INVESTIGATING THE EFFECT DETECTOR GEOMETRY HAS ON HETERODYNE TO NON-HETERODYNE SIGNAL RATIO (HNHR) IN A LOW-COHERENCE TISSUE IMAGING INTERFEROMETER

Department of Physics and Astronomy (CAIS)

University College London

January 2000

A report submitted for the degree of PhD

by

Grant Richard Bedford

Dedication

This thesis is dedicated to the memory of my father

Dick Bedford

who tragically died aged 51, on 19th March 1996,

whilst I was working upon this PhD project.

He is sadly missed.

Acknowledgements

Abstract

A Monte Carlo simulation is used to simulate the emergent light distribution from a turbid media sample placed in the probe beam arm of a scanning low-coherence interferometer that is used to build-up voxelated images in three-dimensions. The sample is a simple three-layered model with an embedded cylinder which simulates the physical and optical properties of skin for near-infrared light passing through the sample. Coherent light from an input probe beam of variable profile and incidence angle is traced through the sample by means of ray-tracing, and any emergent beams are collected in a sample surface array which also logs any emergent Monte Carlo generated photons reaching the surface. At the surface, the heterodyne to non-heterodyne signal ratio (HNHR) measured by a user-defined variable geometry detector is calculated for each point upon a linear scan of the detector position across the sample surface. A coherence gate is set to image a voxel located at the uppermost point of the blood vessel-simulating cylinder. Monte Carlo simulations are performed for various input probe beam angles and probe beam profiles, and the HNHR analysed for various detector geometries by varying: the detector area, central detector axis angle and the acceptance angle at the detector. The Monte Carlo results confirm the benefit of confocal detection, and indicate that angular decoupling of the light delivery and detection systems can improve differential HNHR measurements at scan extremities by 25 to 30 dB provided that stratum corneum is either removed or the sample index matched to the imaging system. Also presented is the description of a prototype experimental low-coherence interferometer system and some of the results derived from it: at its best this system was able to measure reflected coherent signals with a dynamic range approximating 130 dB.

Contents

4

List of figures and tables

Introduction

The past decade has seen an enormous increase in the use of, and research into, optical techniques for use in *in-vivo* medical applications for diagnostic, therapeutic and imaging applications, with a concomitant increase in the use of modelling to analyse and predict the measured results or effects of these various experimental techniques.

Behind these optical techniques, some of which are outlined in sections 1.1 and 1.2, has been much research work into not only modelling techniques, as described below in section 1.3, but measurement of optical parameters of tissue both *in-vivo* and *in-vitro*. (Some measured values for the tissue types and wavelengths of interest to us are given in section 3.4)

In sections 1.1 and 1.2 below, we outline some of the uses to which these optical techniques have been put. Generally these sections present a broad overview of the techniques used in the field and attention is draw to the references therein for further detail. The exception to this broad generality is in section 1.1 where we go into a more detailed discussion of the technique of low-coherence interferometry to illustrate the technique from which the ultimate hypothesis of this thesis and the subsequent results to test that hypothesis were derived.

The sub-divisions 1.1 to 1.3 below are for convenience only, and are not categorical divisions with impermeable boundaries between them: their contents can and do overlap; indeed one ultimate goal for these techniques is the combination of imaging techniques and diagnostic techniques for performing localised *in-vivo* spectroscopy.

1.1 Imaging techniques

In this section we give a brief summary of the main techniques used for forming images using optical and near-infrared radiation. Use of such wavelengths is being actively investigated at present in biological tissues due to the non-ionising properties of this radiation and the spectral properties of tissues at these wavelengths (see section 3.2), even though there are inherent problems in imaging through any

great thickness of such highly scattering-dominated media. Furthermore, optical techniques can be of the "remote sensing" type, in that they do not require an optical probe to be brought into direct contact with the sample being measured. This lessens patient discomfort when measurements are to be performed on painful medical conditions or sensitive organs, such as the eye.

There are three main techniques for imaging in highly scattering tissue samples, all of which are related, and which rely on separating a coherent image from a diffuse scattered light background by either pathlength- or time-resolved means. Polarisation techniques may also be used to further reject scattered light (see section 5.3.4.3.1). The techniques are: time-resolved imaging; holographic imaging and low-coherence imaging. The latter of these, which is of most interest to us, is discussed further in section 1.1.1.

Time resolved imaging[1,2,3,4,5,6,7,8,9,10,11,12] relies upon methods for gating light that is quasi-coherent and thus image-bearing from later arriving light which degrades the detected image. It relies upon the so-called least scattered light to contain information and gates out light which arrives later than this by means of a fast "photographic" method, which may involve the use of a streak camera or Kerr gate for example. Generally short pulses of laser light (femto- to pico-second in duration) are used to probe samples due their high intensity and short temporal coherence, and the samples are investigated using a sample in transmission geometry.

Holographic imaging techniques[13,14,15] involve recording the coherent interference patterns created by light emerging from a sample by exposing an image recording media such as a photographic plate, or more commonly, a CCD camera. This technique can be combined with time gating techniques to give improved rejection of incoherent background light.

1.1.1 Low-coherence imaging techniques

Low-coherence imaging, sometimes known as optical coherence microscopy (OCM), optical coherence tomography (OCT) or coherent detection imaging (CDI), can provide high resolution (of the order 10 μm) non-invasive images in living tissue to a

depth of the order of 1-2 mm depending upon tissue type. It is particularly suited to imaging blood vessels, skin and mucosal linings of the gastrointestinal, respiratory and urogenital tracts which are particularly prone to inflammation, carcinoma and ulceration. Generally the technique is usefully applied in situations where an ability to differentiate soft tissues of closely matched refractive index in highly scattering media is required. Recent studies have even used the technique to perform internal *in-vivo* optical biopsy via a fibre-optic endoscope[16].

Although the OCT technique can be used with confocal imaging techniques, it is physically fundamentally different as it is a way of temporally differentiating photons as opposed to spatially distinguishing them.

Several review papers discuss the basic principles of the low-coherence technique and some of the uses to which it has been put[17,18,19]. The technique usually involves use of an interferometer of the type shown schematically in Figure 1.1 below, although it is not always fibre-optic based[6,20,21,22].

Figure 1.1 shows a low-coherence interferometric system configured as a fibre-optic-based Michelson interferometer. In this system an interference pattern will be seen at the detector only if the reflections from the sample and the reference arms are matched to within the coherence length of the source. In the case of an interferometer designed to image tissue samples, a low-coherence light source operating in the near-infrared region of the optical spectrum is preferred. This permits imaging at micron resolution (the same order of magnitude as the source coherence length) within a region of the optical spectrum at which absorption is at a minimum. Typically, a superluminescent diode (SLD) is used as a source operating at either 850 nm or 1.3 µm, and has a coherence length of around 10-20 µm in tissue. Such systems may be able to deliver several mW of radiant energy to a sample.

The system discriminates scattered photons from those bearing imaging information on a pathlength resolved basis, since only photons whose pathlength matches that of the reference beam to within the coherence length of the source contribute to a heterodyne signal at the detector. So by changing the pathlength in the reference arm the coherent reflectance can be measured as a function of depth in the sample.

Usually, a confocal optical system[22,23,24] is used to deliver the probe beam to the sample and collect light emitted from it in a backscattered direction. Such confocal detection systems help to both focus light into the tissue sample at a point of interest, and also help to reject diffusely scattered light before it reaches the active surface of the photo-detection system.

Since the level of coherent heterodyne signal reaching the detector is generally very small compared to the non-heterodyne light component, coherent detection methods are used to measure it (a shot noise limited HNHR can be obtained with a dynamic range of around 130 to 140 dB using such a technique[19] – where the HNHR, or heterodyne to non-heterodyne signal ratio, is the ratio of the intensity of the light signal reaching the detector that contributes to the heterodyne signal compared to the intensity of all other light signals reaching the same detector). This technique requires spatial modulation of the reference beam (which may be obtained by fibre stretching using a PZT device or by a mirror mounted on a motorised stage, for example) so as to generate a pattern of amplitude varying moving fringes at the detector, the envelope modulation depth of which gives a measure of the coherent reflected signal. Periodic spatial modulation allows the use of a lock-in amplifier to separate the small coherent reflection related periodic signal from the DC diffuse background signal.

Images are generally made up by scanning either the sample beneath the incident optical beam, or by scanning the beam itself, or by a combination of both. Either way, using this technique it is possible to create three-dimensional images of tissue microstructure both *in-vitro*[20,25] and *in-vivo*[16,22,26,27]: in the latter case much work has been undertaken to investigate both intra-occular parameters and to form three-dimensional images of the retina itself[28,29,30,31]. Use of the technique *in-vivo* has led to various works concerned with speeding up the process of the whole image acquisition in an effort to overcome the problems caused by motion artefacts[27,28,31].

An example of a low-coherence interferometric system built by the author is described in Chapter 7.

Figure 1.1: A standard low-coherence interferometer
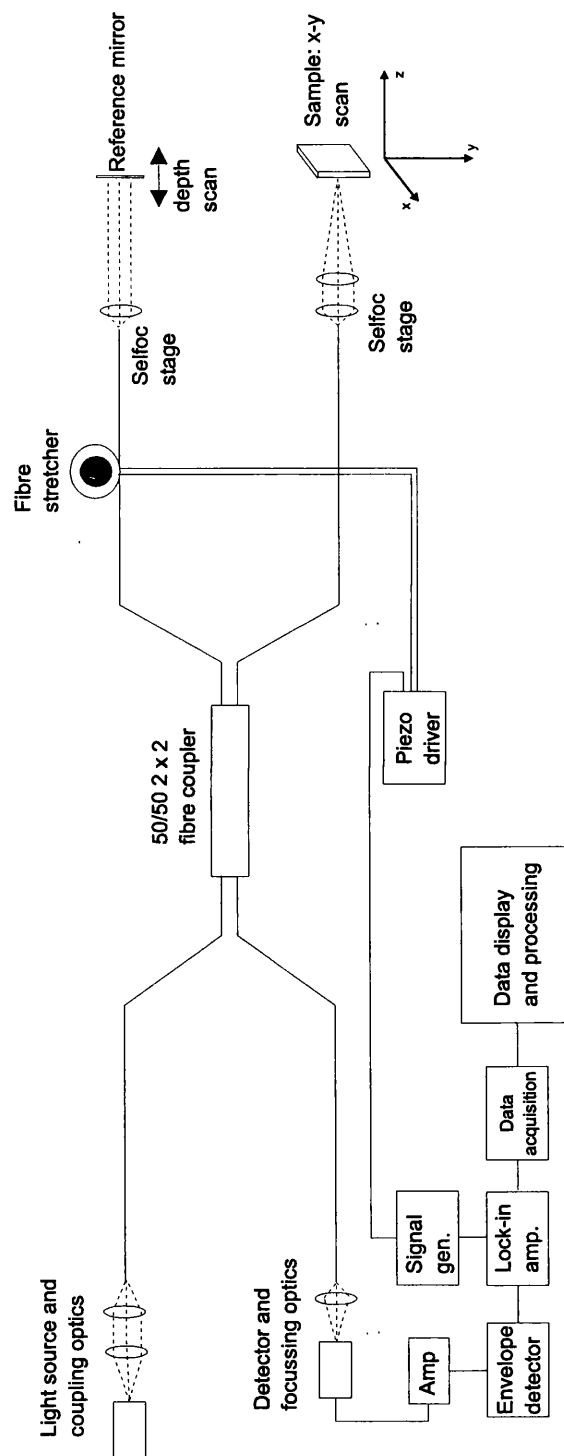
1.2 Therapeutic and diagnostic techniques

Here we mention, for completeness, certain of the other applications besides imaging for which optical and infrared radiation are used but without going into in any great detail and using references that are merely illustrative. These other techniques fall broadly into two categories: therapeutic for the treatment of disease and diagnostic for obtaining clinical information relating to various conditions.

In the first of these two categories are treatments that rely on either: thermal deposition of energy such as photo-coagulation[32] and photo-ablation used in surgery; or treatments relying on photo-chemical effects such as photo-dynamic therapy (PDT), whereby a photo-activated chemical substance is bound to tumours and activated using optical radiation to create free radicals which then attack those tumours.

Diagnostic methods include the use of techniques such as Doppler velocimetry[33,34,35] for measuring *in-vivo* blood flow and spectroscopic techniques[36,37,38,39,40,41] for measuring the concentration of various chromophores.

One "holy grail" in the field of tissue optics is the combination of imaging techniques with spectroscopic techniques so as to produce a system that allows the performance of *in-vivo* localised spectroscopy[36].

1.3 Modelling techniques

In this section we briefly discuss both physical methods and mathematical methods applicable to modelling tissue approximating samples for use in experimental systems and for the prediction of the optical distribution of light, or light induced effects, in tissue, respectively. Numerical modelling of the optical distribution in tissue is also used to enable a fit to experimental data so as to deduce optical properties of measured samples in a process known as the inverse problem[42,43].

Experimentalists have long used intralipid solution[44] in their systems to give a sample having light attenuating properties approximating those of *in-vivo* tissue in that the attenuation is predominantly scattering dominated over the optical and near-

infrared region of the electromagnetic spectrum. Such fluid samples are fine for simulating homogeneous scattering samples held within a glass-walled cuvet, but for imaging it is difficult to produce samples which replicate the structure and shape of an *in-vivo* sample: for example producing a layered sample to simulate skin is difficult using such material. For these reasons solid tissue equivalent phantoms[12,45] have been developed which are easy to machine and to build into complex composite models upon which experimental studies may be performed. A description of the manufacture of such a phantom is described in Chapter 7.

There are numerous analytical or simulation techniques for evaluating the propagation of radiation in tissue[46,47]. The Monte Carlo method[48,49,50,51,52,53] of modelling is a reliable and proven technique which produces accurate results for complex samples, at the expense of being a relatively slow technique requiring plenty of computing power: it was the preferred technique used for the investigations performed to test the hypothesis, outlined below in section 1.4, which forms the basis for the Monte Carlo simulation part of this thesis. It is used not only for simulating imaging systems such as those using OCT[54], but also to simulate energy deposition for thermal and therapeutic effects[55,56,57]. Other noteworthy techniques often used for simulation in the field of tissue optics include finite-element analysis (FEM)[58,59] and other diffusion-theory based models[3,60,61,62].

1.4 Aims of this project

In this section we discuss the train of thought and ideas that led us to propose the hypothesis which the investigation described in the rest of this thesis was designed to test. The experimental system we built went some way towards building a system to test this hypothesis, and the Monte Carlo simulation went one step closer. Unfortunately, the experimental and Monte Carlo results were never fully reconciled, although some interesting results were derived from the Monte Carlo simulated data.

As far as we were aware no studies had investigated the effects of decoupling the optical delivery system in a low-coherence interferometric tissue-imaging system from the light collection system at the time we began our project. Prior systems tended to prefer to use a degenerate delivery and collection system such as that

shown in Figure 1.1, although various studies of how optical elements of low-coherence imaging systems affect the overall system have been made[63,64,65,66,67]. Moreover, certain studies have used decoupled light delivery and collection systems for measuring the optical properties of tissue[43,68,69].

Systems in which the same degenerate optical system is used to both deliver and collect light in a tissue sample necessarily collect relatively large amounts of diffuse background light as the radial diffuse background falls off in intensity as a function of distance from the point at which any incident beam impinges. Furthermore, even for confocal systems, at least a proportion of any specularly reflected probe beam will be incident at the detector and contribute to the non-heterodyne component of the HNHR, if this specular component does not form a desired heterodyne signal component.

Our proposal was therefore to investigate the possible benefits of decoupling the light delivery and light collection paths in a tissue imaging low-coherence interferometric system along the lines shown schematically in Figure 1.2. This meant angling the light delivery and collection systems with respect to the surface of the sample. Some studies have already investigated tilt for measuring tissue optical parameters[68]. It was recognised that going off-axis meant that coherent light had to pass through a greater amount of tissue and therefore would be reduced more in intensity than light incident at an angle normal to the sample surface, but what was less certain was whether the potential benefits of reducing the background intensity outweighed this for the particular sample used.

We envisaged other advantages that may arise from doing this: *viz.* use of a separate light collection arm means that any Fresnel reflections[70] in the light delivery system from lenses, couplers or the 2x2 splitter would not find their way back to the detector as is the case for the degenerate system of Figure 1.1. This can cause particular problems in low-coherence systems whereby multiple coherent Fabry-Perot like reflections may be recorded as coherent signal even if they have not sampled the tissue if, by coincidence, their optical pathlength corresponds to that set by the reference arm of the interferometer. This possible disadvantage is mentioned for note only as it did not form part of our investigations. Another possible benefit is that

20

decoupling of the delivery/detection arms of the interferometer permits the use of dual-balanced detectors which enhance measurement stability[9,37,71] and improve dynamic measurement range by allowing the background DC signal components at each detector to be subtracted from one another. Dual-balanced detection could be introduced into the system of Figure 1.2 by replacing the 1x2 fibre coupler with a 2x2 coupler.

In our investigation we performed Monte Carlo simulations to determine the non-heterodyne signal component emitted from a skin tissue-approximating sample containing an embedded blood vessel for beams incident at various angles with respect to the surface (chapter 4). We then analysed the Monte Carlo generated data and a coherent ray traced signal to enable us to determine a HNHR (chapter 5) as a function of the surface position of a detector for an optical pathlength set so as to image the blood vessel. We thereby simulated an imaging low-coherence interferometer having a light delivery and collection system, similar to that shown in Figure 1.2, scanning the sample at a fixed depth corresponding to an embedded blood vessel.

As a further part of our investigation we built a low-coherence interferometer similar to that shown in Figure 1.1 as a step towards building the interferometer of Figure 1.2, which was to have been used to obtain results to test the data produced by the Monte Carlo simulation. Although the investigations using the low-coherence interferometer were incomplete at the time of writing this thesis, we present details of the experimental system, including system design, circuit characteristics and results from tests on a variety of phantom materials, in Chapter 7. Here we also discuss the problems we encountered in order to provide advice for any persons building a similar system in the future.

Figure 1.2: Low-coherence interferometer with decoupled light delivery and detection system

Retro-reflector

z direction scan

Sample: x-y scan

z

y

x

Selfoc stages

Selfoc stages and focussing

Piezo-electric fibre stretcher

50/50 1 x 2 fibre coupler

50/50 2 x 2 fibre coupler

Piezo driver

Detector and focussing optics

Light source and coupling optics

Beam dump

Pre-amp.

Envelope detector

Lock-in amp.

Data display and processing

Data acquisition
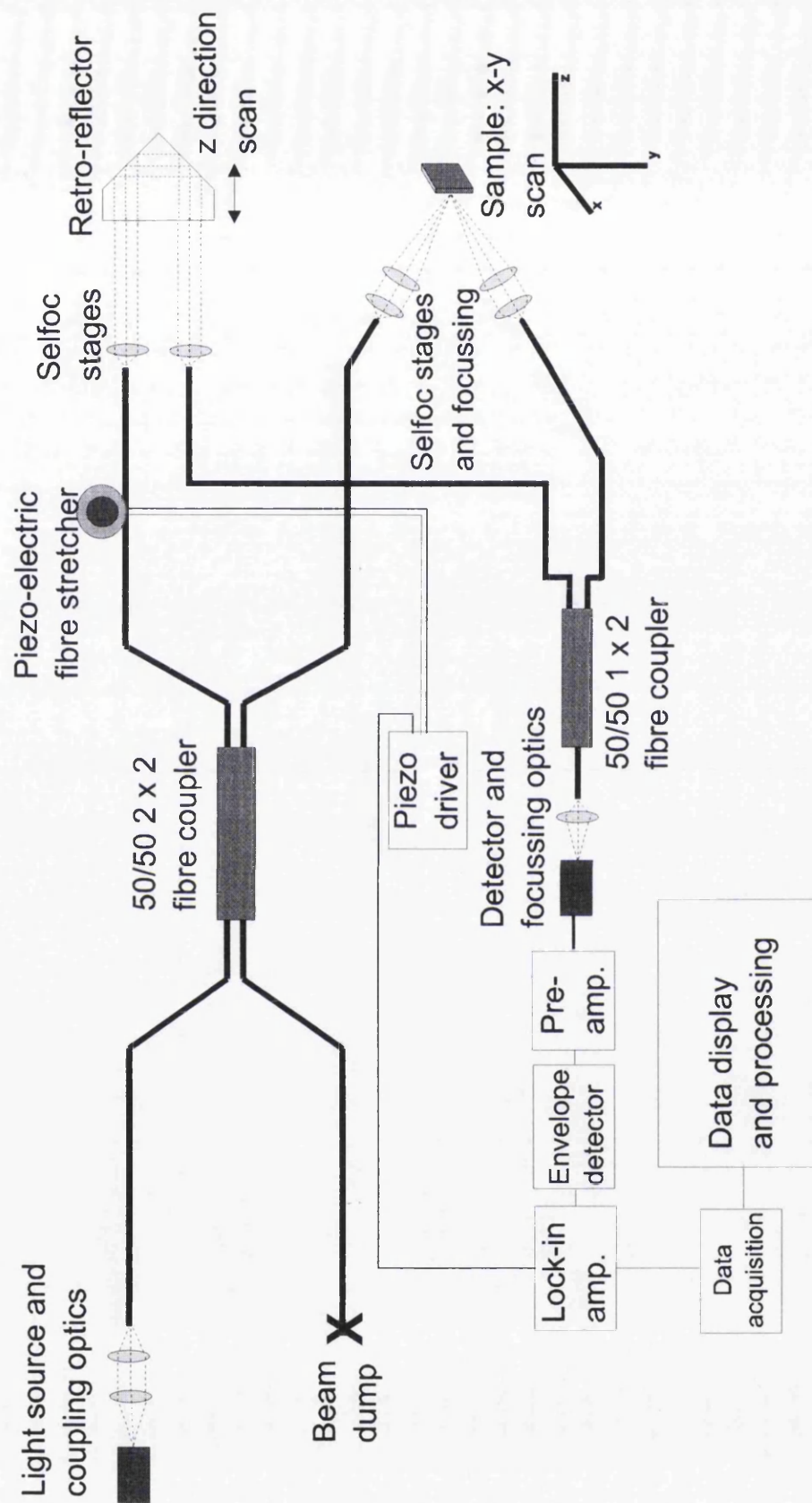
1.5 Structure of the rest of this thesis

The rest of this thesis is dedicated to describing how the hypothesis outlined in section 1.4 above was investigated. We begin in Chapter 2 by giving an outline of the basic terminology and concepts used in tissue optics followed by, in Chapter 3, a general discussion of the physical and optical properties of skin. In Chapter 4 we discuss details of the Monte Carlo simulation and in Chapter 5 describe how the data generated by the Monte Carlo simulation was analysed. In Chapter 6 we show and discuss the results of our Monte Carlo study and draw conclusions from them. For completeness, we present a description of our experimental system, our experimental data, a discussion of the experimental data and details of tissue equivalent phantom materials developed for use with the experimental system in Chapter 7. Chapter 7 also includes a description of the partially complete experimental version of the system shown schematically in Figure 1.2. Chapter 8 presents a brief summary of the content of the thesis. Finally, for completeness, Appendix A provides a listing of the computer control code used to operate the experimental system.

Chapter References

[1] J. Beuthan et al., "Imaging of oblique structures in scattering media by time-gated viewing and coherence imaging (CI)," *SPIE proceedings,* Vol. 1888, pp. 69-75, 1991

[2] M. R. Hee, J. A. Izatt, J. M. Jacobson, E. A. Swanson and J. G. Fujimoto, "Femtosecond transillumination optical coherence tomography," *Opt. Lett.,* Vol. 18, No. 12, pp. 950-952, 1993

[3] J. C. Hebden and D. T. Delpy, "Enhanced time-resolved imaging with a diffusion model of photon transport," *Opt. Lett.,* Vol. 19, No. 5, pp. 311-313, 1994

[4] D. J. Hall, J. C. Hebden and D. T. Delpy, "Imaging very-low-contrast objects in breastlike scattering media with a time-resolved method," *Appl. Opt.,* Vol. 36, No. 28, pp. 7270-7276, 1997

[5] J. G. Fujimoto, S. DeSilvestri, E. P. Ippen, C. A. Puliafito, R. Margolis and A. Oseroff, "Femtosecond optical ranging in biological systems," *Opt. Lett.,* Vol. 11, No. 3, pp. 150-152, 1986

[6] M. R. Hee, J. A. Izatt, E. A. Swanson and J. G. Fujimoto, "Femtosecond transillumination tomography in thick tissues," *Opt. Lett.,* Vol. 18, No. 13, pp. 1107-1109, 1993

[7] B. B. Das, K. M. Yoo and R. R. Alfano, "Ultrafast time-gated imaging in thick tissues: a step toward optical mammography," *Opt. Lett.,* Vol. 18, No. 13, pp. 1092-1094, 1993

[8] K. M. Yoo, Q. Xing and R. R. Alfano, "Imaging objects hidden in highly scattering media using femtosecond second-harmonic-generation cross-correlation time gating," *Opt. Lett.,* Vol. 16, No. 13, pp. 1019-1021, 1991

[9] M. R. Hee, J. A. Izatt, J. M. Jacobson, E. A. Swanson and J. G. Fujimoto, "Femtosecond transillumination optical coherence tomography," *Opt. Lett.,* Vol. 18, No. 12, pp. 950-952, 1993

[10] J. C. Hebden, R. A. Kruger and K. S. Wong, "Time resolved imaging through a highly scattering medium," *Appl. Opt.,* Vol. 30, No. 7, pp. 788-794, 1991

[11] M. D. Duncan, R. Mahon, L. L. Tankersley and J. Reintjes, "Time-gated imaging through scattering media using stimulated Raman amplification," *Opt. Lett.*, Vol. 16, No. 23, pp. 1868-1870, 1991

[12] J. C. Hebden, D. J. Hall, M. Firbank and D. T. Delpy, "Time-resolved optical imaging of a solid tissue-equivalent phantom," *Appl. Opt.*, Vol. 34, No. 34, pp. 8038-8047, 1995

[13] Y. Chen, H. Chen, D. Dilworth, E. Leith, J. Lopez, M. Shih, P. C. Sun and G. Vossler, "Evaluation of holographic methods for imaging through biological tissue," *Appl. Opt.,* Vol. 32, No. 23, pp. 4330-4336, 1993

[14] E. Leith, E. Arons, H. Chen, Y. Chen, D. Dilworth, J. Lopez, M. Shih, P. Sun and J. Vossler, "Use of holography for imaging through inhomogeneous media," *SPIE proceedings Vol. 1942 Underground and obscured object imaging and detection*, pp. 156-165, Orlando, Florida, 1993

[15] E. N. Leith, C. Chen, H. Chen, Y. Chen, J. Lopez and P. C. Sun, "Imaging through scattering media using spatial incoherence techniques," *Opt. Lett.,* Vol. 16, No. 23, pp. 1820-1822, 1991

[16] S. B. Abrams, "Optical coherence tomography moves into the body", *Biophotonics International*, pp. 55-56, Spetember/October 1997 issue

[17] A. F. Fercher, "Optical coherence tomography," *J. Biomedical Optics*, Vol. 1, No. 2, pp. 157-173, 1996

[18] J. A. Izatt, M. D. Kulkami, K. Kobayashi, M. V. Sivak, J. K. Barton and A. J. Welch, A review of optical coherence tomography, *Optics and photonics news*, pp. 41-47, May 1997

[19] K. P. Chan, B. Devaraj, M. Yamada and H. Inaba, " Coherent detection techniques in optical imaging of tissues," *Phys. Med. Biol.*, Vol. 42, pp. 855-867, 1997

[20] J. A. Izatt, M. R. Hee and G. M. Owen, E. A. Swanson and J. G. Fujimoto, "Optical coherence microscopy in scattering media," *Opt. Lett.,* Vol. 19, No. 8, pp. 590-592, 1994

[21] Y. Pan, S. Arlt, R. Birngruber and R. Engelhardt, "Optical coherence tomography in turbid tissue: theoretical analysis and experimental results," *SPIE procs.*, Vol. 2626 BIOS 1995, Barcelona, 1995

[22] J. M. Schmitt, A. Knuttel, A. Gandjbakhche and R. F. Bonner, "Optical characterisation of dense tissues using low-coherence interferometry," *SPIE proceedings*, Vol. 1889., pp. 197-211, 1993

[23] J. M. Schmitt, A. Knuttel and M. Yadlowsky, "Confocal microscopy in turbid media," *J. Opt. Soc. Am. A*, Vol. 11, No. 8, pp. 2226-2235, 1994

[24] C. L. Smithpeter, A. K. Dunn, A. J. Welch and R. Richards-Kortum, "Penetration depth limits of in-vivo confocal reflectance imaging," *Appl. Opt.*, Vol. 37, No. 13, pp. 2749-2754

[25] G. J. Tearney, M. E. Brezinski, M. R. Hee, B. Bouma, J. A. Izatt, E. A. Swanson, J. F. Southern, R. R. Anderson and J. G. Fujimoto, "Optical coherence tomography in multiply scattering tissue," *SPIE proceedings*, Vol. 2389, 1995

[26] B. W. Colston Jr, M. J. Everett, L. B. Da Silva, L. L. Otis, P. Stroeve and H. Nathel, "Imaging of hard- and soft-tissue structure in the oral cavity by optical coherence tomography," *Appl. Opt.*, Vol. 37, No. 16, pp. 3582-3585, 1998

[27] S. M. Reiss, "An imaging modality for the new millennium," *Biophotonics International*, pp. 36-45, October 1999

[28] E. A. Swanson, M. R. Hee, D. Huang, C. P. Lin, C. A. Puliafito and J. G. Fujimoto, "High-speed optical coherence domain reflectometry," *Opt. Lett.,* Vol. 17, No. 2, pp. 151-153, 1992

[29] E. A. Swanson, J. A. Izatt, M. R. Hee, D. Huang, C. P. Lin, J. S. Schuman, C. A. Puliafito and J. G. Fujimoto, "In vivo retinal imaging by optical coherence tomography," *Opt. Lett.,* Vol. 18, No. 21, pp. 1864-1866, 1993

[30] A. F. Fercher, K. Mengedoht and W. Werner, "Eye-length measurement by interferometry with partially coherent light," *Opt. Lett.*, Vol. 13, No. 3, pp. 186-188, 1988

[31] J. Szydlo, H. Bleuler, R. Wälti and R. P. Salathè, "High-speed measurements in optical low-coherence reflectometry," *Meas. Sci. Technol.*, Vol. 9, pp. 1159-1162, 1998

[32] A. L. McKenzie, "Physics of thermal processes in laser-tissue interaction," *Phys. Med. Biol.*, Vol. 35, No. 9, pp. 1175-1209, 1990

[33] A. F. Fercher, H. C. Li and C. K. Hitzenberger, "Slit lamp laser Doppler interferometer," *Lasers in Surgery and Medicine*, No. 13, pp. 447-452, 1993

[34] G. Dougherty, "A laser Doppler flowmeter using variable coherence to effect depth discrimination," *Rev. Sci. Inst.*, Vol. 63, No. 5, pp. 3220-3221, 1992

[35] X-J. Wang, T. E. Milner, Z. Chen and J. S. Nelson, "Measurement of fluid-flow-velocity profile in turbid media by the use of optical Doppler tomography," *Appl. Opt.*, Vol. 36, No. 1, pp. 144-149, 1997

[36] D. A. Benaron, B. Rubinsky, M. Shannon and D. C. Ho, "Imaging (NIRI) and quantitation (NIRS) in tissue using time-resolved spectrophotometry: The impact of statistically and dynamically variable optical path lengths," *SPIE proceedings*, Vol. 1888, pp. 10-21, 1991

[37] A. Duncan, T. L. Whitlock, M. Cope and D. T. Delpy, "A multiwavelegth, wideband, intensity modulated optical spectrometer for near infrared spectroscopy and imaging," *SPIE proceedings*, Vol. 1888, pp. 248-254, 1991

[38] D. T. Delpy, "Optical spectroscopy for diagnosis," *Physics World*, Vol. 7, No. 8, pp. 34-39, 1994

[39] V. V. Tuchin, S. R. Utz and I. V. Yaroslavsky, "Tissue optics, light distribution, and spectroscopy," *Opt. Eng.*, Vol. 33, No. 10, pp. 3178-3188, 1994

[40] M. Keijzer, R. R. Richards-Kortum, S. L. Jaques and M. S. Feld, "Fluorescence spectroscopy of turbid media: Autofluorescence of the human aorta," *Appl. Opt.*, Vol. 28, No. 20, pp. 4286-4292, 1989

[41] U. S. Sathyam, B. W. Colston Jr., L. B. Da Silva and M. J. Everett, "Evaluation of optical coherence quantitation of analytes in turbid media by use of two wavelengths," Appl. Opt., Vol. 38, No. 10, pp. 2097-2104, 1999

[42] R. L. Barbour, H. L. Graber, R. Aronson and J. Lubowsky, "Imaging of subsurface regions of random media by remote sensing," *SPIE proceedings*, Vol. 1431, p. 192, 1991

[43] M. H. Eddowes, T. N. Mills and D. T. Delpy, "Monte Carlo simulations of coherent backscatter for identification of the optical coefficients of biological tissue *in vivo*," *Appl. Opt.*, Vol. 34, No. 13, pp. 2261-2267, 1995

[44] S. T. Flock, S. L. Jacques, B. C. Wilson, W. M. Star and M. J. C. van Gemert, "Optical properties of intralipid: a phantom medium for light propagation studies," *Lasers. Surg. Med.*, Vol. 12, pp. 510-519, 1992

[45] M. Firbank, M. Hiraoka and D. T. Delpy, "Development of a stable and reproducible tissue equivalent phantom for use in infrared spectroscopy and imaging," *SPIE proceedings*, Vol. 1888, pp. 264-270, 1991

[46] W. M. Star, J. P. A. Marijnissen and M. J. C. van Gemert, "Light dosimetry in optical phantoms and in tissues: I. Multiple flux and transport theory," *Phys. Med. Biol.*, Vol. 33, No. 4, pp. 437-454, 1988

[47] M. S. Patterson, B. C. Wilson and D. R. Wyman, "The propagation of optical radiation in tissue," (Parts I and II), *Lasers in med. sci.*, Vol. 6, No. 2, pp 155-168 and Vol. 6, No. 4, pp 379-390, 1991

[48] M. Hiraoka, M. Firbank, M. Essenpreis, M. Cope, S. R. Arridge, P. van der Zee and D. T. Delpy, "Monte Carlo simulation of light transport through inhomogeneous tissue," *SPIE proceedings*, Vol. 1888, pp. 149-159, 1991

[49] S. Feng and F. Zeng, "Monte Carlo simulations of photon migration path distributions in multiple scattering media," *SPIE proceedings*, Vol. 1888, pp. 78-89, 1991

[50] G. Zaccanti, "Monte Carlo study of light propagation in optically thick media: point source case," *Appl. Opt.*, Vol. 30, No. 15, pp. 2031-2041, 1991

[51] Y. Pan, R. Birngruber, J. Rosperich and R. Engelhardt, "Low-coherence optical tomography in turbid tissue-1: Theoretical analysis", *Appl. Opt*, Vol. 34, pp. 6564-6574, 1995

[52] M. Firbank, S. R. Arridge and D. T. Delpy, "An investigation of light transport through scattering bodies with non-scattering regions," *Photons in Medicine and Biology*, Pre-print, 1996

[53] J. K. Barton, T. E. Milner, T. J. Pfefer, J. S. Nelson and A. J. Welch, "Optical low-coherence reflectometry to enhance Monte Carlo modeling of skin," *J. Biomed. Opt.*, Vol. 2, No. 2, pp. 226-234, 1997

[54] G. Yao and L. V. Wang, "Monte Carlo simulation of an optical coherence tomography signal in homogeneous turbid media," *Phys. Med. Biol.*, Vol. 44, pp. 2307-2320, 1999

[55] L. V. Wang, R. E. Nordquist and W. R. Chen, "Optical beam size for light delivery to absorption-enhanced tumors buried in biological tissues and effect of muliple-beam delivery: a Monte Carlo study," *Appl. Opt.*, Vol. 36, No. 31, pp. 8286, 1997

[56] Z. Song, K. Dong, X. H. Hu and J. Q. Lu, "Monte Carlo simulation of converging laser beams propagating in biological materials," *Appl. Opt.*, Vol. 38, No. 13, pp. 2944-2949, 1999

[57] L. V. Wang and G. Liang, "Absorption distribution of an optical beam focussed into a turbid medium," *Appl. Opt.*, Vol. 38, No. 22, pp. 4951-4958, 1999

[58] M. Schweiger et al., "Comparison of finite element forward model with experimental phantom results: application to image reconstruction," *SPIE proceedings*, Vol. 1888, pp. 179-190, 1991

[59] S. R. Arridge and M. Schweiger, "Photon-measurement density functions. Part 2: Finite-element-method calculations," *Appl. Opt.*, Vol. 34, No. 34, pp. 8026-8037, 1995

[60] S. Wan, R. R. Anderson and J. A. Parrish, "Analytical modelling of the optical properties of the skin with *in-vitro* and *in-vivo* applications," *Photochem. and Photobiol.*, Vol. 34, pp. 493-499, 1981

[61] J. M. Schmitt, G. X. Zhou, E.C. Walker and R. T. Wall, "Multilayer model of photon diffusion in skin," *J. Opt. Soc. Am. A.*, Vol. 7, No. 11, pp. 2141-2153, 1990

[62] I. Dayan, S. Havlin and G. H. Weiss, "Photon migration in a two-layer turbid medium: A diffusion analysis," *J. Mod. Opt.*, Vol. 39, No. 7, pp. 1567-1582, 1992

[63] X. Clivaz, F. Marquis-Weible, R. P. Salathé, R. P. Novàk and H. H. Gilgen, "High resolution reflectometry in biological tissues," *Optics Letters*, Vol. 17, No. 1, Jan. 1992

[64] J. A. Izatt, M. R. Hee and G. M. Owen, E. A. Swanson and J. G. Fujimoto, "Optical coherence microscopy in scattering media," *Opt. Lett.*, Vol. 19, No. 8, pp. 590-592, 1994

[65] J. M. Schmitt, A. Knuttel, M. Yadlowsky and M. A. Eckhaus, "Optical-coherence tomography of a dense tissue: statistics of attenuation and backscattering," *Phys. Med. Biol.*, Vol. 39, pp. 1705-1720, 1994

[66] J. M. Schmitt, A. Knuttel and M. Yadlowsky, "Confocal microscopy in turbid media," *J. Opt. Soc. Am. A*, Vol. 11, No. 8, pp. 2226-2235, 1994

[67] D. J. Smithies, T. Lindmo, Z. Chen, J. S. Nelson and T. E. Milner, "Signal attenuation and localization in optical coherence tomography studied by Monte Carlo simulation," *Phys. Med. Biol.*, Vol. 43, pp. 3025-3044, 1998

[68] S. L. Jacques, C. A. Alter and S. A. Prahl, "Angular dependence of HeNe laser light scattering by human dermis," *Lasers in the life sciences*, Vol. 1, No. 4, pp. 309-333, 1987

[69] L. Wang and S. L. Jacques, "Use of a laser beam with an oblique angle of incidence to measure the reduced scattering coefficient of a turbid medium," *Appl. Opt.*, Vol. 34, No. 13, pp. 2362-2366, 1995

[70] K. Takada A. Himeno and K. Yukimatsu, "Phase-noise and shot-noise limited operations of low coherence optical time domain reflectometery," *Appl. Phys. Lett.*, Vol. 59, No. 20, pp. 2483-2485, 1991

[71] M. R. Hee, J. A. Izatt, J. M. Jacobson, E. A. Swanson and J. G. Fujimoto, "Time-gated imaging with femtosecond transillumination optical coherence tomography," *SPIE proceedings*, Vol. 1888, pp. 28-36, 1993

Interaction of optical radiation with turbid media

2.1 Chapter overview

In this chapter we discuss the interaction of radiation with turbid media. We present a general overview of some of the concepts and terminology used in this field which besides being a useful background also allows us to define some of the terminology and equations that were used in the calculations and algorithms of the later chapters. Many excellent works discuss this subject matter in much greater detail than we are able to give here and we refer readers to these other references for more detail[1,2,3,4,5].

2.2 The optical properties of turbid media: methods of interaction

The effect of scattering and absorption by particles upon an incident parallel beam of light is to reduce the intensity of light that is detected by a collimated detector facing into the incident light beam. Any absorbed light deposits its energy as heat, causing molecules to vibrate, rotate or translate, whereas light which is scattered is merely redistributed in space. Other, non-linear, processes such as fluorescence, and inelastic scattering may also occur, but are not considered to be of consequence at the wavelengths and power levels that we were concerned with in this project.

Attenuation of a beam of light is usually spoken of in terms of either absorption or scattering, and mathematically these two processes can be treated in a very similar way. Often the intensity attenuation follows an exponential decay relationship which is described as "Beer Law" like. A similar relationship holds for the light that is attenuated by scattering, under the circumstances that are described further on in this chapter where we consider absorption and scattering as separate entities.

Some possible end permutations for a photon entering a turbid media are shown below in figure 2.1: other cases not shown include the case of a multiply scattered photon not hitting the detector; a multiply scattered photon which is backscattered and a multiply scattered photon which is absorbed.

Figure 2.1: Simple schematic illustrating the mechanisms by which light is attenuated in a turbid media
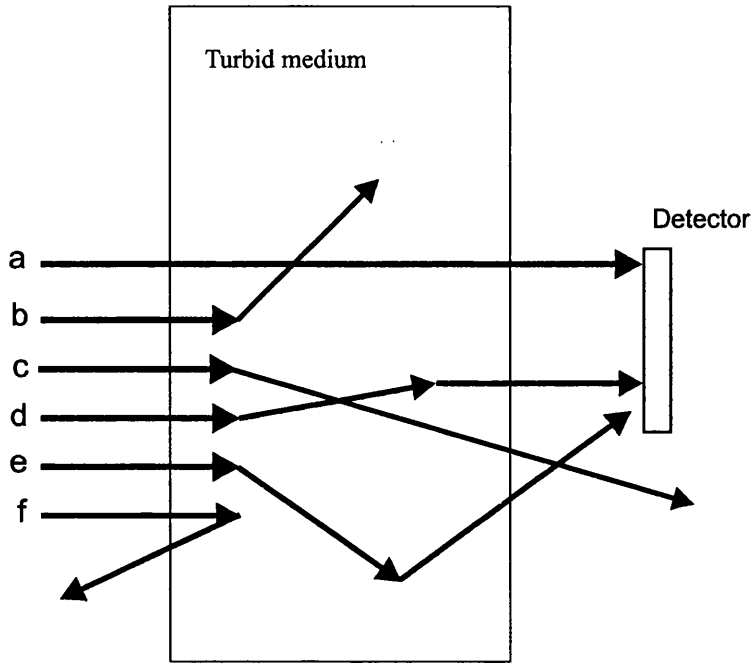
a) unattenuated component; b) photon singly scattered and then absorbed; c) singly scattered and not detected; d) multiply scattered emerging parallel to the axis and detected; e) multiply scattered emerging at an angle to the axis and detected; f) backscattered component

2.2.1 Absorption

We have already mentioned that absorption can be described using an exponentially decaying intensity profile. This description is simple and has been used for many years to predict how light is attenuated upon passage through an optically absorbing media. In its differential form, the Lambert-Bouguer law, it simply states that equal thicknesses of material dx absorb the same fraction dI/I of the light intensity I incident upon them, so that $dI/I = \mu_a dx$ where μ_a is a constant of proportionality known as the absorption coefficient and whose dimensions are inverse length. In its best known form it is valid only for a homogeneous media, or those that can be treated as such overall, and follows the relationship:

$$I = I_0 e^{-\mu_a x} \qquad\qquad (2.1)$$

where I_0 is the intensity of the incident light and x the depth of penetration into the sample. We may express the same equation using Napierian (base ten) logarithms, as follows:

$$A = \log_{10}\left(\frac{I_0}{I}\right) = \kappa x \qquad (2.2)$$

and from this define the extinction coefficient κ (a constant with dimensions of inverse length) and the optical density (OD) A (a dimensionless quantity which is a measure of material absorbency). Again this is in differential form and for a homogeneous medium we may express equation 2.2 as an exponential by raising both sides to the power ten giving:

$$I = I_0 .10^{-\kappa x} \qquad (2.3)$$

For completeness, we include another useful and widely used expression, the Beer-Lambert law. This finds great usage in the field of absorption spectroscopy because it is able to deal with concentrations of chromophores in solution. It applies to an absorbing medium that is dissolved in a solvent whose absorption is negligible compared to that of the solute. This relationship, derived by Beer in the middle of the nineteenth century, simply states that the optical density of a solution is proportional to the concentration of absorber in that solution. Mathematically it follows the following differential relationship:

$$A = \log_{10}\left(\frac{I_0}{I}\right) = \alpha c x \qquad (2.4)$$

where α is the extinction coefficient for unit absorber concentration (units of inverse length and inverse concentration) known as either absorptivity, the specific extinction coefficient or absorbency index, and c the concentration of the solution.

2.2.2 Scattering of light

In this section we continue to define some of the commonly used terminology and ideas that are associated with scattering media, (through sections 2.2.2.1 to 2.2.2.3). In order to understand light scattering in tissue it is first necessary to discuss single

particle scattering theory, even though this does not really occur in tissue, because this provides insight into the mechanisms and mathematical descriptions that underlie the more complex problem of tissue scattering. However, it must be borne in mind that the direct applicability of this theory is only to situations in which either a single particle is under consideration, or where the number density of particles is low enough to ensure that the probability of a photon being scattered more than once is negligible. We consider a number of different models and descriptions in this sub-chapter (sections 2.2.2.4 to 2.2.2.6), all of which have been used to describe the radiation patterns that are produced when a plane electromagnetic wave interacts with a single scattering particle. Thereafter in section 2.2.2.7 we introduce multiple scattering.

For any optically attenuating medium it is possible to define the linear attenuation coefficient, μ, thus:

$$\mu = \mu_a + \mu_s \tag{2.5}$$

where we have now introduced the scattering coefficient μ_s. The scattering coefficient is a measure of the amount by which a collimated beam is attenuated by the scattering of radiation away from the initial direction of propagation. It behaves similarly to the absorption coefficient in equation 2.1. The linear attenuation coefficient is thus a parameter which combines the effects of both the scattering and absorption effects present in the material. By using the linear attenuation coefficient we can express the material effect upon an optical beam as:

$$I = I_0 e^{-\mu x} \tag{2.6}$$

where, as before, I is the transmitted intensity measured by the detector, I_0 is the intensity of the incident light and x the depth of penetration into the sample. The total linear attenuation coefficient is related to the mean free path, d, of a photon in that material by the relationship:

$$d = 1 / \mu \tag{2.7}$$

which is the mean distance that a photon will travel in an attenuating medium before it interacts with that medium either through scattering or absorption.

2.2.2.1 Extinction cross section

Another term that is sometimes used for quantifying the effect of a single scattering particle upon an incident light beam is the extinction cross section. Extinction cross section is defined as being the equivalent area of a perfectly absorbing flat disk that would have to be inserted into a collimated beam in order that a detector of infinitely narrow solid acceptance angle would detect the same amount of light as that passing through the scatterer. The analogy is similar to that used in nuclear physics to define capture cross sections for various species by radionucleides.

In common with the linear attenuation coefficient, the extinction cross section, σ_e, is formed as the sum of the absorption and scattering cross sections, (σ_a and σ_s respectively):

$$\sigma_e = \sigma_a + \sigma_s \tag{2.8}$$

Another set of useful expressions may be derived from the concept of the extinction cross section. Extinction efficiency, Q_e, is the ratio of the extinction cross section to the cross sectional area of the particle projected onto the detector. If the particle were a non-scattering pure absorbing disk, Q_e would be unity. In reality it can be either greater or larger than one, depending upon the degree of interference between the scattered and unscattered waves. Specific cross sections, relating to mass or volume are also terms used, especially in tissue optics. These are the mass extinction coefficient α_m and the volume extinction coefficient α_v defined per unit mass or unit volume respectively.

2.2.2.2 Albedo

The albedo, a, is a parameter which gives a measure of the relative contribution of scattering to the total optical attenuation in a scattering medium, and is therefore a parameter frequently used in the literature to describe situations in which both scattering and absorption are present. It is defined as follows:

$$a = \frac{\mu_s}{\mu_a + \mu_s} = \frac{\mu_s}{\mu}$$

(2.9)

The albedo is a dimensionless quantity, whose value varies from zero when there is pure absorption, to unity when scattering makes up the only contribution to attenuation of the optical signals. In skin tissue, the albedo tends to unity for near-infrared illumination, as scattering is the dominant component of the total optical attenuation (see chapter 3 for measured values).

2.2.2.3 Anisotropic g-factor

Usually for scattering particles, and particularly for irregularly shaped ones such as cells, a complex angular scattering pattern is produced at angles away from the direction of the incident beam. The intensity of the scattered wave generally depends on the direction r' of the incident wave and the direction r of the scattered wave. Resulting complex patterns arise from interference between scattered secondary wavelets from different parts of the particle, and the unscattered incident beam. Figure 2.2 shows an example of such a pattern.

Figure 2.2: Typical angular intensity diagram for a large non-absorbing particle
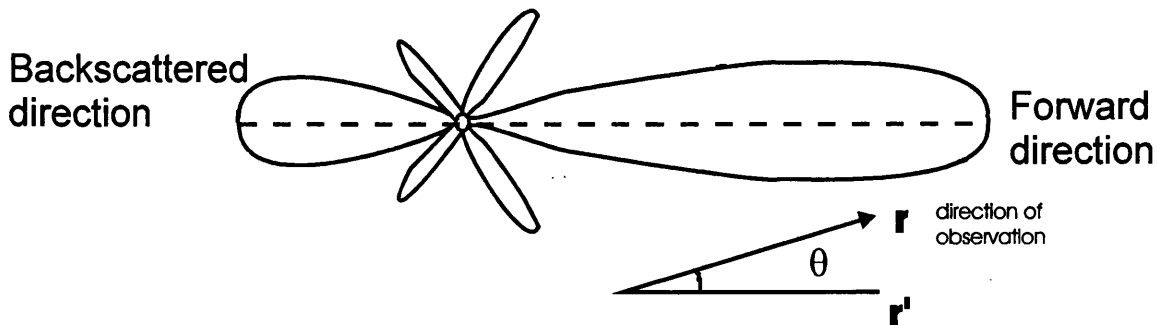
The above figure represents a polar plot for the angular distribution of intensity around a purely scattering particle. The distance from the particle to the outline in the direction of the arrow is proportional to the intensity of the scattered light in the direction θ.

The resulting angular distribution pattern is known as the differential scattering coefficient. However, it is more usual to use a normalised version of this differential scattering coefficient, called the scattering phase function $p(\theta)$, a parameter encountered in many texts within the field of scattering optics, and which, for photons, may be interpreted as being the probability of an incident photon being scattered from direction $\mathbf{r'}$ into the direction $\mathbf{r}$ by the scattering particle. The normalisation condition is that:

$$\int_0^{2\pi} p(\theta)\sin(\theta)d\theta = 1 \qquad (2.10)$$

If scattering is considered to be symmetric about the direction of the incident beam, the phase function depends only upon the scattering angle, θ, between the forward (unscattered) direction and the direction of the scattered beam. In this case the scattering characteristic is often described by the mean cosine of the scattering angle g (the anisotropy or g-factor), thus:

$$g = \int_{4\pi} p\cos\theta \, d\Omega \qquad (2.11)$$

where integration is performed over 4π radians of solid angle Ω.

For $g = 0$, the scattered radiation is isotropically distributed over all angles, $g > 0$ indicates scattering predominantly into the forward direction ($\theta < 90°$), whilst $g < 0$ indicates that backscattering is dominant ($\theta > 90°$). In the case where $g = 1$ all light is scattered in the forward direction ($\theta = 0°$). It is worth emphasising at this point that, because light moving through biological tissue is generally scattered in the forward direction, typical anisotropy factors for g tend to lie between 0.7 and 0.97 for different tissue types - see chapter 3.

2.2.2.3.1 Reduced scattering coefficient

Having defined the scattering coefficient μ_s we now define the reduced scattering coefficient μ_s' as follows:

$$\mu_s' = \mu_s(1-g) \qquad (2.12)$$

and a corresponding reduced attenuation coefficient:

$$\mu' = \mu_a + \mu_s(1-g) \tag{2.13}$$

This allows the effects of the directionality of the scattering to be accounted for by producing a scattering coefficient for the medium that would give rise to the same attenuation if diffuse illumination and isotropic scattering is assumed. It may also be used to define how rapidly the intensity of a diffuse light beam (one that has undergone many scattering events) falls off with distance into the sample, by substituting μ_s' for μ_s in all previous equations.

As an example, μ_s, which defines how coherent light will be attenuated upon propagation through the sample, may have a value of 20 mm^{-1} in a tissue sample with a corresponding g-factor of 0.9 (typical for certain tissues). This then leads to a reduced scattering coefficient of $\mu_s' = 2$ mm^{-1}. Hence the coherent light signal intensity in tissue falls by a factor of 10^5-10^6 by the time it has penetrated to the region where diffuse light is deemed to be dominant. This depth is at approximately $1/\mu_s'$ below the tissue surface, or 0.5 mm in the case of the example given. So the received detector intensity passing through more than a few scattering lengths of a medium is dominated by the diffuse light component. It is this rapid loss of the coherent signal that restricts the thickness of a material through which images may be formed to around 25 scattering mean free paths (beyond this thickness, for any reasonable input light intensity, the coherent signal is dominated by quantum noise effects).

2.2.2.4 Rayleigh scattering

Rayleigh scattering is applicable to the case where scattering particles, such as molecules, are small compared to the wavelength of the light that is incident upon them. A theoretical analysis may be derived from dimensional analysis, or Mie theory (section 2.2.2.6) under restriction of the Mie expansion to only a few terms (an accurate assumption for small particles), or alternatively by considering the radiation scattered by oscillating electric dipoles that are induced by the incident radiation. All of these methods predict the same wavelength dependence for the

intensity of the scattered light; namely that the scattered intensity is proportional to the inverse of the fourth power of wavelength.

In the Rayleigh regime the scattered intensity I_s is proportional to the incident intensity, the volume, observation distance, and the wavelength according to the following relationship:

$$I_s \alpha \, I_i \frac{V^2}{z^2 \lambda^4}$$

(2.14)

where V is the particle volume, z the distance of the particle from the observation point, λ the wavelength, I_i the incident irradiance.

Mie theory predicts that for unpolarised light:

$$\frac{I_s}{I_i} = \frac{8\pi N' r^6}{\lambda^4 z^2} \left[\frac{m^2 - 1}{m^2 + 2} \right]^2 (1 + \cos^2 \theta)$$

(2.15)

for the Rayleigh scattering regime; where the factor $1 + \cos^2 \theta$ describes the polarisation effects of contributions from incident light polarised perpendicular and parallel to the scattering plane, r is the particle radius, and $N' = n' + ik'$ is the complex refractive index of the particle and m is the relative refractive index defined as the ratio of the complex refractive indices inside and outside the particle (which has a weak wavelength dependence). The angular distribution of unpolarised scattered light is nearly isotropic, and this is typical of Rayleigh scattering. Mie theory also demonstrates the characteristic Rayleigh wavelength dependence.

2.2.2.5 Rayleigh-Gans-Debye theory

For tenuous large scatterers, that is those whose refractive index is comparable to that of the medium in which they are suspended and whose absorbance is low, Rayleigh-Gans-Debye (RGD) theory is a useful tool for predicting the scattering properties. Using RGD theory, it is possible to calculate the scattering function for arbitrarily shaped particles which cannot be found by other means. As with all of the other modelling techniques we have mentioned in the small particle limit ($\lambda \gg 2r$)

RGD theory reassuringly approximates to Rayleigh scattering. To apply RGD theory it is necessary to satisfy the following two inequalities[5]:

$$|m-1| \ll 1 \qquad (2.16)$$

$$\frac{\pi}{\lambda} r |m-1| \ll 1$$

where $2r$ is the largest diameter of the particle. These express the requirement that the relative refractive index of the particle must be near unity and that the phase change across the particle must be very similar to that which would occur in the same distance of the surrounding medium (the definition of a large tenuous scatterer). In practice this means there is no appreciable reflection at the particle/medium boundary and a field pattern inside the particle that is nearly identical to the outside medium.

Figure 2.3: Geometry for RGD scattering
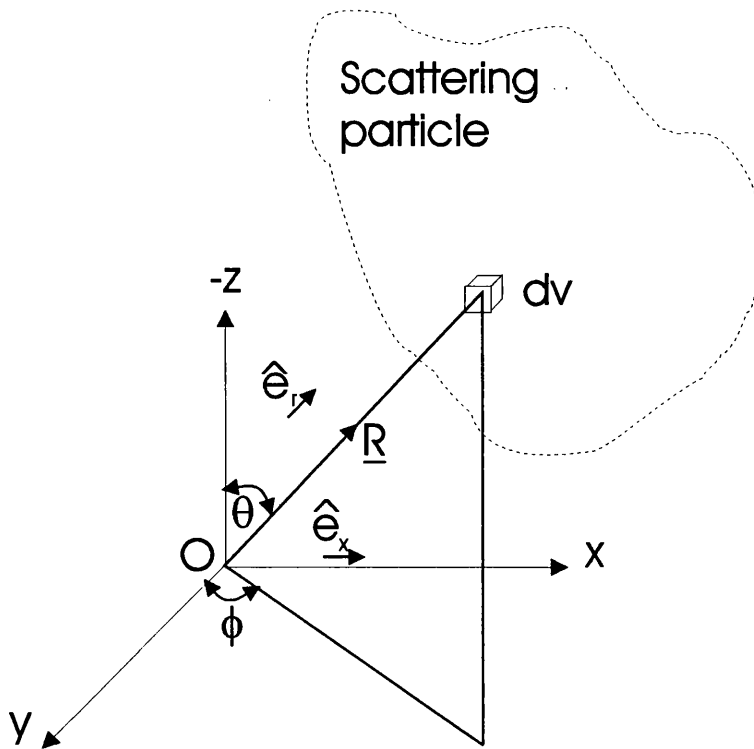
When the above inequalities 2.16 are satisfied, the solution is a modified version of the Rayleigh scattering function[6]:

$$\frac{I_s}{I_i} = \frac{4\pi^2 V^2}{\lambda^4 z^2}[m-1]^2 f^2(\theta,\phi)(1+\cos^2\theta) \qquad (2.17)$$

Here f(θ,ϕ) is the form factor and:

$$f(\theta,\phi) = \frac{1}{V}\int_V e^{i\delta}dv \qquad (2.18)$$

Where δ, the phase difference that results between the scattered and unscattered radiation that passes through the volume dv, is integrated over the particle volume and is given by $\delta = k\mathbf{R}.(\hat{e}_x - \hat{e}_r)$. $\mathbf{R}$ is a vector from an arbitrary origin to the volume dv, $\hat{e}_x$ is a unit vector in the direction of the incident light, $\hat{e}_r$ is a unit vector in the direction (θ,ϕ). This geometry is illustrated above in Figure 2.3.

Equation 2.17 above is similar to the result of Rayleigh, with a modifying angular function dependent upon the shape of the particle. Calculation of the form factor may be performed by numerical integration in the case of complex functions, or analytically for simple geometries. In the case of the homogeneous sphere of radius r and refractive index N', the form factor becomes:

$$f(\theta) = \frac{3}{u^3}(\sin u - u\cos u) \qquad (2.19)$$

where:

$$u = \left(\frac{4\pi N'r}{\lambda}\right)\sin\left(\frac{\theta}{2}\right) \qquad (2.20)$$

It is seen that large scatterers tend to give rise to peaked angular distributions (similar to those shown in Figures 2.2 and 2.4) due to regions of both constructive and destructive interference about the circumference of the particle. The larger the particle the greater the number of possible light paths. Conversely the scattering due to small particles becomes more uniform as the size is decreased and ultimately the

37

Rayleigh criteria is reached when the scattering becomes perfectly uniformly distributed.

Figure 2.4 below represents a hypothetical particle angular scattering pattern for an incident beam propagating from left to right. As the particle has an absorbing component, in contrast to that shown in Figure 2.2, there is an incomplete cancellation in intensity in this interference pattern due to the variations in intensity between the incident and scattered light beams, and the angular distribution of intensity never reaches zero.

Figure 2.4: Rayleigh-Ganz-Debye model of a large tenuous scatterer with absorption present
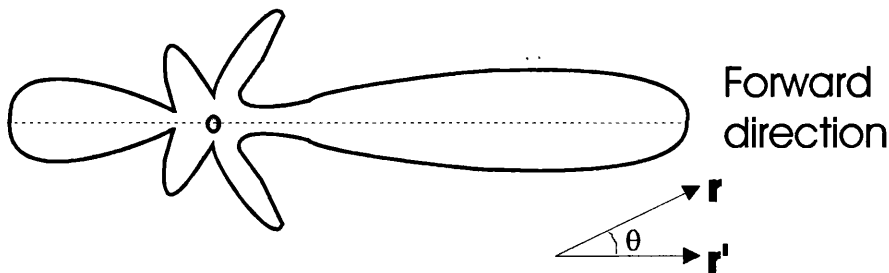
2.2.2.6 Mie theory[3]

Mie scattering theory gives exact analytical solutions to the problem of scattering and absorption of light by spherical particles as it is based upon exact solutions of Maxwell's equations. It has also been extended to include prolate spheroids[2,3], although its main implementation is still for the less complex problem of the sphere. The method works by solving Maxwell's equations in and around the particle providing an exact map of the internal and external electro-magnetic fields.

Useful insight is gained into the scattering from cells using Mie theory. Although cells are not perfectly spherical, the technique is able to provide some indication to the kind of field patterns that may surround cells by modelling them as spheres of approximately the same equivalent volume.

It is also common for experiments to be carried out using polystyrene microspheres in solution because Mie theory can be used for calculating the scattering coefficient

and *g*-factor precisely. Mie theory is also used to calculate the scattering coefficient of the solid phantom materials used as samples in our experimetal system: see Chapter 7 for more details.

2.2.2.7 Multiple scattering

Multiple scattering gives rise to long path lengths in the sample which subsequently increases the likelihood of the photon being absorbed, and certain researchers have used this property to improve their imaging techniques by adding absorbing material to attenuate the multiply scattered light.

It is the *g*-factor which describes the directionality of the scattered light, and this is used in the description of multiple scattering. The reduced scattering coefficient may be defined for the diffuse light and by similarly defining reduced values for $Q(1-g)$, σ $(1-g)$ and α_v $(1-g)$ we can account for the effects of multiple scattering on a beam of light. Cope[5] illustrates the effect of multiple scattering by calculating the most volume efficient scattering coefficient, α_v, for both a single particle and multiple scattering of particles of relative refractive index 1.042 at 800 nm. The results indicate that for a single particle this value for the radius is 3.275 microns, whereas for multiple scattering it drops to 0.166 microns.

Measurement of these multiple scattering coefficients and the spatial distributions of multiply scattered photons are notoriously difficult, especially for highly forward scattering light and for retroreflected light. Unfortunately because the light in tissue tends to be highly forward scattered measurements upon such samples are rare in the literature, especially for *in vivo* studies. We present some of the data that has been published for measurements in human tissue in the following chapter.

Chapter References

[1] A. Ishimaru, Wave Propagation and Scattering in Random Media Vols. 1 and 2 (Academic Press, New York, 1978)

[2] H. C. van de Hulst, Light scattering by small particles, (Dover publications, New York, 1981)

[3] C. F. Bohren and D. R. Huffman, Absorption and scattering of light by small particles, (Wiley-Interscience, New York, 1983)

[4] M. S. Patterson, B. C. Wilson and D. R. Wyman, "The propagation of optical radiation in tissue," (Parts I and II), Lasers in Med. Sci., Vol. 6, No. 2, pp 155-168 and Vol. 6, No. 4, pp 379-390, 1991

[5] M. Cope, The development of a near infrared spectroscopy system and its application for non invasive monitoring of cerebral blood and tissue oxygenation in the newborn infant, (PhD thesis, University College London, 1991)

[6] S. P. Parker, The optics source book, (McGraw-Hill, New York, 1986)

The Physical and Optical Properties of Skin

In this chapter we discuss both the physical structure and the optical properties of skin. The physical properties define the optical properties of the components in a skin sample, and this chapter concludes with a summary of known measured and calculated optical properties for such components.

3.1 The physical properties of skin

Before one can really talk meaningfully about the optical properties of skin it is necessary to go into some anatomic details in order to get a feeling for the structures that are present, as illustrated in Figure 3.1. These structures define how the skin responds to light and define the distribution of both the absorption and scattering parameters, μ_a and μ_s. As an optical medium skin is complex in that it consists not only of relatively large anatomical components and structure on a cellular level between approximately 1 and 20 μm in size, but also structure on a sub-cellular (sub-micron) level. In this chapter we mainly consider radiation that is in the near infrared (NIR) region of the spectrum, for reasons that are given in section 3.2.1, and consequently the wavelength of radiation that is of most interest to us lies approximately within the 0.7 - 1.0 μm range.

The skin is a thin relatively flat organ classified as a membrane: the cutaneous membrane. It is composed of two main layers: an outer thinner layer called the epidermis and an inner thicker layer named the dermis. The deeper dermis is a relatively dense and vascular connective tissue layer that may average just over 4 mm in thickness in some body areas. Between the dermis and the epidermis is found the dermal-epidermal junction, a specialised area where the cells of the epidermis meet the connective tissue cells of the dermis. Beneath the dermis itself lies a loose subcutaneous layer that is rich in fat and areolar tissue: sometimes it is known as the hypodermis, or superficial fascia. The fat content of this layer varies with the individual state of nutrition and in obese individuals may exceed 10 cm, and whilst the hypodermis is not strictly a part of the skin it does contains the bulk of blood supplying vessels going to the dermis itself.

Figure 3.1: Anatomical diagram of skin
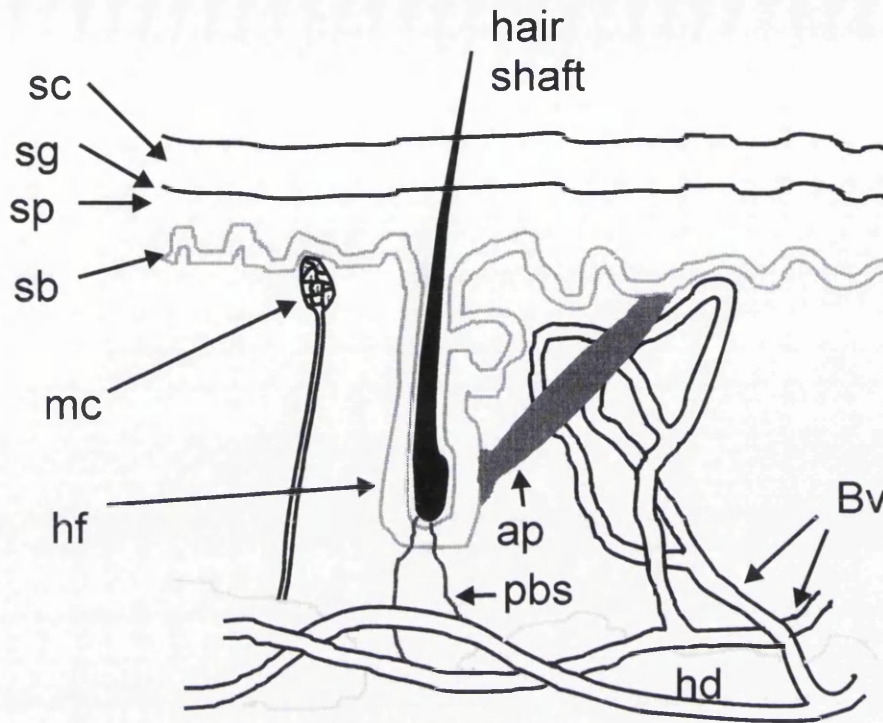
sc - stratum corneum; sg - stratum granulosum; sp - stratum spinosum,; sb - stratum basale; mc - Meissner's corpuscle; pbs - papillary blood supply; ap - arrector pili muscle; hd - hypodermis; bv - blood vessels

3.1.1 The epidermis

The epidermis of the skin is composed of stratified squamous (flat) epithelium. In "thin" areas of skin, which covers most of the body, it has a total thickness of between 1 and 3 mm, the outer epidermal layer is quite thin being typically less than 0.17 mm thick in most places. Notable exceptions to this are found in body areas such as the soles of the feet and palms of the hands where the total skin thickness may be 4-5 mm and the epidermal region may be 1-1.3 mm thick.

Epidermis is composed of several types of epithelial cells. Keratinocytes become filled with a tough, fibrous protein called keratin. These cells, which are arranged in distinct strata, are by far the most important cells in the epidermis. Comprising over 90% of the epidermal cells, they form the principal structural element of the outer skin. Melanocytes are another class of cells found in the epidermis; they contribute to

the skin colour and protect the skin from ultra-violet light by scattering and absorbing harmful wavelengths and may comprise over 5% of epidermal cells. Another type of cell, the Langerhans' cell, is also found and is believed to play a limited role in immunological reactions affecting the skin.

The cells of the epidermis are found in up to five distinct layers and each layer is characterised by certain structural or functional properties. These layers are described below in sections 3.1.1.1 to 3.1.1.5.

3.1.1.1 Stratum corneum (horny layer)

This is the most superficial layer of the epidermis and comprises of very thin (typically about 10 μm) squamous cells that are dead at the skin surface and are continuously being shed and replaced. The cytoplasm in these cells has been replaced by the water repelling protein keratin. In addition the cell membranes become thick and chemically resistant. Specialised junctions, known as desmosomes, that hold adjacent keratinocytes together strengthen this layer even more and enable it to withstand considerable wear and tear. Hence the stratum corneum serves as a protective outer skin layer but certain diseases of the skin can cause it to thicken far beyond normal limits, in a process known as hyperkeratosis, resulting in thick, dry, scaly skin that is inelastic and prone to painful fissures.

3.1.1.2 Stratum lucidum (clear layer)

The karatinocytes in this layer are closely packed and clear. Typically the cell nuclei are absent and the cell outlines are indistinct. The cells are filled with a soft gel-like substance, called eleiden, which is eventually transformed to keratin. Eleiden is rich in protein bound lipids which allows it to serve as a barrier to prevent water penetration and loss. In areas of thin skin this layer is usually absent but is highly noticeable in regions of thick skin.

3.1.1.3 Stratum granulosum (granular layer)

The process of keratinisation begins in this layer. Cells are arranged in a sheet of two to four layers deep and are filled with extremely staining granules called keratohyalin, which is required for keratin formation. Cells in the stratum granulosum have started to degenerate. As a result, high levels of lyosomal enzymes are present in the cytoplasm, and the nuclei are missing or degenerate. Like the stratum lucidum this layer of the epidermis may also be missing in some regions of the skin.

3.1.1.4 Stratum spinosum (spiny layer)

The stratum spinosum layer of the epidermis is formed from eight to ten layers of irregularly shaped cells with very prominent intercellular bridges or desmosomes. When viewed under a microscope the desmosomes joining adjacent cells give the layer a spiny appearance. Cells in this layer are rich in ribonucleic acid (RNA) and are therefore well equipped to initiate the protein synthesis required for the production of keratin.

3.1.1.5 Stratum basale (base layer)

This is a single layer of columnar cells. Only cells in this deepest stratum of the epithelium undergo mitosis. As a result of this regenerative activity, cells transfer or migrate from the basal layer through the other layers until they are shed at the skin surface.

3.1.2 The dermal-epidermal junction

Electron microscopy and histochemical studies have demonstrated the existence of a definite basement membrane, specialised fibrous elements, and a unique polysaccharide gel that together serve to cement the superficial epidermis to the dermis below. This area of contact forms a specialised junction which functions to hold the two layers together and to provide mechanical support for the epidermis. In

addition, it serves as a partial barrier to the passage of some cells and large molecules.

3.1.3 The dermis

The dermis, or corium, is composed of a thin papillary and thicker reticular layer. The dermis is always thicker than the epidermis and can exceed 4 mm on the soles and palms, although it seldom is less than about 0.4 mm. In addition to serving a protective function against mechanical injury and compression, this layer of the skin provides a reservoir storage area for water and important electrolytes. A specialised network of nerves and nerve endings in the dermis serves to process sensory information such as pain, pressure, touch and temperature. At various levels of the dermis there are muscle fibres, hair follicles, sweat and sebaceous glands, and many blood vessels.

3.1.3.1 The papillary layer

The thin superficial layer of the dermis forms bumps, called dermal papillae, which project into the epidermis. The layer takes its name from these papillae arranged in rows on its surface. Between the sculptured surface of the papillary layer and the stratum basale lies the important dermal-epidermal junction. The papillary layer and its papillae are composed essentially of loose connective tissue elements and a fine network of thin collagenous and elastic fibres. The thin epidermal layer of the skin conforms tightly to the ridges of dermal papillae. As a result the epidermis also has characteristic ridges on its surface. These epidermal ridges are especially well defined on the tips of fingers and toes and allow us to grip surfaces.

3.1.3.2 The reticular layer

The thick reticular layer of the dermis consists of a much more dense reticulum, or network of fibres, than is seen in the papillary layer above it. Although most of the fibres in this layer are of the collagenous type, which give toughness to the skin, elastic fibres are also present.

The dermis contains both skeletal and smooth muscle fibres. A number of skeletal muscles are located in the skin of the face and scalp. These muscles permit a wide variety of facial expressions and are also responsible for voluntary scalp movements. The distribution of smooth muscle fibres in the dermis is much more extensive than the skeletal variety. Each hair follicle has a small bundle of involuntary muscles attached to it. These are the arrector pili muscles which can cause the hairs to stand on end.

Unlike the epidermis the dermis does not continually shed and regenerate itself. It does maintain itself but rapid regeneration of connective tissue in the dermis only occurs in unusual circumstances, such as the healing of a wound. It is as well to note here that unusual skin surface features such as scars, moles, freckles and stretch marks may all occur and give rise to unpredictable optical properties. Hair follicles, sweat glands and sebaceous glands also can affect the tissues' optical properties.

3.2 Optical properties of skin

In this section we consider the components of absorption and scattering separately, discussing the contributions of the individual components that make them up.

3.2.1 Optical absorption spectrum of tissue

Skin consists of very many optically active components which absorb light. The most predominant of these are water, which makes up around 80% by weight of skin tissue, and the haemoglobin proteins found mainly in red blood cells, although a number of other chromophores are present. These are described below, and Figure 3.2 illustrates an attenuation spectrum for some of these components.

3.2.1.1 Water

Water absorbs strongly at wavelengths in the ultra-violet, and in the far infrared (above ~2 μm), a property that leads to use of such wavelengths in therapeutic medical optical systems; e.g. for tissue ablation where laser energy needs to be strongly absorbed so as to produce localised damage to tissue. By contrast, for wavelengths in the visible and near infra-red, scattering dominates over absorption in

tissue. Water has an extinction coefficient of around 0.02 optical densities per centimetre at a wavelength of 800 nm, but its concentration in tissue is around 55 molar. Since the absorption coefficient is the product of the concentration and the extinction coefficient, this gives a relatively high absorption due to water even though at first sight it may appear that water would not make a significant contribution.

3.2.1.2 Haem proteins

Haemoglobin is responsible for oxygen transport in the blood, and its absorption spectrum depends on its oxygenation state. Both oxygenated (HbO2) and deoxygenated (Hb) haemoglobin show high absorption in the visible region of the spectrum below about 600 nm, but above this in the near-infrared region it drops to below 0.5 mm^{-1}. However, even this is a high absorption coefficient, when compared to that of water, and it extends over a large portion of the optical spectrum, as may be seen from the absorption spectrum shown in figure 3.2. Although the extinction coefficients of these proteins are high for pure samples, their concentration in tissue is relatively low, and so their overall contribution is less than may have, at first glance, been expected: the extinction coefficient of pure haemoglobin is 0.8399 per mMol per centimetre, whereas its concentration in tissue is typically a few percent. Because of this the contribution to the overall tissue absorption spectrum from the haem proteins is of the same order of magnitude as that for water whose attenuation coefficient is very much lower but whose high concentration mitigates this factor.

3.2.1.3 Other chromophores

Absorption also occurs in other tissue chromophores, the main one being myoglobin whose absorption spectrum is similar to that of haemoglobin and which forms the oxygen store inside cells. Cytochromes are enzymes found in the mitochondrial membranes inside cells, and like haemoglobin their absorption characteristics depend on their oxygenation state. The extinction spectra of oxygenated cytochrome aa$_3$ (3.4 mM^{-1}cm^{-1} at 800 nm), reduced cytochrome aa$_3$ (1.1 mM^{-1}cm^{-1} at 800 nm) and cytochrome b (1.0 mM^{-1}cm^{-1} at 800 nm) are of the same order of magnitude as the

haemoglobin spectra, but due to their much smaller concentrations (5-20 μM) they make small contributions to tissue spectra and are subsequently ignored in the following discussions. Melanin is another important component of skin, found in varying concentrations according to skin type.

Figure 3.2: The absorption spectra of water and oxyhaemoglobin shown with the scattering region where melanin makes a contribution to the attenuation[1]

Wavelength (nm)
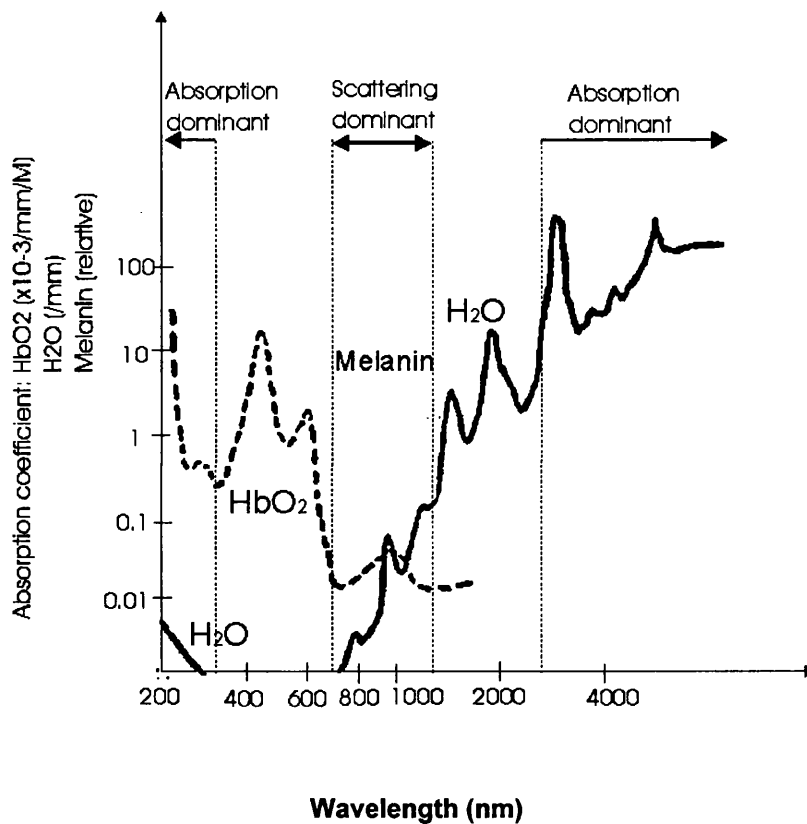
Figure 3.2 illustrates the effects, both combined and individually, of the absorption contributions for soft tissue: after Patterson et al[1]. Once the absorption spectra of all the above components, scaled by their respective concentrations are considered, it becomes apparent that there is a window of minimum absorption in the far-red to near-infrared, and for this reason these wavelengths are commonly used for diagnostic and imaging systems.

3.2.2 Scattering from tissue in the NIR

Although important, the absorption of light by tissue is only one factor, and the least important at that, in determining the overall attenuation that is observed. The major player is scattering, which makes the dominant contribution at the wavelengths of interest to us (those of the optical and near-infrared part of the spectrum). The origins of scattering in tissue are numerous and the analysis is involved, complex and incomplete at the theoretical level of description. However a number of hybrid models do exist for looking at tissue scattering which involve combining several modelling techniques for various regimes of scattering theory. We now proceed to discuss the various factors contributing to optical scattering in tissue.

3.2.2.1 Structural scattering

As skin is formed from several layers (Figure 3.1), such as the dermis and epidermis, it is necessary to consider the differing optical properties of each layer. Scattering at boundaries may also occur by reflection at refractive index mismatched boundaries, or by refraction at these boundaries. Prediction of these effects is difficult, not merely as the refractive indices of the various tissue types are not well known, but because the interfaces between the different types form irregular shaped boundaries.

3.2.2.2 Particle scattering

Since we are chiefly concerned with near infrared radiation, structure on the scale of individual cells is large compared to the wavelength of the illuminating radiation, and thus we have a scattering regime that falls neatly into that for large particles. However, because living cells are not generally a well defined spherical shape we cannot model their scattering pattern analytically. Mechanisms by which the light is scattered include those due to interference effects described by Rayleigh-Ganz-Debye theory (detailed in section 2.2.2.5). Moreover, in a general sample of skin we find more than one type of cell forming not only inhomogeneities but also layers such as the stratum corneum, the epidermis and the dermis, and this causes immense

difficulty in calculating a well defined compound scattering pattern for this combination of particles.

3.2.2.3 Membrane scattering

Besides scattering from the cellular components of tissue, it is also necessary to consider how the passage of radiation through skin is affected by the properties of cell membranes. These are considered to be thin (10 nm), flat, dielectric reflecting films of refractive index 1.46. For angles of incidence less than about 50° the reflection at 800 nm from a flat segment of membrane remains nearly constant at approximately 0.001 of the incident intensity, rising to approximately 0.01 at an angle of around 80°. Refraction effects are usually small, since the refractive index of the various tissue components are not too dissimilar, they vary from 1.33 for water to 1.55 for fat and concentrated protein solutions. It is common practice to neglect internal refraction in light transport models except at the surface interface (air-tissue), and to assume a constant refractive index for tissue: 1.4 is the value that is usually adopted.

In order to account for the fact that cells are not regular it is possible to consider a random distribution of thin films analogous to the collection of particles described earlier in the definition of the g-factor. In this case the response of a single film is multiplied by the cosine of the angle of incidence to account for the effective area of the membrane intersecting the input beam. The integrated reflectance is virtually wavelength independent, decreasing by only 6% between 600 and 1000 nm^2.

3.2.2.4 Mitochondrial scattering

Cope[2] has simulated the single scattering properties of mitochondria, which in reality are structures that are around 2-3 microns long with a volume of approximately 1 micron cubed, by treating them as volume equivalent spheres and performing Mie simulations with assumed particle radii of 0.36 microns, an internal refractive index of 1.428 and an external refractive index of 1.354. He found a wavelength

dependence of the reduced scattering coefficient proportional to $1/\lambda^{0.6}$ which is much less than for Rayleigh scattering.

3.2.2.5 Other cellular components

Structure that forms at a sub-cellular level is generally small compared to the wavelength of the illuminating radiation, and so may be treated as small particle scatterers. Many such small biological forms are known to effect scattering: such as the mitochondria mentioned above. They tend to give rise to an isotropic scattering contribution which sums with the anisotropically scattered component of the light to produce the overall scattering pattern.

Besides mitochondria there are many other scattering components in tissue. These include; cellular nuclei whose size is approximately 70 nm, each cell has two centrioles 300-500 nm long by 150 nm diameter, Golgi apparatus of a sac like structure on a scale of about 30 nm, a secretory endoplasmic reticulum whose size is around 50 nm, and various other structures upon the 100 nm and sub-100 nm scale. These components account for a large Rayleigh scattering component contributing to the overall scattering in tissue.

3.2.2.6 Backscattering

Backscattered signals may derive from either singly or multiply scattered photons. The singly scattered component may be either a specular reflection at a refractive index boundary or a backscattering event from within a homogeneous region of the medium. The multiply scattered photons are those following paths in which more than one scattering event occurs, and consequently these photons follow longer paths than their singly scattered counterparts. This also means that what absorption is present affects the multiply scattered photons more than those that are singly scattered, and this can be advantageous in improving the contrast ratio between the singly and multiply scattered signals. Thus materials of relatively high absorption coefficient form images of better contrast ratio than their lower absorption counterparts, at the expense of a reduced signal intensity at the receiving detector. It

is possible to see that this property may have applications in biological imaging whereby a tuneable wavelength source could be used to image tissue by switching between wavelengths to change the contrast ratio, for example, in order to image soft tissues more effectively.

Combining the two contributions from Mie and Rayleigh scattering, or RGD theory and Rayleigh scattering (see section 2.2.2), gives an approximate model for tissue. However such models are often not particularly good for accurately predicting the behaviour of light and may be better used to indicate the expected magnitude of the scattering coefficients. For this reason the Monte Carlo method of chapter 4 for modelling light transport in tissue was adopted.

3.3 Optical parameter values for skin and its components

The optical properties of a medium are characterised by three main parameters: the absorption coefficient, scattering coefficient, and the anisotropic phase function. Often the exact form of the phase function is unavailable, and in this case an approximation to the phase function can be created using the anisotropic g-factor. In some cases, such as in some Monte Carlo models, a full phase function is necessary, and in these cases a function is often constructed using the g-factor and the Henyey-Greenstein equation (see section 4.4.2). This is valid for highly forward scattering media, and provides a reasonable model for tissue such as skin in the diffuse regime and where scattering dominates over absorption. The refractive index of the tissue is important mainly at the air/tissue interface where it affects the degree of internal reflection.

We have already said that it is difficult to determine the optical transport coefficients in highly scattering media, and this is reflected by the relatively small amount of data that has been published for skin. Of the work that has been published to date, the bulk has been with the red light from HeNe lasers[3], with comparatively little in the near-infrared, and the majority of these data have been measured upon *in vitro* samples. Measurements using *in vivo* samples are made more difficult because, generally, experiments need to measure both the reflected and transmitted light

52

intensities, and also because the tissue is inhomogeneous making separation of signal components from different tissue layers difficult.

The three main optical parameters are usually derived from three different sets of measurements using the following method[3,4,21]. Firstly the total attenuation of a collimated beam through a section of tissue is measured to obtain the value of μ' (section 2.2.2.3.1). Then measurements of the diffuse reflectance and transmittance through the sample are made using a pair of integrating spheres, and from these are derived the absorption and reduced scattering coefficients.

Finally the phase function, and subsequently the g-factor, is measured by illuminating a thin slab of tissue with a collimated beam of light, (so that multiple scattering in the sample is insignificant) and using a goniometer to measure the reflected or transmitted light at different angles.

Cheong[5] reviewed the published data on optical parameters for various types of tissue, and explained the methods used to derive them. These data verify that scattering forms by far the largest contribution to the overall attenuation of light for a section of skin. Typically $\mu_a \approx 0.04$ mm^{-1} and $\mu_s \approx 10\text{-}20$ mm^{-1} in the linear attenuation region, hence often the contribution of absorption to the overall attenuation can be, and is often, ignored. In addition, papers published by Anderson and Parrish[6] and van Gemert[7] have focused solely on skin optics. Reported values for skin tissue parameters are given in the tables below.

3.4 Summary of physical and optical properties of skin

Skin can be simplified as a three strata medium: stratum corneum, epidermis and dermis. The stratum corneum forms the surface skin layer, and has a thickness of about 10-100 μm. It is formed from layers of dead keratinised cells with a high lipid and protein content, but has only a low water content. Although it rapidly gives rise to diffusion of light, due to its high scattering coefficient (~200 mm^{-1}), this fact is mitigated by the fact that it is such a thin layer. Below the stratum corneum lies the epidermis, which itself consists of several layers, and which has a much lower scattering coefficient than the stratum corneum, but with a typical thickness of

around 100 microns. Finally the dermis lies below the epidermis. It has a typical thickness of 2-4 mm, where again, the scattering coefficient is lower than for that of the stratum corneum (see the tables below), but here the absorption is mainly due to the haem proteins found in red blood cells in the network of capillaries in this layer. The dermis may also include blood vessels.

Table 3.1: Some published results for optical parameters in human tissue

Author	Values measured and conditions of measurement
Reynolds et al[8]	Blood; 800 nm; forward scattering cross-section 42.03 μm^2; backscattering cross-section 0.21 μm^2; absorption cross-section 0.131 μm^2
Anderson and Parrish[9]	Stratum corneum; refractive index = 1.55 at 633 nm
Bruls and van der Leun[10]	Epidermis in the visible; $\mu_s \approx 50$ mm^{-1}; $\mu_a \approx 4$ mm^{-1} ; $g \approx 0.75$
Gemert et al[11]	At 800 nm: Dermis; $\mu_s = 40$ mm^{-1}; $\mu_a = 0.4$ mm^{-1}. Epidermis; $\mu_s = 43$ mm^{-1} ; $\mu_a = 4$ mm^{-1}
Pederson et al[12]	Blood in the visible; $\mu_s \approx 150$ mm^{-1}; $\mu_a \approx 0.5$ mm^{-1} ; $g \approx 0.99$
Jacques et al[13]	Dermis *in vitro*; at 633 nm; μ_s=18.7 mm^{-1}; μ_a=0.27 mm^{-1}; $g = 0.91$
Prahl[14]	Bloodless human dermis; at 800 nm; $\mu_a = 0.09$ mm^{-1}; $\mu_s = 7.0$ mm^{-1}
Steinke and Shepherd[15]	Blood; at 633 nm; concentration from 0.5-1.5%; scattering cross-section 76.31-87.34 μm^2
Marchesini et al[16]	Dermis; at 635 nm; $\mu_s = 24.4 \pm 2.1$ mm^{-1} ; $\mu_a = 0.18 \pm 0.02$ mm^{-1}. Breast tissue; $\mu_s = 39.5 \pm 3.5$ mm^{-1}; $\mu_a < 0.02$ mm^{-1}; $g = 0.85$-0.92
Cope[2]	Refractive index of pure lipids and concentrated protein solutions = 1.5
Schmitt et al[17]	At 1300 nm; Stratum corneum $\mu_s = 1.5$ mm^{-1}. Dermis $\mu_s = 4.6$-5.0 mm^{-1}

Schweiger[18]	Stratum corneum in visible and UV; $\mu_s \approx 250$ mm^{-1}; $\mu_a \approx 10$ mm^{-1} g ≈ 0.9
Tuchin et al[19]	At 633 nm; Epidermis $\mu_s = 10.7$ mm^{-1}; $\mu_a = 0.43$ mm^{-1}; g = 0.79; refractive index = 1.5. Dermis $\mu_s = 18.7$ mm^{-1} ; $\mu_a = 0.27$ mm^{-1} ; g = 0.82; refractive index = 1.4
Treweek and Barbenel[20]	Breast skin; at 633 nm; $\mu_s = 40$ mm^{-1} ; $\mu_a = 1.0$ mm^{-1}
Simpson et al[21]	At 851 nm; Caucasian dermis; $\mu_s' = 1.7567$ mm^{-1} ; $\mu_a = 0.0122$ mm^{-1}
Gobin et al[22]	At 633 nm; Palm of hand $\mu_s' = 1.2$ mm^{-1} $\mu_a = 0.08$ mm^{-1}. Back of hand $\mu_s' = 1.4$ mm^{-1} $\mu_a = 0.18$ mm^{-1}. Pigmented white skin $\mu_s' = 1.3$ mm^{-1} $\mu_a = 0.218$ mm^{-1}. Non-pigmented white skin $\mu_s' = 1.3$ mm^{-1} $\mu_a = 0.135$ mm^{-1}. Dermis $\mu_s' = 1.1$ mm^{-1} $\mu_a = 0.1$ mm^{-1}

Chapter References

[1] M. S. Patterson, B. C. Wilson and D. R. Wyman, "The propagation of optical radiation in tissue," (Parts I and II), *Lasers in Med. Sci.*, Vol. 6, No. 2, pp. 155-168 and Vol. 6, No. 4, pp. 379-390, 1991

[2] M. Cope, *The development of a near infrared spectroscopy system and its application for non invasive monitoring of cerebral blood and tissue oxygenation in the newborn infant*, (PhD thesis, University College London, 1991)

[3] S. L. Jacques, C. A. Alter and S. A. Prahl, "Angular dependence of HeNe laser light scattering by human dermis," *Lasers in the life sciences*, Vol. 1, No. 4, pp. 309-333, 1987

[4] M. S. Patterson, B. C. Wilson and D. R. Wyman, "The propagation of optical radiation in tissue," (Parts I and II), *Lasers in med. sci.*, Vol. 6, No. 2, pp. 155-168 and Vol. 6, No. 4, pp. 379-390, 1991

[5] W. F. Cheong, S. A. Prahl and A. J. Welch, "A review of the optical properties of biological tissues," *IEEE J. Quan. Electronics*, Vol. 26, No. 12, pp. 2166-2185, 1990

[6] R. R. Anderson and J. A. Parrish, "The optics of human skin," *J. of Inv. Derm.*, Vol. 77, pp. 13-19, 1981

[7] M. J. C. van Gemert, S. L. Jacques, H. J. C. M. Sterenborg and W. M. Star, "Skin Optics," *IEEE Transactions on biomedical engineering*, Vol. 36, No. 12, pp. 1146-1154, 1989

[8] L. Reynolds, C. Johnson and A. Ishimaru, "Diffuse reflectance from a finite blood medium: applications to the modelling of fiber optic catheters," *Appl. Opt.*, Vol. 15, No. 9, pp. 2059-2067, 1976

[9] R. R. Anderson and J. A. Parrish, "The optics of human skin," *J. of Inv. Derm.*, Vol. 77, pp. 13-19, 1981

[10] W. A. G. Bruls and J. C. van der Leun, "Forward scattering properties of human epidermal layers," *Photochem. Photobiol.,* Vol. 40, pp. 231-242, 1984

[11] M. J. C. van Gemert, S. L. Jacques, H. J. C. M. Sterenborg and W. M. Star, "Skin optics," *IEEE Biomed. Eng.,* Vol. 36, No. 12, pp. 1146-1154, 1989

[12] G. D. Pederson, N. J. McCormick and L. O. Reynolds, "Transport calculations for light scattering in blood," *Biophys. J.,* Vol. 16, pp. 199-207, 1987

[13] S. L. Jacques, C. A. Alter and S. A. Prahl, "Angular dependence of HeNe laser light scattering by human dermis," *Lasers in the life sciences,* Vol. 1, No. 4, pp. 309-333, 1987

[14] S. A. Prahl, *Light transport in tissue,* (PhD thesis, University of Texas at Austin, 1988)

[15] J. M. Steinke and A. P. Shepherd, "Comparison of Mie theory and the light scattering of red blood cells," *Appl. Opt.,* Vol. 27, No. 19, pp. 4027-4033, 1988

[16] R. Marchesini, A. Bertoni, S. Andreola, E. Melloni and A. E. Sichirollo, "Extinction and absorption coefficients and scattering phase functions of human tissues *in vitro,*" *Appl. Opt.,* Vol. 28, No. 12, pp. 2318-2324, 1989

[17] J. M. Schmitt, A. Knuttel and R. F. Bonner, "Measurement of optical properties of biological tissues by low-coherence reflectometry," *Appl. Opt.,* Vol. 32, No. 30, pp. 6032-6042, 1993

[18] M. Schweiger, *Application of the finite element method in infrared image reconstruction of scattering media,* (MPhil transfer report, University College London, 1993)

[19] V. V. Tuchin, S. R. Utz and I. V. Yaroslavsky, "Tissue optics, light distribution, and spectroscopy," *Opt. Eng.,* Vol. 33, No. 10, pp. 3178-3188, 1994

[20] S. P. Treweek and J. C. Barbenel, "Direct measurement of the optical properties of human breast skin," *Med. & Biol. Eng. & Comp.,* Vol. 34, No. 4, pp. 285-289, 1996

[21] C. R. Simpson, M. Kohl, M. Essenpreis and M. Cope, "Near infrared optical properties of *ex-vivo* human skin and subcutaneous tissues measured using the Monte Carlo inversion technique," *Phys. Med. Biol.,* Vol. 43, pp. 2465-2478, 1998

[22] L. Gobin, L. Blanchot and H. Saint-Jalmes, "Integrating the digitized backscattered image to measure absorption and reduced-scattering coefficients *in vivo,*" *Appl. Opt.,* Vol. 38, No. 19, pp. 4217-4227, 1999

The Monte Carlo Simulation

4.1 Chapter overview

This chapter details the Monte Carlo simulation used to simulate the experimental system shown in Figure 1.2. It is broken down into several sections dealing respectively with an initial brief historical perspective describing how the simulation developed over the years at UCL (section 4.2), followed by a general overview of the Monte Carlo simulation (section 4.3), followed finally by a detailed description of the component parts of the simulation itself (section 4.4). The detailed description of the simulation basically follows the functionality that was coded into the simulation and begins by describing the components of the C function main() from where the simulation program began execution. Following this and a general outline of the functions contained within this function, the subfunctions therein are also described, and followed in a descending hierarchical tree-like map until all the component parts of the simulation and the logic encoded therein has been described. The flowcharts of this chapter act as a map to indicate where one section of code fits into the overall simulation and its relation to the other sections of code: Figure 4.2 is a flowchart showing the main flow of control for the simulation and Figure 4.5 illustrates the step of performing a random walk in greater detail than is shown in Figure 4.2. This chapter therefore reads somewhat like a user manual or programmer's guide written for the simulation.

4.2 Historical background of the Monte Carlo simulation

The Monte Carlo method itself has long been used at UCL to model light transport through tissue, and much credit for the original programming must go to P. van der Zee[1], M. Essenpreis[2], D. Kirkby[3] and M. Eddowes[4], although many others added modifications and improvements.

The actual coding of the Monte Carlo simulation was in the C programming language, and began as a translation and modification of an original program written in Pascal by Miles Eddowes[4]; a program which was itself based upon models written by van der Zee[1] and Essenpreis[2]. Some of the linear nature of the Pascal program coding remained, in the form of a large number of global variables, although an

57

attempt was made to modularise the code into a set of functions as far as possible. This was done to adopt the common practice in industry of coding in a modular way to make large projects easier to write when using more than one programmer, such code being easier to maintain, and easier to upgrade and modify at a later date. Modularising the code also localises the effect of variables contained in the modules, which confines effects locally and makes it easier to debug.

The original Pascal version of this program was based on the program "copeak," written by Miles Eddowes, which was designed to look at coherent backscatter peaks in tissue due to photons taking reciprocal paths and giving rise to localised interference peaks in the backscattered direction[4]. This version was designed to run on a Sun workstation, and used look-up tables for values of sine and cosine to speed up calculations. However, due to the availability of maths coprocessors using hard coded look-up tables and compilers that are optimised for use with these coprocessors, this technique was largely obsolete at the time of writing our Monte Carlo simulation and direct calls to the C library functions sin() and cos() were preferred instead.

In the model used by Essenpreis[2], the calculation of Fresnel reflected and transmitted components was also achieved by using a look-up table to speed computation, and we followed this convention.

Programming was undertaken using the Microsoft Visual C++™ compiler versions 1.0 and 1.5, and was run as both a 16-bit QuickWin™ program and MS-DOS™ executable on several 80486 and Intel Pentium™ personal computers.

4.3 An overview of the Monte Carlo simulation technique for photon tracing in tissue

The model implemented a simulation of a blood vessel embedded in a three layered slab, and is shown in Figure 4.1. Analysis of the output, including the output scan, from the model forms the topic of discussion for the next chapter; this chapter deals with simulating photons incident upon the sample surface, the tracing of their passage through the sample and the recording of any photons that leave the sample surface.

Figure 4.1: Simulated core model sample
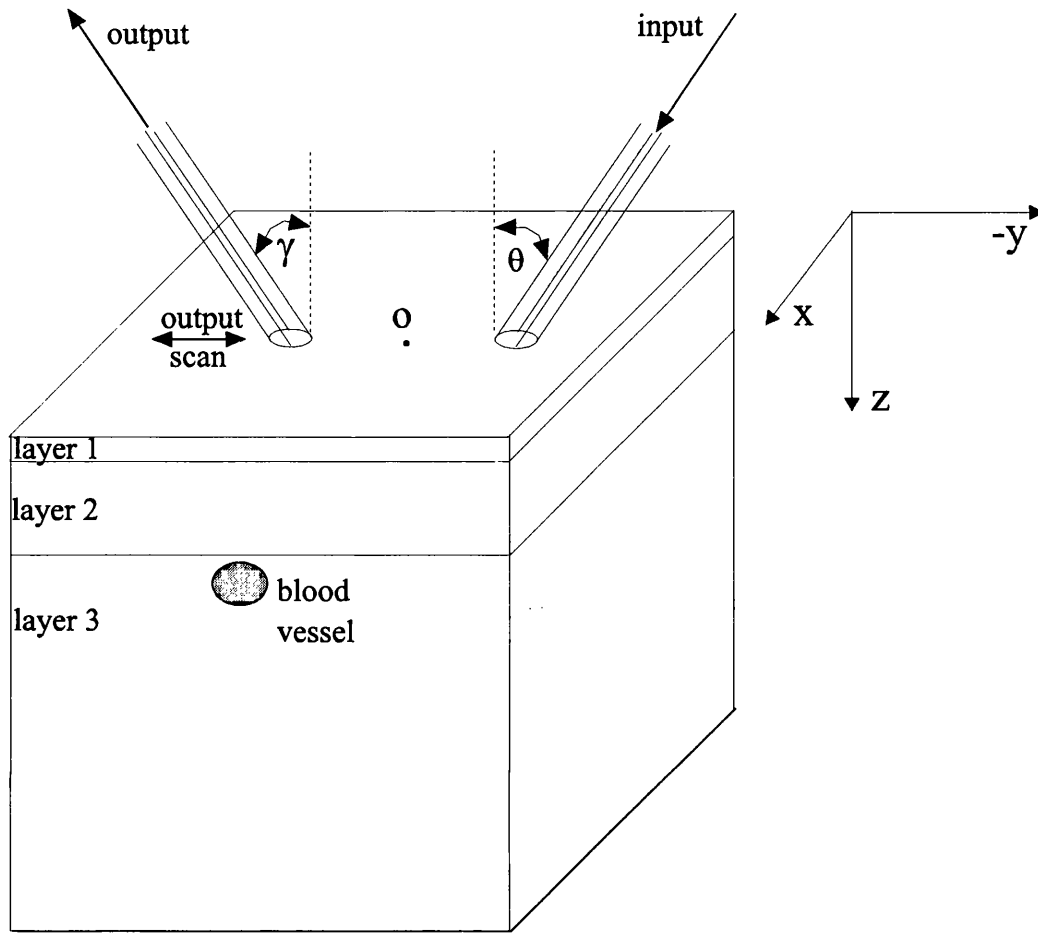
θ is the incident beam angle defined as that measured between the normal to the surface at the point of photon incidence and the incident photon trajectory: the photons themselves had no x-component of motion. θ was held constant during a simulation.

The optical Monte Carlo technique used in this thesis worked by injecting photons into a computer simulated sample of known optical properties one by one and tracing their progress through that sample. Photons were made to obey deterministic laws of physics in the sample, for example they underwent refraction at refractive index boundaries according to Fresnel's laws, but their progress though the sample was dictated by selecting their path length and direction stochastically from the known properties of the sample in which they were travelling.

In all simulations photons were selected according to one of three input beam profiles. The simplest was a point input beam profile incident at a fixed point on the sample surface. The point beam gave rise to an infinitely narrow beam of light impinging on the sample surface, and approximated a perfectly focused input probe beam. The other two cases were for beams of finite width having either a top-hat intensity profile or a Gaussian intensity profile, both of which were collimated beams in which the incident photons followed trajectories which were parallel to their neighbours. In the latter two cases the starting co-ordinates of the photon were chosen at random from either a uniform distribution or a Gaussian distribution, centred on a user defined central input point, independently in both the x- and y-directions so as to simulate a 2-dimensional beam profile incident on the $z = 0$ surface. The top-hat profile simulated a beam of constant intensity across its width, and the Gaussian beam simulated the more realistic situation of a beam whose intensity profile was Gaussian across its width. The use of different beam input profiles permitted a comparison between them to see if or how the beam profile effected the emergent coherent signal and overall signal-to-noise ratio. The centre of any of the incident beams simulated was always made to lie in the $x = 0$ plane; both for simplicity and because the simulated sample was symmetrical with respect to the x-axis.

The photons selected according to the preceding beam profiles were injected into the sample at a user defined angle θ and with an initial path length selected according to their perpendicular distance in the $z = 0$ plane from the line parallel to the x-axis passing through the centre of the input beam profile. Biasing the initial optical path length of the photons in this way accounted for the spatial coherence of the input beam, which was assumed to be uniform across its perpendicular cross-section.

Individual photons were processed until they were terminated either by going beyond the user-definable model bounds (set to be 20 x 20 x 20 mm in all our simulations)[*],

_____

[*] On average the energy of a photon beam travelling an optical path of 20 mm through tissue (whose value of μ_s is 10 mm^{-1}) is attenuated by a factor of e^{-200} which is well below the quantum noise detection limits of a detector; and hence a depth limit of 20 mm was considered justified as a cut-off.

dropping below a user-defined minimum cut-off weight (usually of the order of 10^{-15}) or by leaving the sample at its surface having been recorded in an output array.

4.3.1 Simulation of planar layers

Planar layers were used to simulate approximately the layers of skin; stratum corneum, epidermis and dermis. These layers were of constant thickness, refractive index, scattering coefficient and absorption coefficient, and lay in the x-y plane. The boundaries of such layers were defined by an upper- and lower-z-coordinate, and all of the layer parameters were defined in user-defined initialisation files.

4.3.2 Inclusion of blood vessels

We simulated a single blood vessel. This was defined as a single cylinder embedded completely in one of the layers. The central axis of the cylinder lay in the $y = 0$ plane, thus making the cylinder symmetrical about the x-axis. The cylinder diameter and central axis depth could also be varied by user defined initialisation parameters. The cylinder was of uniform refractive index, scattering and absorption coefficient, with values chosen to simulate blood. The boundary of the cylinder was defined by a radial distance from the central cylinder axis.

4.4 Running the Monte Carlo simulation

The overall simulation fell into two stages; the first was an initialisation of variables and parameters that need only be performed once (numbers 1 to 6 in Figure 4.2). The second step involved the actual simulation itself following the method outlined in section 4.4.3, and finally the data blocks that were saved to disk needed to be analysed: the latter analysis stage forms the discussion topic of the next chapter. The following chapter headings describe the actions performed at each of the numbered stages in the flow diagram describing the function main() (see Figure 4.2 below).

Figure 4.2: Outline of the main program control
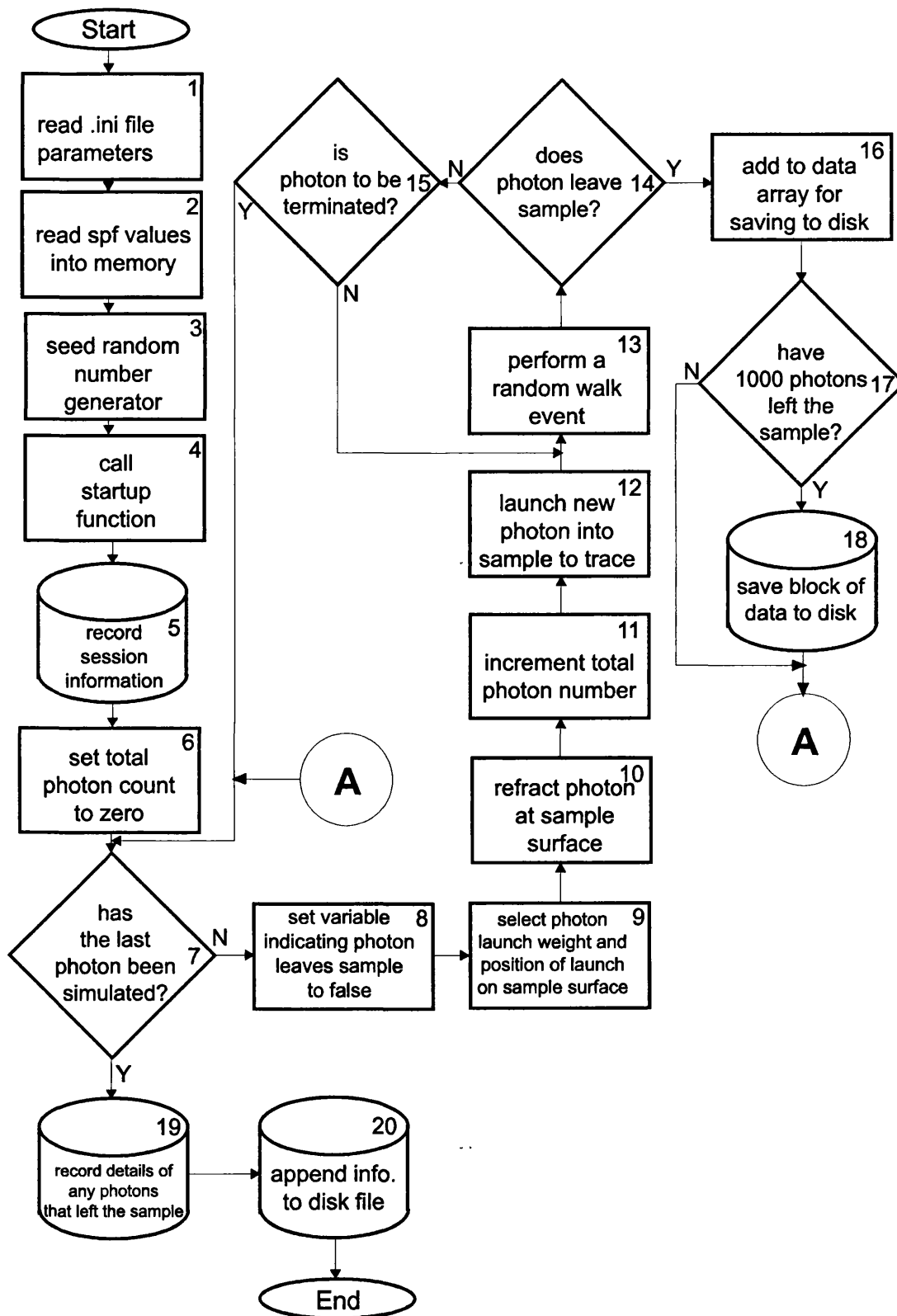
4.4.1 Overview of the function main()

Since the function main() is where a C program begins execution, it generally contains all the main flow of control for the program, the details being filled in by calls to various subroutines. The flow of control of main() was such as to perform an initialisation once (section 4.4.2) and then to initialise and simulate individual photons travelling through the sample (section 4.4.3).

The function main() tracked the number of photons actually simulated and compared this to the number that were required to be simulated in order to determine when to stop the simulation. Every photon leaving the sample surface had its details recorded in a structured array for output to a hard disk file. Once 1,000 of such photons had been recorded the data array was saved to disk and then flushed so that it became available to be overwritten with new data. Writing every 1,000 photons to disk was a safeguard against software crashes and power failures, and was necessary because the time needed to do a typical simulation was large: furthermore, it allowed the computer running the simulation to be shut down and restarted with the loss of no more than a maximum of about 10 minutes' simulation time.

4.4.2 Initialisation

The initialisation stages of the simulation needed only to be performed once when the simulation was started; they corresponded to stages 1 to 6 shown in Figure 4.2. Each stage of the process is now described.

The first stage of the initialisation process (numbered 1) was to read the initialisation file parameters from a user modifiable text file. Use of such a file allowed the simulation code to be compiled once and to modify the starting conditions for the simulation without re-compiling hard coded variable values for each run. This had the further advantage that it allowed the easy creation of a list of sets of individual starting parameters which were kept as an archive for reminding the user which starting parameters were used to create which data sets.

The initialisation file was copied into a file named "copeak.ini" which the simulation expected to find in the same directory as the simulation executable code itself. It contained a list of the following parameters for varying the starting conditions of the

simulation: the total number of photons that were required to be simulated (typically 500,000); the input beam diameter; the beam profile of the beam incident upon the surface of the sample ("input" in Figure 4.1, and which could either be a Point, a Tophat, or a Gaussian); the incident direction cosines of the input beam on the sample surface used to define the angle of incidence at the surface θ; the central point of the input beam on the sample surface, the refractive index of layers 1 to 3; the thickness of layers 1 to 3; the absorption coefficient of layers 1 to 3; the scattering coefficient of layers 1 to 3; the depth of the blood vessel; the diameter of the blood vessel; the absorption coefficient of the blood vessel; the scattering coefficient of the blood vessel; the refractive index of the blood vessel; the minimum cut-off weight for a photon; the maximum size of the sample in the x-direction; the maximum size of the sample in the y-direction; the output base filename; and any additional user comments that were desired for later reference.

The second stage of initialisation (numbered 2 in Figure 4.2) involved setting global variables describing the scattering properties of the layers. Function look-up tables were initialised by reading predefined values from text-based data files saved upon the hard disk drive and located in the same directory as the executable program code. Two such sets of look-up tables were previously populated using data calculated from the Henyey-Greenstein equation[5,6] for scattering phase functions (refer again to chapters 2 for a description of the scattering phase function) having g-values of 0.9 and 0.995 respectively. The former was used for the tissue layers 1 to 3 throughout the simulation and the latter for the blood vessel. The scattering phase function was thus fixed for each tissue type during all of the simulations performed, and no account of possible variations from the values shown was investigated[*].

Once the scattering phase function tables had been initialised, the initialisation process proceeded to seed the pseudo-random number generator from the system

---

[*] In this respect our simulation differed from that found for real skin, in that stratum corneum has a g-factor of approximately 0.7. Use of a g-factor of 0.9 was due to the fact that our simulation was developed alongside an experimental system in which the tissue phantoms we had made had their g-factor set to be 0.9. The original intention was to compare results from our experiments to those derived from the simulation described in this chapter.

clock (step 3 of Figure 4.2). The generator was of the Box-Müller type[7] and worked by creating an array of 100 random numbers using the standard C library function and then choosing a further random number which was used to index that array: the number chosen at the randomly indexed position was then returned as the random number to use in the simulation. This elaborate generation process was necessary to prevent the cycling of the random number sequence produced by the random number generator. Such sequence cycling is known to occur when the standard C random number generation function is used[3], and would corrupt simulation data were a modified random number generator not used. It would be a particular problem for coherent photon tracing where repeat paths taken by successive photons, caused by repeating sequences of pseudo-random numbers, would give rise to false estimates of the coherent signal. The Box-Müller approach we adopted eliminated the problem of random number sequence cycling, but with a penalty of an increase in the time taken to run the simulations.

As an aside, disabling the random number generator and seeding with the same value was found to be a useful device when debugging the program, as it enabled the rapid retracing of program execution to a point near to or at a known point of failure or error from where stepping could be performed one statement at a time to find the precise statement where the error occurred.

At step number 4 in Figure 4.2, the function named startUp() was called. This function initialised certain parameters that only needed initialising once. It set a parameter indicating which layer the blood vessel was in by calculating this from the data contained in the initialisation file "copeak.ini". Further, at this point a set of look-up tables was calculated for the Fresnel reflection coefficients for photons going from each different material found in the simulation to each neighbouring material. The Fresnel coefficients were based on randomly polarised light, and were the average of the parallel and perpendicularly polarised components[5]. Any total internal reflection (TIR) was taken into account by the look-up tables having a reflection probability of 1.0 for angles of incidence ϕ (the angle formed between a photon's trajectory and the normal to the refractive index boundary) greater than that necessary to give rise to TIR: rouletting [see section 4.4.4.4] using a reflection probability of unity gave a reflected photon every time. The sets of reflection

coefficient tables populated according to equation 4.2 (below), allowed for integer indexing to find reflection coefficients during the main simulation, and thereby speeded up the process of adjusting the photon weight whilst the simulation ran.

At normal incidence to a plane surface the reflection coefficient, R, for a photon passing from a material of refractive index n_1 to a material of refractive index n_2 is given by the following equation,

$$R = \left(\frac{n_1 - n_2}{n_1 + n_2} \right)^2 \tag{4.1}$$

This changes for photons incident at an angle ϕ with respect to the normal to the surface according to the following relationship,

$$R = \frac{1}{2} \left(\frac{\sin^2(\phi - \phi_r)}{\sin^2(\phi + \phi_r)} + \frac{\tan^2(\phi - \phi_r)}{\tan^2(\phi + \phi_r)} \right) \tag{4.2}$$

where the incident angle ϕ and the angle of refraction ϕ_r are related by Snell's law: $\sin \phi = k \sin \phi_r$. The relative refractive index of the two layers is $k = \frac{n_r}{n}$.

Snell's law was used further to relate the direction cosines of the transmitted and incident photons. The transmitted photon's direction cosine, $du3_r$ was modified by refraction from that incident at the boundary, $du3$, according to the equation,

$$du3_r = \sqrt{1 - k^2 (1 - du3^2)} \tag{4.3}$$

and the transmitted x- and y-direction cosines, $du1_r$ and $du2_r$, were then normalised according to the rule for direction cosines that:

$$du1_r^2 + du2_r^2 + du3_r^2 = 1 \tag{4.4}$$

At step 5 in Figure 4.2 data relating to the simulation was copied into a data file which resided in a directory along with the data files themselves. This file was given the same name as the data and served as a label for future reference. It incorporated such information as: the date and time of the simulation, the input beam profile, and

66

the properties of the layers and embedded cylinder. Following the creation of this file, the main counters for the total number of photons and interactions were set to zero and the main simulation itself was begun.

The simulation injected one photon at a time into the sample at the surface until the total number of photons that were to be simulated had been traced through the sample. Usually this number was 500,000. Each photon had various parameters associated with it, some of these represented physical quantities, such as the weight which corresponded to the energy of the photon, and some were merely parameters used in the simulation itself, and which had no physical counterpart, such as designating whether the photon was heading up or down, or was about to leave the sample.

4.4.3 Launching a new photon

We now describe the iterative part of the main procedure which fell into essentially two nested component parts. The outermost control loop, consisting of steps 7-12, created a new photon and controlled the number of such new photons created to ensure that the simulation ran the desired number of photons for the whole simulation. Embedded in that control loop was another loop, the major component of which is shown schematically as 13 in Figure 4.2, which performed a random interaction between the photon being traced through the sample and the material in that sample.

The outermost loop first checked, at step 7, to see if any more photons were required to be simulated. If there were more to do, processes 8 to 12 were invoked to create a new photon infinitesimally close to, but just below, the uppermost surface of the sample. One of the trace variables photonLeavesSample was reset to indicate that the photon was not about to exit the sample surface (step 8), this prevented the simulation from inadvertently recording the photon as data to record at step 14 and was a default starting parameter for each new photon.

At step 9 the profile of the beam, as defined in the initialisation file read at step 1, was used to determine the starting x- and y- co-ordinates of the photon (x_{start}, y_{start}, 0). For a point beam profile this was merely the centre point of the input beam

(x_{centre}, y_{centre}, 0), which was again defined in the initialisation file. For a beam whose profile was top-hat, a uniform distribution of random numbers was used to select points in both the x- and y-directions according to the beam width defined in the initialisation file. The algorithm selected a random number between -0.5 and 0.5 multiplied this by the beam width in the x-direction and then added this value to the central point x-value. An analogous algorithm was applied to determine the starting point in the y-direction.

The algorithm for determining the starting point for a Gaussian distribution of photons at the sample surface was similar in principal to that for the top-hat profile in that a beam width was defined in the initialisation file. However, in this case the cut-off value defining the absolute width of the beam was not so well defined, and the value supplied for the beam width was used to define the Gaussian beam's $\frac{1}{e}$ width.

The Box-Müller random number generator[7] was used to select random numbers from a Gaussian profile and these were multiplied by the beam width in the x-direction. This result then formed the offset added to the beam centre x-coordinate x_{centre} to give a Gaussian beam profile of the required $\frac{1}{e}$ width distributed about the central starting x-coordinate. As for the top-hat distribution, an analogous process was repeated to select an initial y-coordinate for the photon: the value found being added to the value y_{centre}.

Both the top-hat and Gaussian beam profile generation algorithms accounted for the fact that the beam width was extended in the y-direction by a factor of $\frac{1}{\cos\theta}$ when the surface input beam was tilted with respect to the z-axis. Thus the simulation automatically accounted for the effect of the changing shape of the input beam profile at the sample surface when a beam of circular cross section was not normally incident upon the sample surface.

Figure 4.3: Biasing the photon's initial optical path length
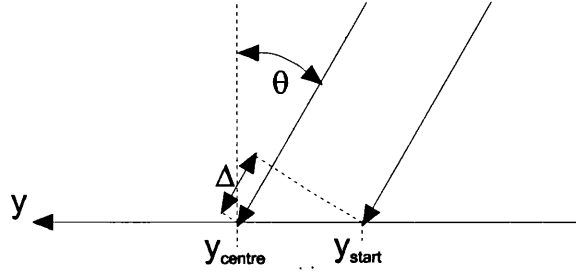
During step 12 the photon initial optical pathlength was set to account for the tilt of the beam with respect to the surface normal (see Figure 4.3). As mentioned in 4.3 above, this permitted the incident beam to be essentially spatially coherent across the entire beam width in a plane normal to its direction of motion. The optical pathlength Δ was set depending upon the difference between the y-coordinate of the centre of the input beam (y_{centre}) and the y-coordinate of the randomly selected starting position on the sample surface (y_{start}) according to the following equation:

$$\Delta = \left(y_{centre} - y_{start}\right) \cdot \sin\theta \qquad (4.5)$$

Finally, before iterative processing began, the photon was refracted into the sample and its weight reduced according to the Fresnel transmission coefficient calculated from a look-up table for the given angle of incidence. The reflected portion of the photon's weight was discarded because it was added in later during analysis according to the method described in chapter 5.

4.4.4 Iterative photon tracing

Iterative photon tracing entailed i) selecting a random scattering length, ii) testing the photon to see if it crossed any boundaries or needed to be terminated and iii) selecting a random scattering direction for the photon and repeating the process from i) until the conditions required to terminate the photon were met. A general overview of the scattering geometry involved is shown below in Figure 4.4 for illustrative purposes only. It shows a random scattering event, of path length r_n in a direction (ψ,ω) with respect to the coordinate frame orthogonal to the preceding scattering

path, following an initial preceding scattering event of path length r_{n-1} in a direction (Ψ,Ω) with respect to the (x,y,z) coordinate frame.

Figure 4.4: Particle scattering coordinate geometry
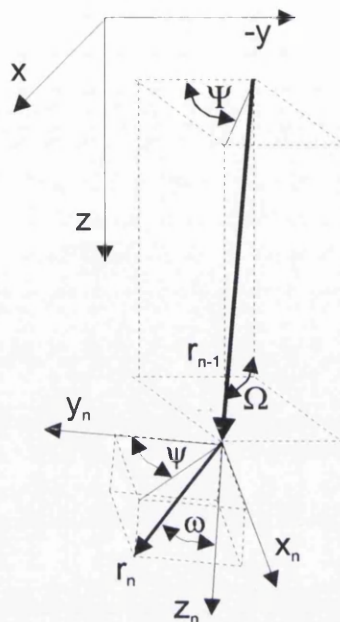
The core logic of this iterative process was encapsulated by step 13 of Figure 4.2 above, which was itself further sub-divided according to the flowchart illustrated below in Figure 4.5.

When the simulation began the iterative process (step 13) for a new photon for the first time, the check performed at step 22 calculated a random scattering length (see equation 4.6 below) based upon the optical scattering coefficient of the layer in which the photon was in without changing the direction cosines of the photon. This was done to ensure that photons were not scattered into another direction in the sample before they had penetrated by a first randomly selected depth.

Figure 4.5: Performing a random walk event
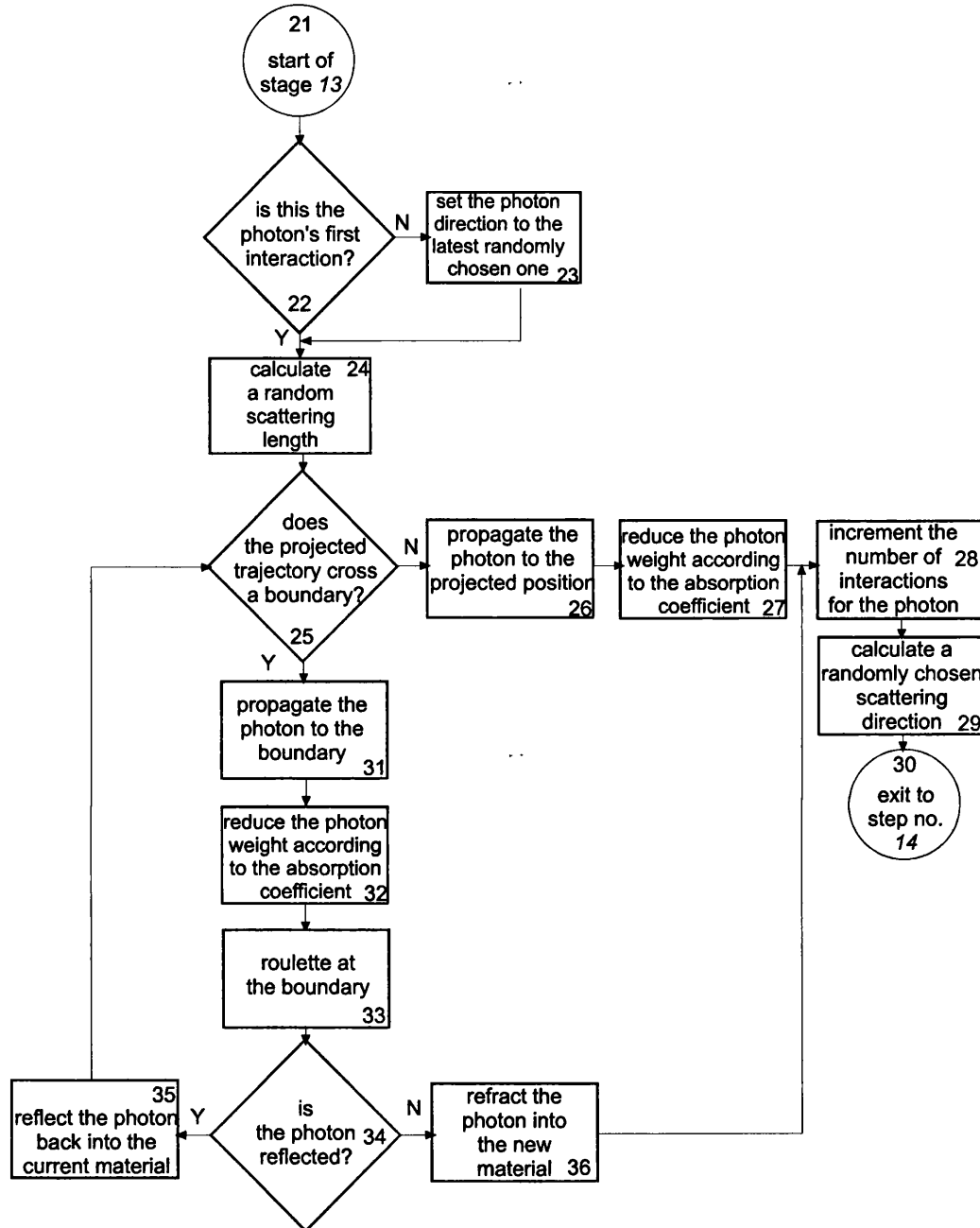
4.4.4.1 Selecting a new random scattering length

For each iteration an interaction length (at step 24) was calculated by sampling the probability distribution of free paths dictated by μ_s for the material in which the photon was travelling. A random number was used to seed the following equation from which a value for the scattering length, r_n, was returned:

$$r_n = \frac{\ln(N_{ran})}{\mu_s}$$
(4.6)

where $0.0 < N_{ran} \leq 1.0$.

4.4.4.2 Testing if a boundary was crossed

Once the scattering length was calculated, another function was then called (at step 25) to check if, based upon the current trajectory, the projected photon position using the randomly selected scattering path length would cause the photon to cross any physical boundaries defined within the simulated sample. These boundaries could be either those associated with interfaces defined between the planar layers or those between the cylindrical blood vessel and its surrounding tissue. The results of these tests (given in sections 4.4.4.2.1 to 4.4.4.2.5) determined how the photon position was calculated at the end of the iteration according to the various possibilities outlined in section 4.4.4.3 below: if no internal boundary was crossed then the photon was propagated to its projected position (step 26), otherwise the photon was propagated to the nearest boundary where its fate was decided by the rouletting process described in section 4.4.4.4 below.

Boundary crossing tests were performed dependent upon where the photon was starting a random scattering event from. There were three cases to consider: 1) the photon started in a plane layer without an embedded cylinder, 2) the photon started in a plane layer with an embedded cylinder and 3) the photon started from within the cylinder itself. These three cases are discussed in the following sections numbered 4.4.4.2.1 to 4.4.4.2.5.

Several parameters were used to help to track the photons and determine if they crossed refractive index boundaries: a) an integer parameter was used to track the layer in which the photon was currently, this being incremented and decremented according to the photon's movements across planar layer boundaries; b) a fixed parameter was used to indicate which layer the cylinder was in, the layers being numbered 0 to 2 with 0 being that layers closest to the surface of the sample (i.e. whose uppermost boundary lay in the $z = 0$ plane). Such layer assignment indices were based upon the depth at which the photon started; a comparison of the photon z-

coordinate with the boundary depths revealing which layer a particular photon was in; c) a Boolean parameter was used to indicate whether the photon was currently in the cylinder or not.

4.4.4.2.1 Test performed when the photon was in a plane layer without a cylinder

This test, described below in section 4.4.4.2.4 was the most rapid to perform in terms of processing time. It was initiated when it was determined that the photon was in a layer not containing the cylinder. This was done by comparing the integer parameter indicating which layer the photon was in to the layer in which the cylinder resided. If the two parameters were not equal then the photon was in a layer not containing a cylinder.

4.4.4.2.2 Test performed when the photon was in a plane layer with a cylinder

If the photon was in the layer in which the simulated cylinder was placed, but was not actually in the cylinder itself, then two tests were performed to check if the photon crossed any boundaries. This was determined to be the case when the integer parameters describing the layer that the photon was currently in and the layer that the cylinder was in were equal. Firstly, a test was performed to see if the photon crossed the cylinder at any point on its periphery. This first test is described in detail below in section 4.4.4.2.5 as a separate section because the detail is somewhat lengthy, and because the method described therein is also pertinent to the following section. If the photon did not cross the boundary of the cylinder, the second test was performed to determine if the photon then crossed a plane boundary, following the method described in section 4.4.4.2.4. If it were the case that the photon's proposed trajectory crossed both a cylinder and a plane boundary, then the distance to the cylinder would always be less than that to the plane boundary ensuring that the photon hit the cylinder first; this was the reason for testing for a cylinder boundary crossing before testing for any plane boundary crossing that might have had occurred.

4.4.4.2.3 Test performed when the photon was in a cylinder

All photons initially began at positions outside the cylinder and just below the sample surface. A Boolean parameter, isPhotonInTheCylinder, initially set to be FALSE was used to indicate whether at any particular time during the simulation a photon was inside the cylinder or not. Subsequently during the simulation when a photon crossed a cylinder boundary this Boolean expression was toggled between TRUE and FALSE to reflect the photon's position with respect to the cylinder. If the photon began inside the cylinder, then the test for a cylinder boundary crossing was the only test that needed to be performed since the photon cannot begin inside the cylinder and cross a plane boundary without first leaving the cylinder itself. So, if isPhotonInTheCylinder was TRUE then the test of section 4.4.4.2.5 was performed in preference to those described in 4.4.4.2.1 and 4.4.4.2.2 above.

4.4.4.2.4 Test performed for detecting the crossing of a plane boundary

To test for the crossing of a plane boundary, the following procedure was adopted: photons began at a known point in the simulated sample and were thus in a known layer, if the photon wasn't in the layer in which the cylinder was to be found a test was performed to see if the photon's projected final point following the proposed trajectory was on the other side of the nearest plane boundary to be found in the direction in which the photon was heading. The sign of the z-direction cosine indicated whether the photon was moving down (a positive value of the direction cosine indicating that the photon was moving in the +z-direction of Figure 4.1) or up (a negative value of the z-direction cosine indicating that the photon was moving in the -z-direction of Figure 4.1).

4.4.4.2.5 Test performed for detecting the crossing of a cylinder boundary

Details of any crossing points found during this test were retained in memory for access by other functions or passed as parameters out of the function for access by the calling function. A Boolean indicator of whether the photon hit a cylinder boundary was also passed back to the calling function for use in the program's flow control.

In order to detect photons that crossed the embedded cylinder boundary, it was sufficient to apply the following mixed 2- and 3-dimensional analysis method. The photon trajectory was projected onto a cross-section from an x = arbitrary constant plane along with a cross-section of the cylinder, as illustrated in Figure 4.6 below. The vector forming the line joining the start point (point A) and projected end point (point B) was then found and a test performed to see if this vector intercepted the circle anywhere along its trajectory. If this was found to be the case, the x-y-z coordinates corresponding to the intercept point closest to the start position of the photon were calculated in 3-dimensions. The distance of this intercept point of the vector and the cylinder from the starting point of the photon was then compared to the pathlength over which the photon was projected to travel. If the distance to the cylinder was less than the projected path then the photon would hit the cylinder at the x-y-z point calculated previously provided that it were moving towards the cylinder. The following analysis shows how the intercepts were calculated:

Figure 4.6: Testing whether cylinder boundary crossed
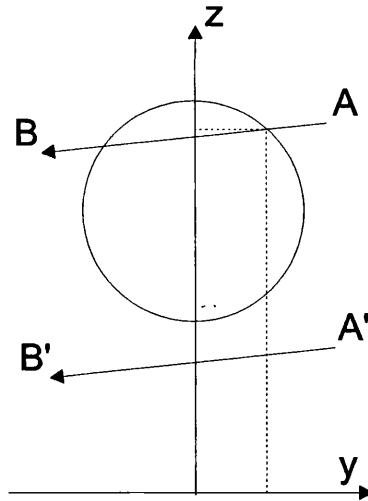
Let the coordinates of A = (x_1, y_1, z_1), and those of B = (x_2, y_2, z_2). If the centre of the circle above lay on the line ($y = 0$, $z = c'$), then in order to test if the line intercepted the circle we needed to solve the simultaneous equations,

$$y^2 + (z - c')^2 = r^2 \qquad (4.7)$$

$$z = my + c \qquad (4.8)$$

The first defined the circle in the x = constant plane, and the second the line passing through points A and B. The gradient and intercept of the line were, respectively,

$$m = \frac{y_2 - y_1}{z_2 - z_1} \quad \text{and} \quad c = z_1 - my_1$$

Substituting (4.8) into (4.7) and rearranging gave a quadratic equation (4.9) whose solution, if any, provided the intercept points of the line and circle.

$$y^2\left(1 + m^2\right) + 2m(c - c')y + \left((c - c')^2 - r^2\right) = 0 \qquad (4.9)$$

Solutions to 4.9 were given by the following equation,

$$y = \frac{-2m(c - c') \pm \sqrt{4m^2(c - c')^2 - 4\left(1 + m^2\right)\left((c - c')^2 - r^2\right)}}{2\left(1 + m^2\right)} \qquad (4.10)$$

Equation (4.10) was then used determine what relationship the line and circle had. If

$$4\left(1 + m^2\right)\left((c - c')^2 - r^2\right) = 4m^2(c - c')^2 \qquad (4.11)$$

then the line was a tangent to the circle, whereas if

$$4\left(1 + m^2\right)\left((c - c')^2 - r^2\right) > 4m^2(c - c')^2 \qquad (4.12)$$

then the line did not intersect the circle, and if

$$4\left(1 + m^2\right)\left((c - c')^2 - r^2\right) < 4m^2(c - c')^2 \qquad (4.13)$$

the line cut the circle and in two places. When the latter case was found to be true, the points at which the intercept occurred were checked to find if the photon really did cross, or if it was just headed for the cylinder some distance away, by comparing distances as previously mentioned. (The tangential case was ignored as it indicated a photon incident at 90° to a normal to the cylinder surface, and therefore implied 100% reflectance.)

4.4.4.3 Propagating the photon to the next position

The photon was propagated to a next position depending upon whether or not it had encountered any refractive index boundaries. The possible cases are described below in sections 4.4.4.3.1 to 4.4.4.3.3, but in all cases the new photon weight W_n was reduced from its previous value W_{n-1} according to the following equation to account for the absorption properties of the material in which the photon was propagating:

$$W_n = W_{n-1} \cdot e^{-\Delta x . \mu_a} \qquad (4.14)$$

where μ_a was the absorption coefficient corresponding to the material the photon was currently propagating in, selected from the values derived from the user-defined initialisation file, and Δx was a length measurement selected according to the cases given below. If this new value for the weight fell below a user-defined threshold, then the photon was terminated rather than propagated to the boundary, in preparation for the simulation of a new photon.

The model assumed constant absorption of light in any one material but as we were not interested in the deposited energy, since we assumed that no significant changes in the scattering properties of the material occurred with the intensities and wavelengths of light we considered, this absorption weight was discarded[#].

A running total was also kept, by incrementing the appropriate variables, of both the physical pathlength traversed by each photon and the total optical pathlength over which each had travelled. In the former case, all values of Δx were added to a double precision variable which was set to zero during the launch of each new photon. In the latter case, the value $\Delta x.n_i$ was added to a similar double precision variable to accumulate the optical pathlength. The value n_i being equal to the refractive index of the layer in which the photon was propagating.

_____

[#] In models that are interested in the deposition of energy within tissue, such as those interested in photo-coagulation for example, this absorption factor is important and would be stored in an array to add to the total distribution picture of energy within the tissue. From this the temperature changes in the tissue can be calculated and photo-coagulation modelled.

4.4.4.3.1 Photon did not hit a boundary

If the tests performed for checking for a boundary crossing, as described in the previous section, proved negative, then the photon was moved from the starting position to the projected position in accordance with equation 4.15 below. Further interactions in the simulated sample were then started from this point. The weight of the photon following the interaction W_n was reduced according to equation 4.14 above, to account for absorption of photon energy in the medium in which the photon was travelling, with a value of $\Delta x = r_n$. r_n being the full length of the interaction as given by the uninterrupted scattering length found according to equation 4.6 above. The pathlength and optical pathlength were incremented as described in 4.4.4.3 above using the value of $\Delta x = r_n$: the photon weight was also reduced using this value.

$$\begin{bmatrix} x_n \\ y_n \\ z_n \end{bmatrix} = \begin{bmatrix} x_{n-1} \\ y_{n-1} \\ z_{n-1} \end{bmatrix} + r_n \cdot \begin{bmatrix} du1 \\ du2 \\ du3 \end{bmatrix}$$

(4.15)

4.4.4.3.2 Photon hit a plane boundary

If the boundary crossing test indicated that the photon crossed a plane boundary then the photon was propagated to that interface. The z-coordinate was set to the boundary interface depth and the pathlength necessary to propagate the photon to the boundary l_{tb} (see Figure 4.7 below) was calculated by proportion as follows:

$$l_{tb} = r_n \cdot \frac{\left| z_{start} - z_{boundary} \right|}{\left| z_{projected} - z_{start} \right|}$$

(4.16)

Figure 4.7: Propagating a photon to a plane boundary
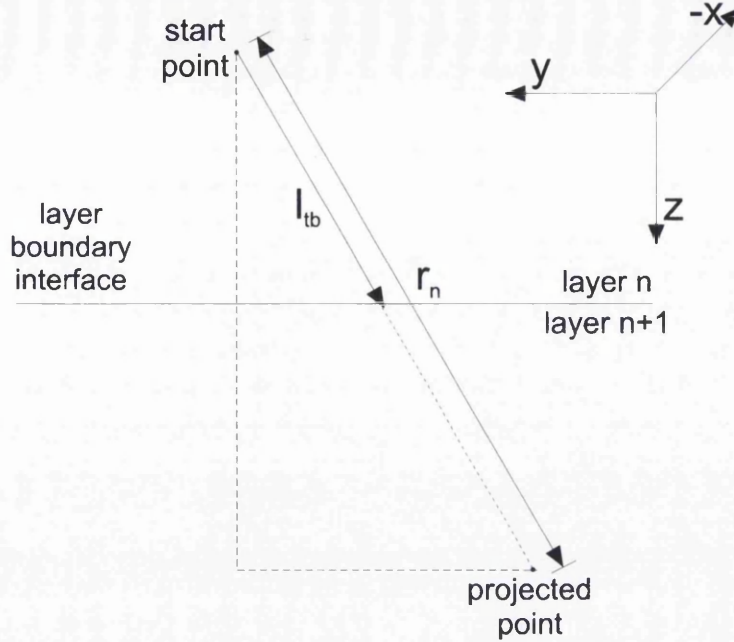
The x- and y- and z-coordinates were then found thus:

$$\begin{bmatrix} x_n \\ y_n \\ z_n \end{bmatrix} = \begin{bmatrix} x_{n-1} \\ y_{n-1} \\ z_{boundary} \end{bmatrix} + \begin{bmatrix} l_{tb}du1 \\ l_{tb}du2 \\ 0 \end{bmatrix}$$

(4.17)

placing the photon position on the plane of the boundary interface. The pathlength and optical pathlength were incremented by an amount l_{tb} and $l_{tb}.n_i$ respectively, and the weight reduced according to equation 4.14 by setting $\Delta x = l_{tb}$. The fate of the photon following this propagation was then decided by the rouletting procedure described in section 4.4.4.4 below.

4.4.4.3.3 Photon hitting a cylinder boundary

If the photon had hit a cylinder boundary, as indicated by the process outlined in section 4.4.4.2.5 above, the y- and z-coordinates of the intercept ($y_{intercept}$ and $z_{intercept}$) were calculated according to equations 4.10 and 4.8 respectively. The pathlength necessary to propagate the photon to the cylinder boundary could be calculated from either value. Using the z-value, the pathlength to the boundary l_{tc} was calculated as follows:

$$l_{tc} = \left| \frac{z_{intercept} - z_{n-1}}{du3} \right| \qquad (4.18)$$

The position of the photon once it had been propagated to the boundary was then:

$$\begin{bmatrix} x_n \\ y_n \\ z_n \end{bmatrix} = \begin{bmatrix} x_{n-1} \\ y_{intercept} \\ z_{intercept} \end{bmatrix} + \begin{bmatrix} l_{tc}du1 \\ 0 \\ 0 \end{bmatrix} \qquad (4.19)$$

The pathlength and optical pathlength were incremented by an amount l_{tc} and $l_{tc}.n_i$ respectively, and the weight reduced according to equation 4.14 by setting $\Delta x = l_{tc}$. As with all boundary interactions, the fate of the photon following the propagation was decided by the rouletting procedure described in section 4.4.4.4 below.

4.4.4.4 Rouletting at a boundary

Rouletting (step 33 of Figure 4.5) accounted for reflection and refraction of photons crossing mismatched refractive index boundaries. It was based upon the reflection coefficient $R(\Theta)$ for a photon striking the refractive index boundary at an angle of incidence Θ with respect to the normal to that surface. The values of $R(\Theta)$ for all possible boundaries had been calculated and placed in suitable look-up tables during the program's initialisation phase [see section 4.4.2]. The value $R(\Theta)$ gave a direct measure of the probability that a photon would be reflected, a fact which the rouletting technique used to select which photons were reflected and which transmitted.

The value Θ was found according to one of two methods depending upon whether the photon hit a plane boundary or a cylinder boundary. If the photon hit a plane boundary the value of Θ could be found directly from the z-direction cosine $du3$ as follows:

$$\Theta = \cos^{-1}(du3) \qquad (4.20)$$

The problem of finding the value Θ when the photon struck the cylinder surface was reduced to finding the angle between the normal to the cylinder $\mathbf{n}$ and the photon trajectory $\mathbf{p}$: this is shown in cross-section in Figure 4.8 below. The photon vector $\mathbf{p}$ is shown in the plane of the diagram, but in reality this was not necessarily the case.

The photon trajectory **p** was already known from its direction cosines. The equation of the normal to the cylinder **n** resided in the y-z plane, and was perpendicular to the tangent formed at the point where the photon was incident on the cylinder surface.

Figure 4.8: Propagating a photon to a cylinder boundary
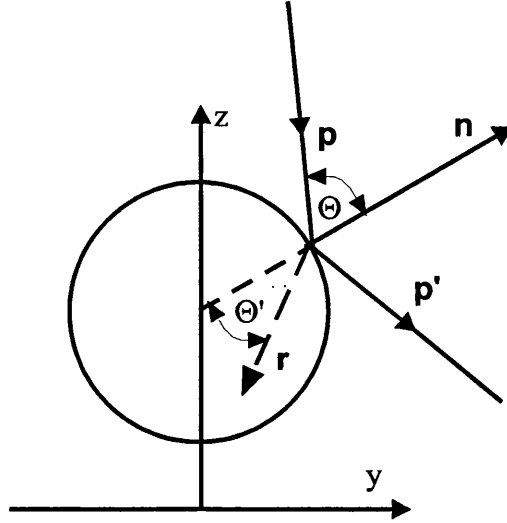
According to Smyrl[8] the following equation may be used to determine the angle, Θ, between two vectors:

$$\cos\Theta = l_p l_n + m_p m_n + n_p n_n \tag{4.21}$$

where l, m and n are the respective direction cosines of the two vectors. The direction cosines of **n** were found from the point at which the photon intercepted the cylinder, thus:

$$l_n = 0, \, m_n = \frac{y_n}{r}, \, n_n = \frac{z_n - c'}{r} \tag{4.22}$$

where r was the radius of the cylinder.

Substituting the values from equation 4.22 and the values $l_p = du1$, $m_p = du2$ and $n_p = du3$ into equation 4.21 enabled the value of Θ to be found and the value for $R(\Theta)$ to be looked up.

The following probability line shows how the value $R(\Theta)$ was then used to decide whether the photon was transmitted or reflected:

Figure 4.9: Rouletting at a boundary
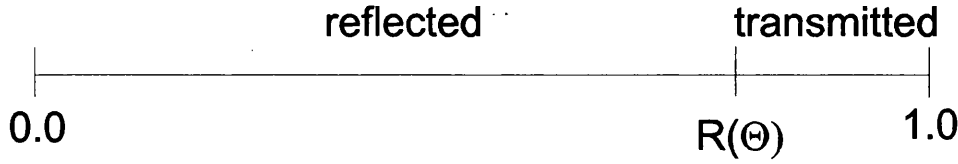
A random number (chosen from a uniform distribution), N_{rand}, between 0.0 and 1.0 was selected (or rouletted). If $0.0 \leq N_{rand} \leq R(\Theta)$ then the photon was deemed to have been reflected, and if $R(\Theta) < N_{rand} \leq 1.0$ then the photon was deemed to have been transmitted. Having determined the fate of the photon at the boundary, the photon was either reflected or refracted according to the appropriate method described in the following section.

4.4.4.5 Reflection or refraction of a photon at a boundary

Following rouletting, photons were either reflected back into the material from which they had come or refracted into a different material at the boundary of incidence. Four possible cases could occur and these are described in the following sub-paragraphs of this section.

4.4.4.5.1 Reflection from a plane boundary

When photons were reflected at a plane boundary the direction cosines were modified as follows to reflect the fact that only the sign of the z-direction cosine needed to be changed:

$$\begin{bmatrix} du1 \\ du2 \\ du3 \end{bmatrix} \rightarrow \begin{bmatrix} du1 \\ du2 \\ -du3 \end{bmatrix} \tag{4.23}$$

4.4.4.5.2 Refraction at a plane boundary

First, the integer index indicating which layer the photon was in was updated to reflect the fact that a boundary had been crossed.

Refraction at a plane boundary caused the angle that the photon trajectory incident upon the plane made with the normal to that plane Θ to be refracted to an angle Θ' according to Snell's law:

$$\frac{\sin\Theta}{\sin\Theta'} = \frac{n_2}{n_1} \qquad (4.24)$$

Therefore:

$$\sin\Theta' = \frac{n_1\sin\Theta}{n_2} \qquad (4.25)$$

Since $\Theta = \sin^{-1}(du3)$ the refracted z-direction cosine in the plane of incidence z' was given by:

$$z' = \cos\left[\sin^{-1}\left[\frac{n_1\sin\Theta}{n_2}\right]\right] \qquad (4.26)$$

The sign of z' was the same as that for the incident photon as it passed though the refractive index boundary in the same sense as it was incident. Normalising the direction cosines accounted for the change of $du3$ due to refraction and gave the following as the direction cosines for the refracted photon:

$$\begin{bmatrix} du1 \\ du2 \\ du3 \end{bmatrix} \rightarrow \begin{bmatrix} \dfrac{du1}{\sqrt{du1^2 + du2^2 + z'^2}} \\ \dfrac{du2}{\sqrt{du1^2 + du2^2 + z'^2}} \\ \dfrac{z'}{\sqrt{du1^2 + du2^2 + z'^2}} \end{bmatrix} \qquad (4.27)$$

4.4.4.5.3 Reflection from a cylinder boundary

We knew from the solution above at what point the photon struck the cylinder surface, and using this and the following vector equation we calculated the direction cosines of both the photon, $\mathbf{p} = (y_p, z_p)$, and the normal, $\mathbf{n} = (y_n, z_n)$, in the y-z plane. The angle between these two vector equations was given by the following vector

equation; this angle was also equal to the angle of reflection of the photon with respect to the normal to the cylinder surface:

$$\mathbf{n.p} = \cos\Theta \text{ or } \left(y_n\mathbf{j} + z_n\mathbf{k}\right)\bullet\left(y_p\mathbf{j} + z_p\mathbf{k}\right) = \cos\Theta \tag{4.28}$$

with $\mathbf{j}$ and $\mathbf{k}$ being unit vectors in the $+y$ and $+z$ directions respectively. For the reflected photon component:

$$\mathbf{n.p'} = \cos\Theta \text{ or } \left(y_n\mathbf{j} + z_n\mathbf{k}\right)\bullet\left(y_{p'}\mathbf{j} + z_{p'}\mathbf{k}\right) = \cos\Theta \tag{4.29}$$

Multiplying out the left hand side of the two preceding equations and subtracting the results yielded:

$$\left(y_p - y_{p'}\right)y_n + \left(z_p - z_{p'}\right)z_n = 0 \tag{4.30}$$

Moreover, we also know that the sum of the squares of any set of orthogonal basis direction cosines is unity, thus:

$$y_{p'}^2 + z_{p'}^2 = 1 \tag{4.31}$$

Having two equations in two unknowns, we solved to find the new y-direction cosines. After some considerable algebraic manipulation we obtained two solutions, thus:

$$y' = \frac{ac \pm \sqrt{a^2c^2 - \left(a^2 + b^2\right)\left(-b^2 + c^2\right)}}{a^2 + b^2} \tag{4.32}$$

where $a = y_n$, $b = z_n$, and $c = y_p y_n + z_p z_n$.

One of these solutions was the same as our starting direction $\mathbf{p}$, and the other was the solution we were seeking $\mathbf{p'}$. The elimination of the original solution thus left $\mathbf{p'}$. Knowing the reflected y-direction cosine y' we calculated the reflected z-direction cosine z' thus:

$$z' = \pm\sqrt{1 - y'^2} \tag{4.33}$$

Finally the signs of the reflected components were found by considering the direction of approach of the original photon trajectory, **p** before all the direction cosine components were normalised to account for the reflection in 3-dimensions thus:

$$
\begin{bmatrix} du1 \\ du2 \\ du3 \end{bmatrix} \rightarrow \begin{bmatrix} \dfrac{du1}{\sqrt{du1^2 + y'^2 + z'^2}} \\[3mm] \dfrac{\pm y'}{\sqrt{du1^2 + y'^2 + z'^2}} \\[3mm] \dfrac{\pm z'}{\sqrt{du1^2 + y'^2 + z'^2}} \end{bmatrix}
\tag{4.34}
$$

4.4.4.5.4 Refraction at a cylinder boundary

Refraction was performed by considering the incident angle the photon vector **p** made with the plane tangential to the cylinder surface described by the normal vector **n** to it in the y-z plane. The refracted direction cosines of the photon in the y-z plane were given by $\mathbf{r} = (y_r, z_r)$.

When the incident angle was Θ, then the refracted angle Θ' could be derived from Snell's law (equation 4.24 above) for media having refractive indices n_1 and n_2 respectively. Using the fact that $\sin\Theta = \sqrt{1 - \cos^2\Theta}$ we could deduce using Snell's law that the cosine of the refracted angle $\cos\Theta' = \sqrt{1 - \dfrac{n_1}{n_2}\sin^2\Theta}$. Knowing that the cosine of the angle between the two vectors was **n.p**, we further deduced that:

$$
y_r y_n + z_r z_n = \sqrt{1 - \frac{n_1}{n_2}\left(1 - \cos^2\Theta\right)}
\tag{4.35}
$$

Moreover $y_r^2 + z_r^2 = 1$, which once rearranged and substituted into 4.35, gave the following:

$$
y_r y_n + z_n\sqrt{1 - y_r^2} - \sqrt{1 - \frac{n_1}{n_2}\left(1 - \cos^2\Theta\right)} = 0
\tag{4.36}
$$

Some manipulation yielded the following solutions for y_r:

$$y_r = \frac{-ac \pm \sqrt{a^2c^2 - (a^2 + b^2)(-b^2 + c^2)}}{a^2 + b^2} \qquad (4.37)$$

where $a = y_n, b = z_n$ and $c = \sqrt{1 - \frac{n_1}{n_2}(1 - \cos^2 \Theta)}$. The values of z_r were derived from

the equation $y_r^2 + z_r^2 = 1$, but only one of the pairs of values (y_r, z_r) gave a physically

realistic solution for which the angle of refraction Θ' was within 90° of the angle of

incidence, and this was the solution adopted following refraction.

We knew the magnitude of the direction cosines of the refracted component **r** and

found the respective signs by making them equal to the incident sign of the direction

cosines of the vector **p**. As was necessary when processing reflections from the

cylinder, the direction cosines of the refracted beam were also normalised to move

the trajectory into 3-dimensions. The final refracted direction cosines following

refraction at a cylinder boundary were:

$$\begin{bmatrix} du1 \\ du2 \\ du3 \end{bmatrix} \rightarrow \begin{bmatrix} \dfrac{du1}{\sqrt{du1^2 + y_r^2 + z_r^2}} \\ \dfrac{\pm y_r}{\sqrt{du1^2 + y_r^2 + z_r^2}} \\ \dfrac{\pm z_r}{\sqrt{du1^2 + y_r^2 + z_r^2}} \end{bmatrix} \qquad (4.38)$$

Finally the Boolean parameter indicating whether the photon was in the cylinder or

not was toggled to account for the crossing of the cylinder boundary.

4.4.4.6 Calculating a new scattering direction

Having decided upon the fate of the photons, the new scattering direction of those

allowed to continue was calculated. This involved using random numbers to generate

new values for Ω and Ψ [see Figure 4.4 above]. A first random number N_{ran} was used

to find a new value for the deflection angle ω (from the previous direction of travel)

by selection from a 1000 point look-up table of the scattering phase function of the

material in which the photon was travelling created using the Henyey-Greenstein

function for the g-factors found during the program initialisation [see section 4.4.2 above]. The angle ω was indexed by multiplying the value N_{ran} by 1000 and taking the index as being the closest integer to the resultant value: the value of ω being found as the data value at the indexed point in the array. The azimuth angle ψ was assumed to have a constant probability density function[2] and so could be calculated directly from a second random number N_{ran} as: $\psi = 2\pi N_{ran}$.

Finally the absolute direction of the photon relative to the tissue co-ordinate system, shown in Figure 4.4 in the (x,y,z) axis system, was calculated. The new absolute direction cosines following the random scattering event were given by:

$$\begin{bmatrix} du1 \\ du2 \\ du3 \end{bmatrix} = \begin{bmatrix} \cos\Psi\cos\Omega & -\sin\Psi & \sin\Omega\cos\Psi \\ \sin\Psi\cos\Omega & \cos\Psi & \sin\Omega\sin\Psi \\ -\sin\Omega & 0 & \cos\Omega \end{bmatrix} \begin{bmatrix} \sin\omega\cos\psi \\ \sin\omega\sin\psi \\ \cos\omega \end{bmatrix} \tag{4.39}$$

4.5 Validation of Monte Carlo simulation data

In order to verify the data created by the Monte Carlo simulation, the initialisation parameters were set such that the top layer of the model was greater than 20 mm thick and did not contain an embedded cylinder. As the cut-off depth for the simulation was 20 mm this ensured that a homogeneous slab of material was simulated[*] . The optical parameters for this slab were set as follows: refractive index = 1.4, μ_s = 20.0 mm^{-1}, μ_a = 0.04 mm^{-1} and g = 0.9.

Since the simulated slab was homogenous it was possible to compare the distribution of light intensity at the surface of the simulated slab to that derived using the theoretical model of Eason *et al*[9] using Green's functions. Such a model had been coded using Mathematica by S. Arridge at UCL, and this was used to produce the data set against which the Monte Carlo data was compared.

The results of this comparison are shown below in Figure 4.10, and indicated a good match between our simulation data and the theoretical model over a distance on the

---

[*] Models for 2 and 3 layered slabs do exist, but we made no data comparisons to such models.

surface of the sample over a distance of approximately 10 mm, after which the data sets began to diverge. Such a divergence was known to occur between such data sets at increasing radial distance, and was due to the fact that the refractive index mismatch at the surface was not accounted for by the theoretical model, thereby leading to a higher intensity than that found for the Monte Carlo model in which partial surface reflection reduced the overall surface intensity by reflecting light back into the sample from the mis-matched boundary.

For a layered sample containing refractive index boundaries between the layers and an embedded cylinder, the crossing events were checked manually by stepping though the program in debug mode and comparing the effect upon the photon direction and weight, in the event of reflection or refraction, to values calculated manually from Snell's and Fresnel's laws using pen and paper. This approach confirmed that the photons were indeed following the paths predicted by the laws of physics.

The results of the data comparison below and the analytical checking of boundary events gave us some confidence that the Monte Carlo simulation used to produce the data during the simulation of a layered tissue sample was producing plausible and reliable data.

Figure 4.10: Comparison of Monte Carlo simulated and theoretical surface intensities[9]
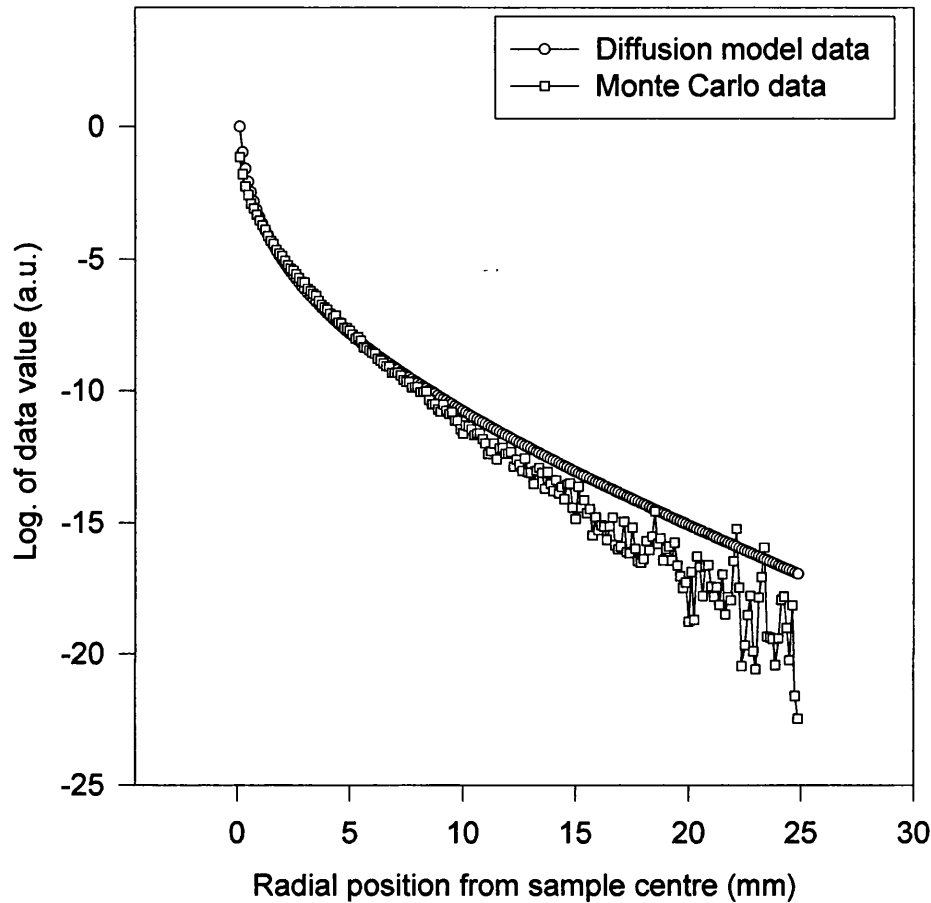
Chapter References

[1] P. van der Zee, Measurement and modelling of the optical properties of human tissue in the near infrared, (PhD thesis, University of London, 1992)

[2] M. Essenpreis, Thermally induced changes in optical properties of biological tissues, (PhD thesis, University College London, 1992)

[3] D. R. Kirkby, Monte Carlo simulation of laser Doppler blood flow measurement through thick tissue sections, (MSc. report, University College London, 1993)

[4] M. H. Eddowes, T. N. Mills and D. T. Delpy, "Monte Carlo simulations of coherent backscatter for identification of the optical coefficients of biological tissue *in vivo*," *Appl. Opt.*, Vol. 34, No. 13, pp. 2261-2267, 1995

[5] C. F. Bohren and D. R. Huffman, *Absorption and scattering of light by small particles*, (Wiley-Interscience, New York, 1983)

[6] H. C. van de Hulst, *Light scattering by small particles*, (Dover publications, New York, 1981)

[7] W. H. Press, S. A. Teukolsky, W. T. Vetterling and B. P. Flannery, *Numerical Recipes in C: The Art of Scientific Computing*, (Cambridge University Press, Cambridge, 1993)

[8] J. L. Smryl, An introduction to University mathematics (Hodder and Stoughton, London, 1986)

[9] G. Eason, A. R. Veitch, R. M. Nisbet and F. W. Turnbull, "The theory of the back-scattering of light by blood," *J. Phys. D: Appl. Phys.*, Vol. 11, pp. 1463-1481, 1978

The Monte Carlo Analysis Tools and Utilities

5.1 Chapter overview

This chapter details the way that the main Monte Carlo analysis tool worked. The chapter begins by describing the program that was used to analyse the data files produced by the simulation program described in the previous chapter, initially in general terms, in section 5.2, and then in some detail in section 5.3. The end of the chapter mentions briefly (section 5.4) some utility programs that were developed for use alongside the analysis tool: these are of less relevance to the overall content of this thesis, but were found to be useful and so are included briefly for interest.

5.2 General description of the Monte Carlo analysis tool program

The analysis program calculated the heterodyne to non-heterodyne signal ratio (HNHR) for a particular user-defined detector geometry which collected light output from the surface of the sample (Figure 4.1). Data from the Monte Carlo simulations was used to provide the non-heterodyne component for the calculation of HNHR and to analyse the "false heterodyne" signal (see section 5.3.4.3.1 below for an explanation of this term), the heterodyne component was added analytically by the analysis program. The user defined parameters were recorded as initialisation parameters in a series of text files which the program read according to the order dictated by a batch file. This facilitated the consecutive processing of multiple detector geometries for various input beam geometries.

The analysis of simulation data fell into several parts. Each initialisation file referred to in the batch file initialised a set of detector parameters, the associated surface area of which was then scanned across the sample surface between user-defined limits given in that initialisation file. Once the calculation of HNHR for each detector geometry associated with each initialisation file was finished for each radially scanned centre position of the detector (see following paragraph), the next initialisation file was read to set up the detector geometry ready to perform the next radial scan. This process continued until all the detector geometries referred to in the batch file had been scanned across the sample surface. The processing of each of

these geometries produced a single associated data file giving the HNHR measured as a function of the centre point of the detector area as it was scanned along the y-axis.

5.3 Detailed description of the Monte Carlo analysis tool code

We adopt a similar approach in this chapter when describing the detailed workings of the Monte Carlo analysis tool to that we adopted in the last chapter for describing the simulation program itself, in that we refer extensively to flowcharts derived from the actual program code (see Figure 5.1 below).

5.3.1 Initialisation

The first task of the analysis program was to ascertain, at step 1, how many individual batch initialisation files were to be processed. The text file "batch.ini" was expected by the program to reside in the same directory as the executable analysis file code and to contain a list of initialisation files, each of which initialised a radial detector scan on the sample surface for given user defined detector starting parameters: the centre point of the detector area being stepped across the sample surface a point at a time.

Figure 5.1: Main flow of control in the Monte Carlo data analysis program
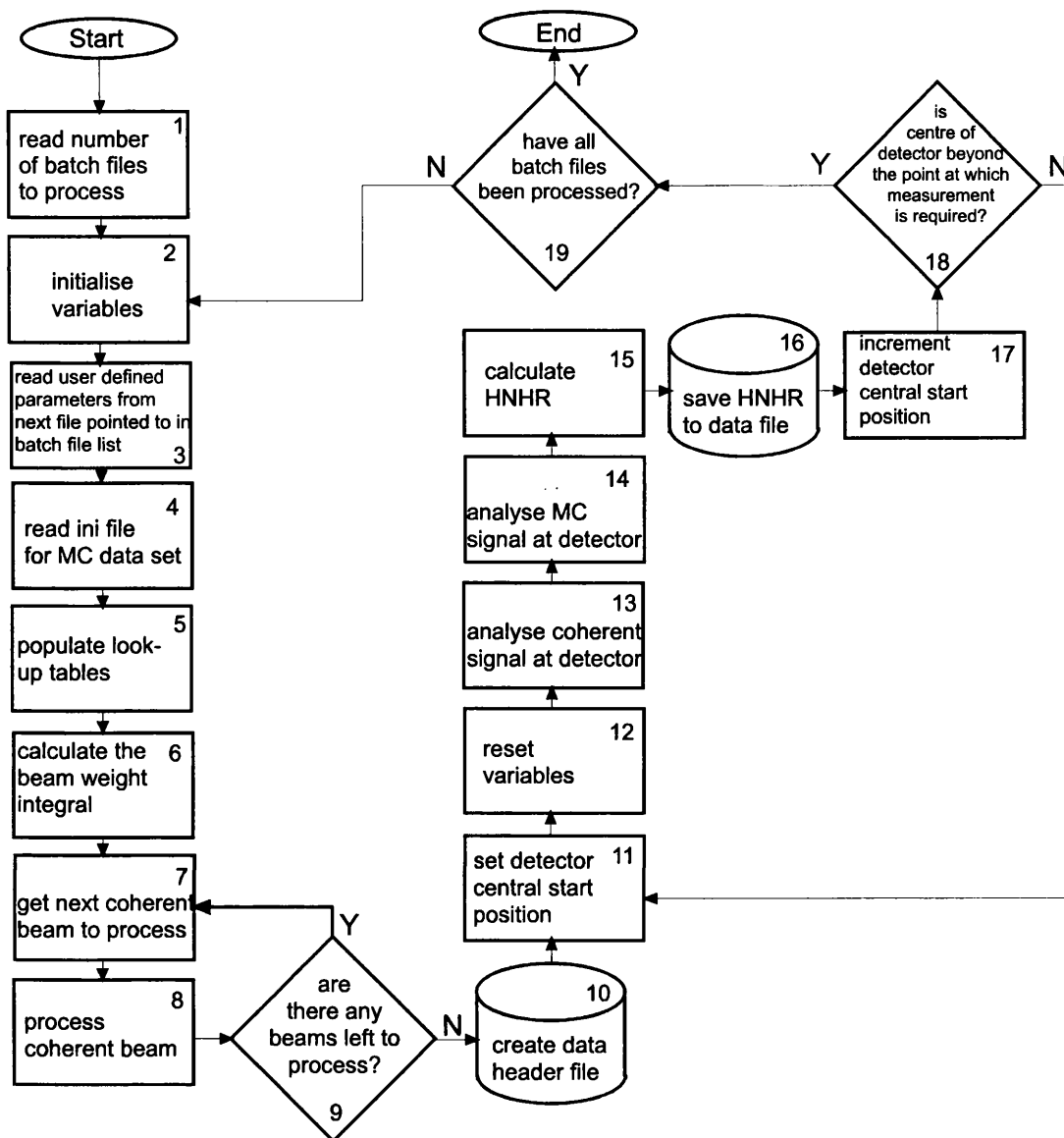
Each radial scan required the following parameters to be given for each of the initialisation files in the batch list: the angle the central axis of the detector cone formed at the surface of the sample made with the normal to the sample surface (referred to hereinafter as the detector angle); the cone angle formed at the surface of the sample within which emitted or reflected photons would be deemed to have fallen upon the detector's active area (referred to hereinafter as the acceptance angle); the starting point on the sample surface from which the centre of the detector area formed upon the sample surface was scanned radially in the y-direction; the end point on the sample surface which when reached by the radially scanned centre of the

detector area, would end the radial scanning process; the number of incremental steps by which the radially scanned detector area would be moved in between the extremities of the scanning process defined by the starting and end points; the optical path length at which the signal-to-noise ratio was to be set; the optical coherence length of the optical source that was used; the path to the directory in which the Monte Carlo data files generated by the simulation of Chapter 4 were found; the number of such Monte Carlo data files; the diameter of the detector area formed upon the surface of the sample and the name of the initialisation file used by the simulation process of Chapter 4 to generate the Monte Carlo data. This latter information was used to enable the analysis tool to extract the physical parameters used by the Monte Carlo simulation for the layer and cylinder physical and optical properties without having to enter them all again into the analysis files' initialisation records, and thereby to enable the correct addition of the heterodyne element of the HNHR to be traced analytically.

Having counted the number of batch files to process, the main iterative loop was begun. An initialisation process (steps 2 to 6) was begun for the set of detector parameters defined by the next initialisation file listed in the batch file. This process needed to be performed once per given detector arrangement.

The initialisation of variables in step 2 reset parameters used during the processes of coherent beam tracing and the calculation of the HNHR, to zero. This included variables such as resetting a counter for tracking any multiple beam spawned by the coherent beam tracing process (see section 5.3.3), and the resetting of accumulator variables used to sum the heterodyne, non-heterodyne and "false heterodyne" components of light reaching the detector active area.

At step 3 the program initialised the individual user-defined parameters (detector angle, acceptance angle, starting position, end position, number of incremental steps, coherent optical path length, source optical coherence length, data directory, number of data files, detector diameter and the Monte Carlo initialisation parameter file name) by reading the batch file indicated as being the next to process in the list, and storing the values into variables.

Using an analogous process to that described in section 4.2.2 for the Monte Carlo simulation itself, the refractive index mis-matches between the boundaries were themselves used to calculate Fresnel reflection coefficients to populate look-up tables which gave the reflection coefficient as a function of angle for photons or beams that were incident at those boundaries.

5.3.2 Calculating the integral of surface beam weight

Figure 5.2 below shows how the surface beam was analysed for a Monte Carlo simulation in which a Gaussian surface beam profile was incident at an angle $\theta \neq 0^{\circ}$. This figure illustrates the principles involved in calculating the beam weight integral and tracing the individual coherent beams used to approximate the input beam profile (see section 5.3.3 below).

It should also be noted, in Figure 5.2, that the centre of the incident beam was positioned such that the central ray hits the upper most point on the blood vessel. This point is that at which the maximum intensity of coherent light is expected to return from the blood vessel, the path being the minimum distance for the beam to have travelled in the tissue whilst also having sampled the blood vessel surface. This position was therefore expected to give the maximum HNHR for an incident beam that was Gaussian in profile: the central point of the beam being the most intense.

Indeed, this was always the case for the Monte Carlo simulations themselves, the input beam being fixed on the sample surface for a particular value of θ. The central position itself, where the ray incident at angle θ on the surface hit the top of the cylinder was found using one of the utility tools described briefly in section 5.4 below.

Figure 5.2: Quantising the surface input beam profile
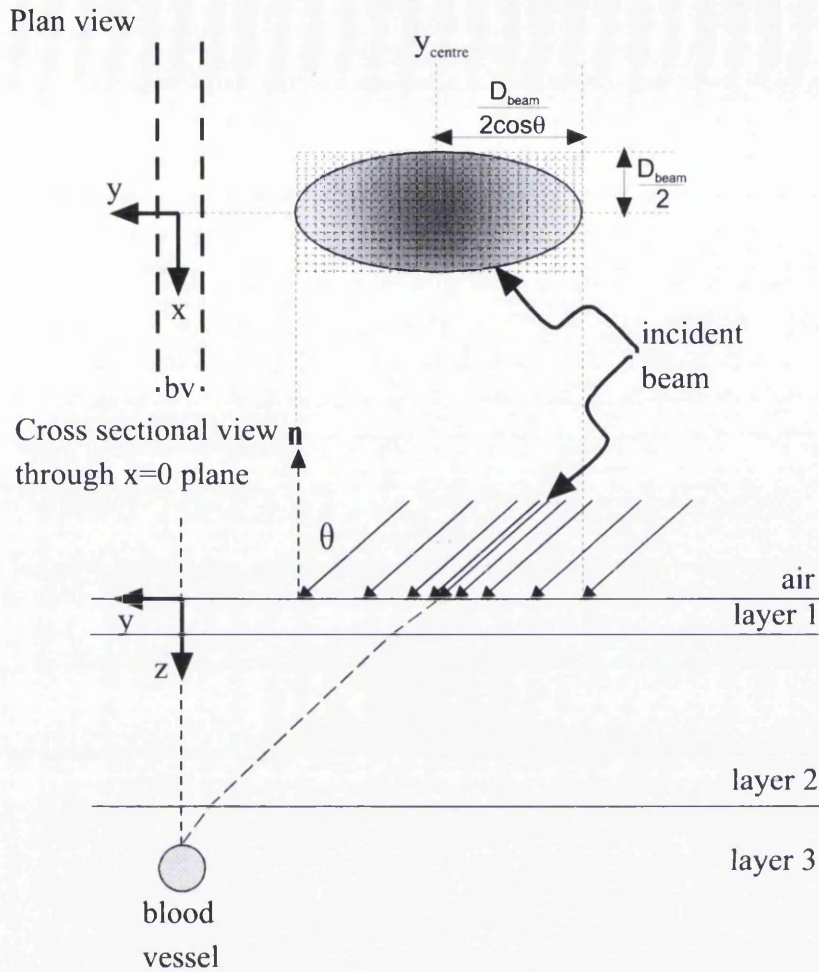
The surface input beam was incident over an area in the $z = 0$ plane whose shape was circular and symmetrical about the y-axis when incident at an angle parallel to the normal to the surface ($\theta = 0^\circ$ in Figure 5.2), and elliptical and symmetrical about the y-axis for non-normally incident surface input beams ($\theta \neq 0^\circ$ in Figure 5.2). In order to match the energy of the input beam to the energy of the simulated beam of photons, so that both the analytical incident beam and the Monte Carlo simulation injected the same number of photons into the sample, it was necessary to calculate the sum of all the surface beam weights (the beam weight integral of step 6) and assign a weight to each individual beam according to its fractional energy of the total input into the sample.

The beam weight integral varied according to the beam profile. Its value summed the initial coefficients chosen to be equal to the beam starting weight of all the individual

beams propagated into the sample. An intermediate value was used to calculate the actual beam starting weight and the use to which it was put is shown below when discussing step 7. Here we illustrate the method of calculating the beam weight integral I_{bw} for the case of point, top-hat and Gaussian input beams.

The point beam input profile was the simplest being:

$$I_{bw} = 1 \tag{5.1}$$

For a top-hat profile the beam weight integral was:

$$I_{bw} = \sum_{y_1}^{y_2} \sum_{-D_{beam}/2}^{D_{beam}/2} w_{xy} \, dxdy \tag{5.2}$$

where the sum was performed in 2-dimensions across the rectangular grid (shown in Figure 5.2) overlapping the incident beam surface profile, where $w_{xy} = 1$ when the pixel indexed at surface point (x,y) of that grid fell within the bounds of the profile, and where $w_{xy} = 0$ when the pixel fell outside the profile perimeter. A running total of how many of such pixels fell within the area defined by the surface profile, $N_{elements}$, was maintained. The two dimensional summation of equation 5.2 was performed across all the elements of the grid by summing the pixel values over a strip in the x-direction for each constant y-value. The major axis length l_{maj} was calculated as follows for a surface input beam incident at an angle θ with respect to the normal to the $z = 0$ plane:

$$l_{maj} = \frac{D_{beam}}{2\cos\theta} \tag{5.3}$$

The pixel size $P_{size} = dx = dy$ (in both x- and y- directions their being square) was determined from the user defined value for the number of steps N_{steps} to perform, read during initialisation as per section 5.3.1 above, according to the following equation:

$$P_{size} = \frac{D_{beam}}{2N_{steps}} \tag{5.4}$$

97

The limits of the scan in the x-direction were thus made between the values

$$x = \pm \frac{D_{beam}}{2},$$

and in the y-direction: $y_1 = y_{centre} - l_{maj}$ and $y_2 = y_{centre} + l_{maj}$.

For a Gaussian beam profile the beam weight integral was again calculated by considering individual beams propagated from a surface area broken down into square pixels: a single beam propagating in each of the pixel areas. The size of these pixels was the same as that for the top-hat profile above, i.e. $P_{size} \times P_{size}$. In this case we had to consider the radial fall in beam weight as a function of the radial distance from the central input beam point. We also allowed the surface area considered to extend to radial distances from the central input beam point beyond the $\frac{1}{e}$ width defined by the user in the initialisation parameter file. This accounted for the skirt-like asymptotic reduction of beam intensity seen for Gaussian profiles. Hence we integrated over a larger area when calculating the beam weight integral for the case of a Gaussian input profile than for a top-hat profile of diameter equal to the $\frac{1}{e}$ diameter of that Gaussian beam profile.

The beam weight integral I_{bw} for a 2-dimensional Gaussian surface intensity profile was:

$$I_{bw} = \sum_{y_1}^{y_2} \sum_{-2.5 D_{beam}/2}^{2.5 D_{beam}/2} w_{xy} g(x,y)\, dx dy \qquad (5.5)$$

where the function $g(x,y)$ defined the intensity profile for a Gaussian beam in 2-dimensions[1] and, as for the top-hat profile, $w_{xy} = 1$ when the pixel indexed at surface point (x,y) of the grid fell within the surface profile area, and where $w_{xy} = 0$ when the pixel fell outside of this area.

We scanned radially in the x-direction from $x = \pm 2.5 \frac{D_{beam}}{2}$, stepping from $y_1 = y_{start} - 2.5 l_{maj}$ to $y_2 = y_{start} + 2.5 l_{maj}$ in between performing the radial x-direction scans. The total surface integral weight for a Gaussian beam thus defined was

99.99% (±2.5 standard deviations) of that defined when the upper and lower x- and y-limits were ±∞ respectively.

5.3.3 Tracing coherent input beams

Once the program had been initialised and the beam weight integral calculated, the coherent signal component was added analytically by tracing beams incident in each of the pixels falling within the surface input beam area. For each of these beams the surface positions, directions, optical path lengths and weights of any surface reflections were stored in a memory array. Each beam was then traced through the sample, recording any split beams due to encounters with refractive index boundaries along the way. All beams and split beams were then traced until their weight fell below a predetermined threshold, their optical pathlength exceeded a user-defined maximum value, they reached the sample surface or until they had no prospect of ever reaching the surface again (such as when they were in layer 2 of Figure 4.1 and were heading downwards and in a direction away from the blood vessel). Any beams which re-emerged from the surface had their surface positions, directions, optical path lengths and weights recorded in a coherent surface beam array for later processing in conjunction with the Monte Carlo data (see section 5.3.4 below).

Thanks to the symmetry of the simulated sample with respect to the x-direction, the calculation of the coherent beam path for individual beams selected from the same pixel strip lying along the x-axis (having a fixed y-value) was greatly simplified. All such beams would follow identical paths with identical boundary interactions, the only difference was the relative weights of the beams for the case that the input beam profile was Gaussian in profile: therefore for the strips mentioned, all beams could be calculated by populating an array with identical values as those found for $x = 0$ and multiplying the weights in that array entry by a factor reflecting the percentage decrease in intensity for a Gaussian profile from the central point depending upon the radial distance of the point in question from the central point (i.e. depending upon its x-value). In the case of a top-hat profile the individual beam parameters were all identical at each point over such a strip in every respect except their final emergent x-coordinate.

The process described in the preceding two paragraphs was coded by the method of steps 7 to 9 in Figure 5.1.

At step 7 the program started by selecting a beam at the point $(0,y_1,0)$ on the surface of the sample. The beam was weighted according to whether it formed part of a top-hat profile or a Gaussian profile. If it were from a top-hat profile where all beam starting weights were equal the weight, $w(0,y_1,0)$ was found thus:

$$w(0,y_1,0) = \frac{I_{bw}.w_{tsp}}{N_{elements}} \tag{5.6}$$

where the weight w_{tsp} was that equivalent to the total weight of all the photons simulated by the Monte Carlo simulation. Numerically it was equal to the number of photons that were traced through the sample: each photon having an incident weight of unity.

If the profile was Gaussian the starting weight $w(0,y_1,0)$ was found thus:

$$w(0,y_1,0) = g(0,y_1,0)\frac{w_{tsp}}{I_{bw}} \tag{5.7}$$

The optical path length of this beam was then set according to the method described with reference to Figure 4.3 of the last chapter.

The surface reflected component of this beam was then calculated at the $z = 0$ plane and stored in the coherent beam array. The beams lying within the detector area on the surface of the simulated sample and also on a strip defined by the line $(x,y_1,0)$ then had their surface reflections processed by stepping the point of incidence from the surface pixel at $(x = 0, y = y_1, z = 0)$ to the next, a distance of P_{size} away at $(x = P_{size}, y = y_1, z = 0)$ etc. Each beam propagated at point $(x = n.P_{size}, y = y_1, z = 0)$, where n is an integer, had a symmetrical counterpart at the point $(x = -n.P_{size}, y = y_1, z = 0)$, and this too was processed and stored in the coherent beam array. For Gaussian beams the weight of the beams before surface reflection was calculated according to the surface profile function $g(x, y, 0)$, whereas for a top-hat profile the weight remained the same as for that at point $(x = 0, y = y_1, z = 0)$.

The beam at point ($x = 0$, $y = y_1$, $z = 0$) was then refracted into the sample and propagated. This process followed the same principles as those used in the last chapter with the exceptions that beams were made to split at boundaries rather than being rouletted, and the beams were reduced in weight from an initial weight of w_{n-1} to a weight of w_n according to the following equation rather than undergoing any random scattering events:

$$w_n = w_{n-1}e^{-\Delta x \mu_a \mu_s}$$
(5.8)

where Δx was the distance the beam travelled before undergoing an interaction with a refractive index boundary.

At each point where a beam crossed a boundary a reflected beam was created and saved into a temporary array. The reflected component's direction cosines and Fresnel-based weight reduction were calculated in the same way as for photons crossing boundaries in the Monte Carlo simulation itself: *viz.* according to the methods described in sections 4.4.4.5.1 and 4.4.4.5.3. The refracted component's parameters, if such a component existed, had its direction cosines and Fresnel-based weight reduction calculated according to the method described in sections 4.4.4.5.2 and 4.4.4.5.4. The refracted beam, or the totally internally reflected beam if there was no refracted beam, was then propagated until termination according to the criteria laid out in the introductory paragraph of this section.

Each beam in the temporary array was counted, and once a transmitted beam or internally reflected beam had been propagated to a point where it was terminated, a beam from the temporary array was propagated instead and the array counter decremented. Finally, once all the temporary beams had been processed to termination, the next beam was input into the sample at its surface, and the process of propagation and reflected beam storage began again.

Any beams that did leave the sample surface (at a point (0, y_{exit}, 0)) were refracted through the boundary between layer 1 and the surrounding air layer; a reflected beam was created and stored for further processing in the manner already described. A strip of pixels, centred on the line defined by $y = y_{exit} : z = 0$, was then processed with a beam at each pixel being added to the surface output array. The strip was of a length

corresponding to the width of the incident beam at the point on the surface of the sample where it was originally incident, and was at the same fixed y-coordinate, y_{exit}, as the emergent beam. The weight of the beams in the individual pixels was also reduced according to a surface Gaussian profile for an incident Gaussian beam, or remained constant for a top-hat profile.

Once all the beams lying on the y-axis of the surface input beam profile had been processed we were left with a surface output beam array populated with those beams reaching the surface of the sample which were described by their associated optical path lengths, weights, surface output coordinates and direction cosines. Other information, such as whether the beams had sampled the cylinder, was also recorded. This information was then used to determine the heterodyne signal component of the HNHR according to the method described in section 5.3.4.3 below.

5.3.4 Scanning the detector across the sample surface to calculate the HNHR

This part of the Monte Carlo analysis tool was used to determine how the HNHR for a particular user-defined detector geometry varied as that detector was scanned across the sample surface. Such a surface scan is shown schematically in Figure 4.1 as "output scan". The user was thus able to vary the parameters of the detector to see how these affected the measured HNHR for any particular Monte Carlo data set.

The user could define the following parameters relating to the detector area: the principal angle of the axis of the detector γ (generally γ was made to be equal to θ - *i.e.* confocal detection - in our analyses) defined with respect to a normal to the surface; the angle of acceptance defining an angular deviation range $\pm\Delta\gamma$ (measured from the principal detector angle) within which photons were deemed to have been incident upon the active detector area; the starting position for the central point of the detector area (on the line $(0, y, 0)$) at which the scan was to begin; the end point for the central detector position at which the scan was to stop; the number of steps between the starting and end positions of the scan (normally set to be 200); the coherent optical path length at which photons reaching the detector were deemed to give rise to a heterodyne signal by interacting with a reference beam l_{ref}; a source optical coherence length l_{source}; the root name of the Monte Carlo data set to be

analysed; the number of data files to be analysed, the detector diameter and the file name of the Monte Carlo initialisation file.

Some of these parameters are mentioned in section 5.3.1 above. The source optical coherence pathlength was variable but in general was set to be 0.078 mm, to correspond to an in-air source of coherence length 0.050 mm when propagating through material of refractive index 1.4. This latter refractive index corresponding roughly to that of dermis/epidermis in the near-infrared. The detector diameter defined a cut-off area outside of which no photons were deemed to reach the detector, it was thus unlike the beam input profile which allowed for "skirts" when the incident beam profile was Gaussian, and essentially simulated a pin-hole stop placed before the detector, or a detector of finite diameter.

Although it was not necessarily the case, as the coherent optical pathlength was variable, in all our data analysis we set the coherent optical pathlength to be equal to a value which corresponded to the optical path length that the central beam of the input illumination beam needed to follow in order to sample the uppermost point of the embedded cylinder. This value defined the central value of a range of optical pathlengths, the width of that range being defined by the source optical coherence length, within which photons reaching the detector were deemed to add to the heterodyne component of the HNHR. This information was made available by use of one of the utility tools described briefly in section 5.4. Setting the coherent optical pathlength to equate to that of the uppermost point of the cylinder in this manner gave rise to the greatest measure of HNHR since the coherent beam reflected from this point travelled the minimum possible path in the sample needed to sample the cylinder and was therefore attenuated the least.

The content of this section relates to steps 10 to 19 in Figure 5.1, although steps 13 to 16 are described in more detail under their respective subheadings (5.3.4.1 to 5.3.4.3) below. At step 10 a header was saved to a disk file detailing the detector parameters for future reference as well as setting up tab delimited column headings for each of the central detector position and the component parts making up the SNR as well as the SNR itself. At steps 11 and 12 the central detector position was set and the variables for totalling the optical components reset to zero.

5.3.4.1 Analysing the heterodyne signal measured at the detector

At this point in the analysis program, step 13, all the coherent beams found to have reached the surface of the sample (calculated according to the method of section 5.3.3) were analysed to see if any of them fell within the range of positions and exit angles defined according to the user-defined parameters. Such beams were saved in the coherent output beam array.

The test to see if any of these coherent beams reached the detector was performed according to the method described in the rest of this section. Each beam in the array, assigned exit coordinates on the sample surface of (x_{exit}, y_{exit}, 0), was tested individually in turn as follows: firstly, the extreme positions (y_3, y_4) of the detector area lying on the y-axis were found from the central point y-coordinate, y_{centre}, the detector tilt angle γ and the diameter of the detector area D_{det} thus:

$$y_3 = y_{centre} + \frac{D_{det}}{2\cos\gamma}, y_4 = y_{centre} - \frac{D_{det}}{2\cos\gamma} \tag{5.9}$$

If the surface y-coordinate (y_{exit}) of the coherent beam under test did not fall within these limits then the next beam in the array was tested. If it did fall within these limits, the limits of the detector in the x-direction (x_3, x_4) corresponding to the x-coordinate (x_{exit}) of the exit position were checked to see if the exit position lay within the detector area. In practice, since the detector area was symmetrical about the y-axis, $x_3 = -x_4$ and vice-versa. The value x_3 was found, after some manipulation and by knowing the equation for an ellipse, as follows:

$$|x_3| = \left[\frac{D_{det}^2}{4\cos^2\gamma} - \frac{|y_{centre} - y_{exit}|^2}{\cos^2\gamma} \right]^{\frac{1}{2}} \tag{5.10}$$

If $|x_{exit}| \leq |x_3|$ then the beam fell within the area defined by the detector and the further following angular acceptance test was performed to determine whether the beam would reach the active area of the detector and contribute to the HNHR.

Each beam left the surface with direction cosines (du_x, du_y, du_z). Since the coherent beams of the array had no x-component, i.e. $du_x = 0$, for their exiting direction cosines, the test for determining whether or not they fell within the acceptance angle of the detector was straight forward. The sign of the y-component du_y was extracted into the value $S_{duy} = \pm 1$. The beams were then tested to see if their output angle with respect to the z-axis, $\cos(du_z)$, fell within the detector acceptance range:

$$\gamma - \Delta\gamma \le S_{duy} \cos(du_z) \le \gamma + \Delta\gamma \qquad (5.11)$$

Any beams that were incident in this range were thus incident upon the detector. The weights of these beams were then accumulated in the component variables used to calculate the HNHR. These variables were a) the heterodyne signal reaching the detector $S_{heterodyne}$, b) the "false heterodyne" signal reaching the detector $S_{falseheterodyne}$ and c) the non-heterodyne signal reaching the detector $S_{nonheterodyne}$. These component parts are discussed below in sections 5.3.4.3 and 5.3.4.3.1; in this section we merely recount how they were determined.

The optical pathlength l_{path} of the "coherent beam" under test was compared to the optical path length range limits defined by the user and the optical source coherence length, thus:

$$l_{ref} - \frac{l_{source}}{2} \le l_{path} \le l_{ref} + \frac{l_{source}}{2} \qquad (5.12)$$

If this condition was not satisfied, the weight of the beam under test was added to the incoherent non-heterodyne signal total $S_{nonheterodyne}$. If it was satisfied, a further test was performed to indicate if the beam had sampled the embedded cylinder. If the beam had sampled the cylinder the respective weight was added to the heterodyne signal total $S_{heterodyne}$, and if it had not sampled the cylinder the weight was added to the false heterodyne signal total $S_{falseheterodyne}$.

It should be noted that the profile of the heterodyne "gate" in terms of pathlength, or equivalently time-of-flight, was assumed to be rectangular across the range of pathlengths measured: e.g. a beam, or photon, arriving at the detector having

travelled an optical pathlength of $l_{ref} - \dfrac{l_{source}}{2}$ was given an equal weighting to one having travelled an optical pathlength of l_{ref}. This parameter could, however, have been easily varied so as to weight beams or photons reaching the detector according to a non-constant gate profile. For example, a Gaussian multiplication factor could be applied to the heterodyne gate profile to attribute a smaller amount of the total weight of an individual beam/photon to the non-heterodyne signal (and a greater proportion to the heterodyne signal) for those beams whose optical pathlength is close to l_{ref} than for those pathlength is closer to $l_{ref} \pm \dfrac{l_{source}}{2}$. Such a weight apportioning scheme would permit quasi-coherent light to be taken into account in any analysis of the Monte Carlo data. Furthermore, it would be possible to re-estimate a simulated measurement of the contribution of quasi-coherent light to the heterodyne signal according to any selection criteria without the need to re-run any of the time-consuming Monte Carlo simulations since the analysis tool is able to apply quasi-coherent gating to the data sets retrospectively.

5.3.4.2 Analysing the Monte Carlo generated photons reaching the detector

The output of the simulation consisted of binary blocks of data which registered the output parameters of those photons that had left the sample surface. In much the same way as for the beams in the last section, the photons were checked to see whether they fell onto the detector area. The main difference between these photons and the beams of the last section lay in the method for analysing whether the photons fell within the detector acceptance area: this was because the assumption that the x-component of the direction cosine was equal to zero was now no longer necessarily correct.

Binary data was read from the saved Monte Carlo data files in blocks of 1,000 photons at a time so as not to unnecessarily delay the analysis tool by performing multiple (slow) disk reads to access the data on the disk.

We again used the values (du_x, du_y, du_z) to define the direction cosines of the individual photons leaving the sample surface. The direction cosines $(du_{x\gamma}, du_{y\gamma}, du_{z\gamma})$ of the central axis of the detector (at angle γ) were thus:

$$du_{x_\gamma} = 0, du_{y_\gamma} = +\sqrt{1 - \cos^2(\gamma)}, du_{z_\gamma} = \cos(\gamma)$$ (5.13)

The angle between the direction vector of the photon and the central axis of the detector γ' was found from the following equation:

$$\cos(\gamma') = du_x\ du_{x\gamma} + du_y\ du_{y\gamma} + du_z\ du_{z\gamma}$$ (5.14)

Satisfaction of the condition $|\Delta\gamma| \leq |\gamma'|$ then indicated that the photon had reached the detector. The optical pathlength test of the last section was then invoked and the weights of the non-heterodyne and "false heterodyne" photons reaching the detector were added to the appropriate signal components for forming the HNHR ($S_{nonheterodyne}$, $S_{falseheterodyne}$), but any signal that was deemed to give rise to a heterodyne signal was not scored since this would have meant counting both the analytically added coherent component and the Monte Carlo simulation generated heterodyne signal component.

5.3.4.3 Calculate and save the measured HNHR

Once all the "coherent" beam and the Monte Carlo data had been analysed, the HNHR was calculated according to equation 5.15 below and the results added to the analysis data file in tab-delimited format for subsequent importing into a commercial graphing and/or analysis package such as SigmaPlot or Excel. (Step 16 of Figure 5.1)

$$HNHR = \frac{S_{heterodyne} + S_{falseheterodyne}}{S_{nonheterodyne}}$$ (5.15)

Then either the central starting position of the detector area was incremented, the next batch file initialised or the program terminated. (See steps 17 to 19 of Figure 5.1.)

5.3.4.3.1 "False heterodyne" signal

Conceptually the "false heterodyne" signal is all that light reaching the detector within the confines of its area, acceptance angle and coherence pathlength gate range which has not sampled the region or feature of interest for which that coherent pathlength gate has been set. In this way it is notionally slightly different from diffuse signal reaching the detector in that the added dimension of coherence needs to be taken into account. Further it is a portion of the signal which, as far as any measured HNHR is concerned, contributes to the heterodyne signal, whereas in reality it actually degrades the HNHR by admitting light to the detector which has not sampled the region of interest.

Such signal forms one part of the natural diffuse reflection signal that arises from multiply scattered light, but it may also arise as a result of light which is multiply reflected. For example, it could include signal that gets multiply reflected within a thin surface layer but which does not sample an embedded cylinder which is the primary interest to the end user.

It should be noted that the false coherent signal component could possibly be reduced by a factor of up to 50%, in any physical experiment, by the use of polarising filters[1,2,3,4] placed in front of the detector. Such a reduction would be possible if the false heterodyne component's polarisation was completely randomised. We, however, did not account for the polarisation of photons travelling in the sample, and this thesis makes no further comment regarding this point.

The Monte Carlo analysis tool was able to quantify the amount of "false heterodyne" signal for any particular sample and recorded such information along with the other components forming the HNHR.

5.4 Utility programs

Some of the utility programs developed to aid in the analysis of data and selection of initial parameters for use in the Monte Carlo simulation itself are mentioned briefly below, without going into excessive detail.

5.4.1 Coherent beam tracing utility

The coherent beam tracing utility injected beams across the surface of the same sample as simulated in the Monte Carlo simulation and traced them in a manner analogous to that in section 5.3.3. A user-defined range and number of beams could by injected at various positions on the y-axis, all at fixed input angle θ. Using the same tracing and splitting technique as above (5.3.3) any emergent beams were recorded in an output data file which recorded for each surface input y-position, the position of any beam intercept at the cylinder boundary and the optical path length travelled. This output file was then analysed to see which beams had hit the cylinder surface nearest to its uppermost point and with minimum optical pathlength: that beam was then used as the central input beam in the Monte Carlo simulation itself.

5.4.2 Binary data file to text data file conversion

This was a simple program for converting the binary files generated by the Monte Carlo simulation to tab-delimited text files. This permitted both visual inspection of the saved data for debugging purposes and enabled statistical analysis to be performed on the data (e.g. finding the average optical path length travelled by the photons) using software tools such as Excel^{TM}, SigmaPlot^{TM} or SigmaStat^{TM}.

Chapter References

[1] W. H. Press, S. A. Teukolsky, W. T. Vetterling and B. P. Flannery, *Numerical Recipes in C: The Art of Scientific Computing*, (Cambridge University Press, Cambridge, 1993)

[1] M. R. Hee, D. Huang, E. A. Swanson and J. G. Fujimoto, "Polarization-sensitive low-coherence reflectometer for birefringence characterisation and ranging," *J. Opt. Soc. Am. B*, Vol. 9, No. 6, pp. 903-908, 1992

[2] M. Dogariu and T. Asakura, "Polarisation dependent backscattering patterns from weakly scattering media," *J. Optics (Paris)*, Vol. 24, No. 6, pp. 271-278, 1993

[3] C. Brosseau, "Depolarization behaviour of multiple scattered light from an optically dense random medium," *Pre-print of paper submitted to Opt. Soc. Am. meeting Advances in optical imaging and photon migration*, Orlando, Florida, March 18-22, 1996

[4] V. Sankaran, K. Schönenberger, J. T. Walsh Jr. and D. J. Maitland, "Polarization discrimination of coherently propagating light in turbid media," *Appl. Opt.*, Vol. 38, No. 19, p. 4252, 1999

Monte Carlo results and conclusions

The main results in this chapter were derived from simulations performed on a so-called core model which corresponded to a tissue equivalent phantom model that we had made at UCL for use in an experimental scanning low-coherence interferometric system: see Chapter 7 for details. This core model was designed to simulate the physical and optical properties of a large blood vessel embedded in dermis beneath a layer of epidermis and stratum corneum respectively. The actual phantom was constructed from a three-layered glass sphere bearing epoxy resin material with an embedded cylinder of dyed epoxy resin used to simulate blood. The phantom was manufactured using the method of Firbank et al[1]. Further details of the core model are given below in section 6.1.

The simulations performed on the core model were used to test the hypothesis presented in chapter 1 (see section 1.4) by investigating the effect of scanning an angled detector, at angle γ with respect to a normal to the sample surface, across the sample surface with a fixed input beam profile, incident at angle θ (see Figure 6.1 for an illustration of this geometry). Results are shown below in Figures 6.4 to 6.7 for various incident beam angles (θ), detector angles (γ) and detector acceptance angles ($\Delta\gamma$). These results show the effect of progressively reducing the size of the detector at the surface of the sample: the diameter of the detector was varied from 0.6 mm to 0.2 mm to 0.1 mm to 0.05 mm respectively.

The results are discussed in section 6.3, and we finally draw our conclusions from them in section 6.4

6.1 The core model

A schematic of the core model is shown in Figure 6.1: this figure corresponds to Figure 4.1 of chapter 4 and is shown again below for convenience. The core model was composed of a number of elements, namely: multiple layers; a blood vessel; an incident beam; and an initial set of detector parameters which gave a starting point from which variations were made to obtain the results presented below in Figures 6.8 and 6.9. The values chosen to characterise these elements of the simulation, and the

reasons for choosing such values, are discussed individually for each element in sections 6.1.1 to 6.1.4 below.

Figure 6.1: The core model*
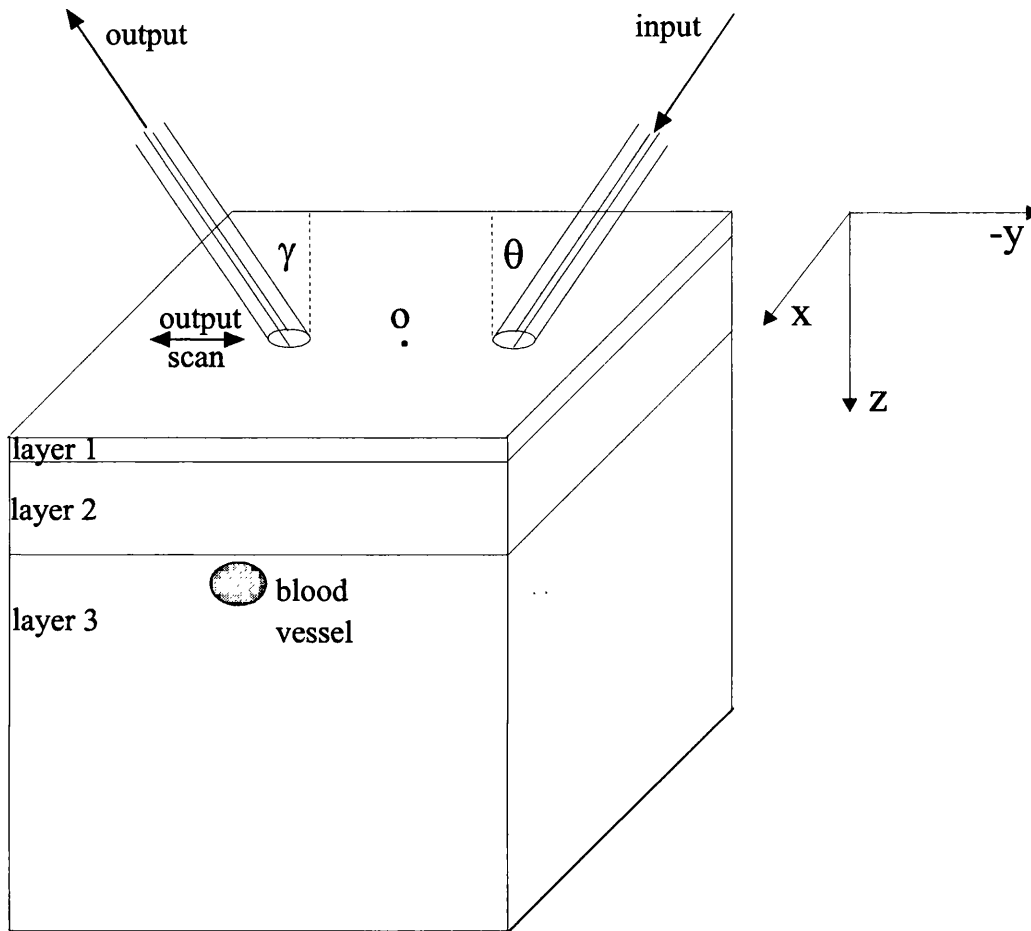
* Note that both the central point of the incident beam and the central point of the output beam lie in the y-z plane and are co-linear with the origin (0,0,0) O.

6.1.1 The layers

The simulation allowed for a model configuration using three separate planar layers, the deepest (layer 3) containing an embedded cylinder. This was in an attempt to approximate the physical structure of skin tissue (see Figure 3.1). Skin is in essence a three layered structure composed of a thin upper-most layer of highly scattering tissue (stratum corneum) on top of a thicker but less highly scattering layer of epidermis. The epidermis separates the stratum corneum from the dermis in which are found blood vessels.

111

As mentioned earlier, another reason for using a three planar-layered model with an embedded cylinder was that it could easily be made using tissue phantom materials such as those developed at UCL[1] (see Chapter 7). Such a planar layer arrangement was readily reconfigurable, the individual layers being index matched together using ethyl cinnamate to eliminate reflections at the boundaries, thereby permitting the construction of different samples with various optical and physical properties for use in experimental systems. The layer thicknesses, refractive index, absorption and scattering coefficients etc. could then all be changed by swapping layers for those of different optical properties.

The literature (see Table 3.1) teaches that all three skin layers, dermis, epidermis and stratum corneum, have approximately the same absorption coefficient due in part to their absence of chromophores such as haemoglobin. Because of this all the layers in the core model were set to have the same absorption coefficient as for near-infrared light travelling through skin tissue: this value was set to be 0.04 mm^{-1}.

The uppermost layer (layer 1 in Figure 6.1) was chosen to be 0.1 mm thick and to have a scattering coefficient of 20 mm^{-1}. These values allowed for a layer that it was feasible to make from phantom material; the stratum corneum itself is usually some 10 μm (0.01 mm) thick and has a scattering coefficient of some 100-200 mm^{-1}. Machining extremely thin layers of phantom material to a uniform thickness is difficult, as is making a phantom material with an extremely high scattering coefficient since the glass spheres used to adjust the scattering coefficient are thought to clump together when they are used in high densities[1]. Consequently, a thicker layer of material with a lower scattering coefficient than for real stratum corneum was used in the model, but which had the same thickness/scattering coefficient product as real stratum corneum: *viz.* 0.1 mm x 20 mm^{-1} = 10 μm x 200 mm^{-1} = 2.

The layer approximating epidermis (layer 2 in Figure 6.1) had a slightly lower scattering coefficient than did layer 1. It had a scattering coefficient of 10 mm^{-1} and was 0.5 mm thick. Such parameters were consistent with those measured in real tissue samples for epidermis. The layer in which the cylinder was embedded (layer 3 in Figure 6.1) was also chosen to have a scattering coefficient of 10 mm^{-1} and extended to a depth, adjustable using a simulation initialisation parameter, of 20 mm.

The optical properties of this layer were also consistent with known measured values for the dermis layer, as was the use of a g-factor of 0.9 for both layers 2 and 3.

Photons reaching a depth, or radial distance, of 20 mm in layer 3 were terminated so as to speed the simulation, as their average weight factor would be reduced to a fraction e^{-200} of their weight at the upper boundary of layer 3. This meant that any photons returning from this depth would be considered to be below the shot noise limit of any detection system at the sample surface ($\approx$-140dB[2]). Their contribution to the SNR at the detector was therefore deemed insignificant and this justified their termination.

All the layers in the core model had a refractive index of 1.56. This value was chosen because it corresponded to the refractive index of the tissue-equivalent phantom material developed at UCL[1]. Thus, the effect of using the parameters described above for layers 2 and 3 was to merge them into a single layer, so although the simulation was coded as a three-layered model, the parameters used in the initialisation of the core model reduced it to being a two-layered model. Coding in such a way permitted the model to be used at a later date for simulating variations from these core values.

6.1.2 The blood vessel

An embedded blood vessel was simulated as a cylinder within layer 3. The cylinder properties were chosen to approximate those of a blood vessel embedded in the dermis and the optical parameters used were derived from the existing literature[3,4,5,6] (see Table 3.1). The refractive index was chosen to provide an index mismatch that gave the same Fresnel reflection coefficients as for that between the outer blood vessel layer and the dermis itself in real tissue. In this case that necessitated using a refractive index of 1.51 for the embedded cylinder. It was known from previous experiments (see chapter 3) that blood is highly forward scattering over the range of wavelengths considered here, and we took a scattering phase function having a g-factor of 0.995 to reflect this. The other optical parameters of blood were taken to be: $\mu_a = 0.6$ mm^{-1}; $\mu_s = 14.9$ mm^{-1}.

A large (1.0 mm) diameter vessel was used as this was expected to give a reasonably high HNHR, and was considered to be the largest magnitude of vessel size that was likely to be found in the upper reaches of the skin. The vessel was placed at a depth of approximately 0.6 mm below the surface of layer 1, on the assumption that this should provide experimentally a signal with adequate HNHR (in a homogeneous slab the coherent signal, which gives rise to a heterodyne signal, of a normally incident beam would be reduced to some 6×10^{-6}, or -100 dB, of its incident value. This level is measurable bearing in mind that sensitive photodiodes can easily detect light levels at the picowatt level). The blood vessel lay parallel to the x-axis of Figure 6.1.

6.1.3 The incident beam

The incident beam is marked "input" in Figure 6.1. Since the aim of this study was to investigate the effects upon the measured HNHR of tilting the incident beam with respect to the sample surface, several simulations were needed using the core model each with a differing incident beam angle. We used input angles θ which formed an angle of 0, 10, 20, 30 and 40 degrees with the z-axis. The beam was unpolarised.

For each input angle 500,000 photons were simulated going from air into layer 1. The respective refractive indices being 1.00 and 1.56. Each input profile was simulated as an unfocused but collimated beam (i.e. a set of parallel photon trajectories at the surface) of Gaussian distribution and with a beam $\frac{1}{e}$ width of 0.6 mm. This input profile corresponded to the profile available from a collimated fibre optic light delivery system that was at our disposal (see Chapter 7).

In all the simulations, the trajectory of a ray at the centre of the input beam profile was made to hit the surface of layer 1 at a point $(0,y,0)$ that (allowing for surface reflection) caused it to be incident at the uppermost point of the cylinder. This ensured that the signal giving rise to a heterodyne signal returning from the cylinder, which was the feature of interest to be imaged, followed the shortest path in the surrounding tissue. This meant that the HNHR for this geometry would be the maximum obtainable. The y-value of the central surface input point, which lay upon the $x = 0$ axis, was calculated by ray tracing a sequence of photon paths incident in

114

the *y-z* plane using the program "coherent.exe" written for this purpose (this is described briefly in section 5.4.1).

6.1.4 The detector

The detector parameters were configurable by changing the initialisation parameters of the analysis tool (see section 5.3.4). However, some of the parameters that could be varied were not, and these are described in this section along with the reasons why they were kept constant and their physical significance.

As low-coherence interferometry is concerned with localising the region from which heterodyne signal is sampled by what essentially amounts to optical path length discrimination between photons that may be deemed coherent (gives rise to a heterodyne signal component) or incoherent (gives rise to a non-heterodyne signal component), it was necessary to select a discriminating path length within which photons could be deemed coherent and outside which they were deemed to be incoherent (the heterodyne "gate" - see section 5.3.4.1). As the cylinder was the feature of interest, the centre of the coherence window was set to coincide with the uppermost point of the cylinder for whatever configuration of sample geometry and input parameters were used. This value of optical path length was also found for each simulation (for differing incident angles) using the simulation tool "coherent.exe".

The heterodyne gate defined the deviation from the optical path length in which photons arriving at the detector were considered to be coherent with others arriving within that range, and thus to give rise to a heterodyne signal: anything outside that range being considered incoherent and giving rise to a non-heterodyne signal contribution. It corresponded physically to the coherence length of the light source used to illuminate the sample. The heterodyne gate was fixed at an optical path length deviation of 0.078 mm. This corresponded to a source having a coherence length of 50 μm measured in air. A coherence length of 50 μm is typical of commercially available superluminescent diodes. The heterodyne gate profile was constant (see section 5.3.4.1) and so did not account for quasi-coherent light reaching the detector.

In all cases the angle formed between the axis of the output and input beams and the z-axis was the same. For the analyses of this section, a variable diameter pin-hole was scanned across the sample surface with a central position varying from $y = -4.00$ mm to $+4.00$ mm in steps of 40 µm size. Such a step size was slightly less than the coherence length of the source in air, and the range chosen was calculated to encompass likely coherent reflections from the surface of the cylinder down to depths of 6.00 mm or so; a depth well in excess of any that was actually used during the simulations we performed. The size of the pin hole remained constant during each scan, and photons or coherent beams falling within the pin-hole area were gated according to whether they fell within a cone defined by the detector angle γ of the output beam plus or minus half of a cone acceptance angle ($\pm\Delta\gamma/2$).

6.2 Results generated using the Monte Carlo model and analysis tool

Figures 6.2 to 6.5 below illustrate the results of performing radial scans across the surface of the core model along the $y = 0$ axis for various detector geometries. Figures 6.6 and 6.7 show the effect of similar scans with the core model modified as indicated. These results are discussed and analysed further in section 6.3 below.

Figure 6.6 shows the effect on HNHR of changing the input beam profile from a 0.6 mm Gaussian beam to an infinitely narrow point beam. The data is shown for the point beam incident on the core model sample, and for angles of incidence of $0°$ and $10°$. The detector parameters were fixed at $\Delta\gamma = 15°$ and the detector diameter was 0.1 mm.

Figure 6.7 shows the effect of changing the refractive index of the uppermost layer from 1.56 to 1.727 for input beams at $0°$ and $40°$. The value of 1.727 was chosen as it gave rise to approximately the same Fresnel reflection coefficient as for two layers having refractive indices of 1.4 and 1.55 respectively: these latter two values being, respectively, the generally accepted refractive indices of epidermis and stratum corneum in the near-infrared region of the optical spectrum. Again, the detector parameters were fixed at $\Delta\gamma = 15°$ and the detector diameter was 0.1 mm.
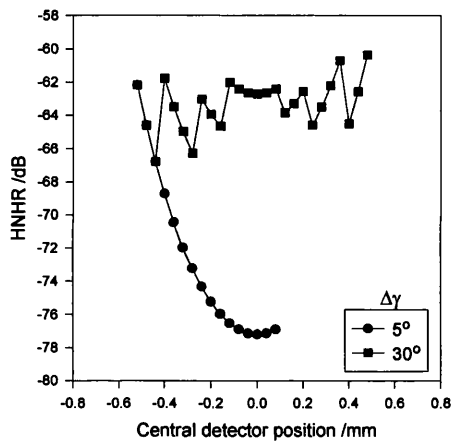
Figure 6.2: HNHR for various incident beam (Θ) and detector (γ) angles; detector diameter = 0.6 mm
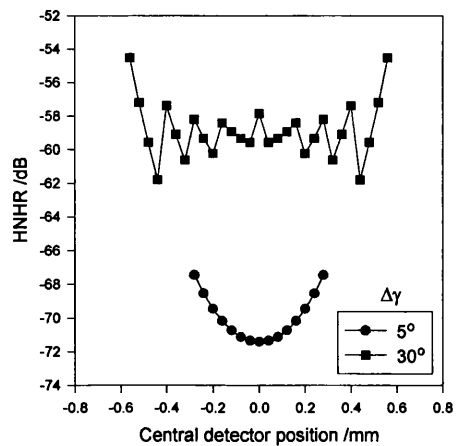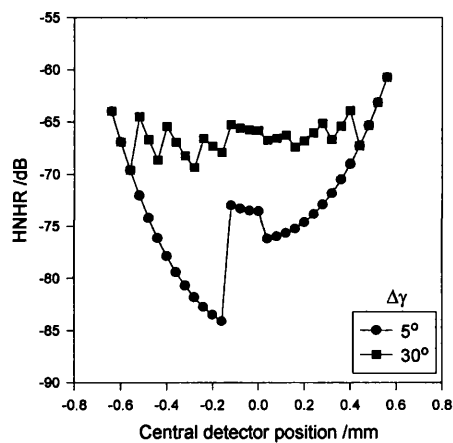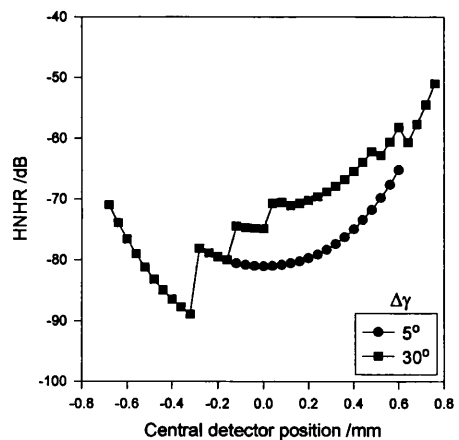

a) Beam incident at 0°
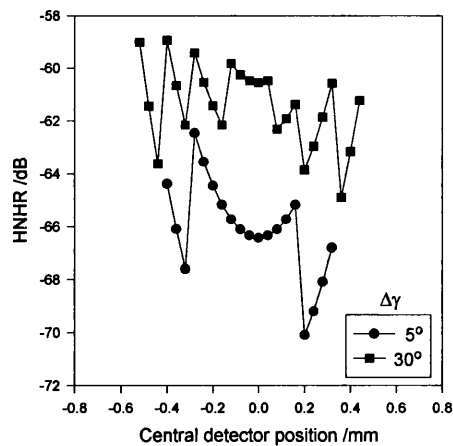
b) Beam incident at 10°

c) Beam incident at 20°

d) Beam incident at 30°

e) Beam incident at 40°

117

Figure 6.3: HNHR for various incident beam (θ) and detector (γ) angles;

detector diameter = 0.2 mm

a) Beam incident at 0°

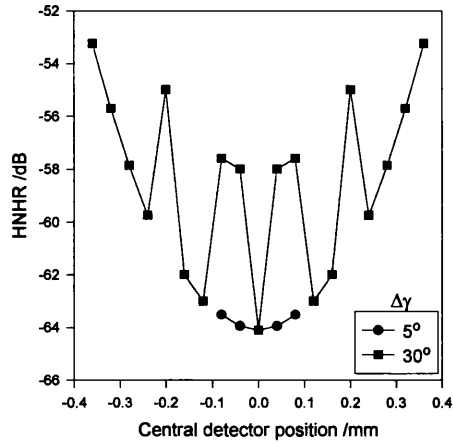b) Beam incident at 10°

c) Beam incident at 20°

d) Beam incident at 30°

e) Beam incident at 40°

118

Figure 6.4: HNHR for various incident beam (θ) and detector (γ) angles;

detector diameter = 0.1 mm

a) Beam incident at 0°
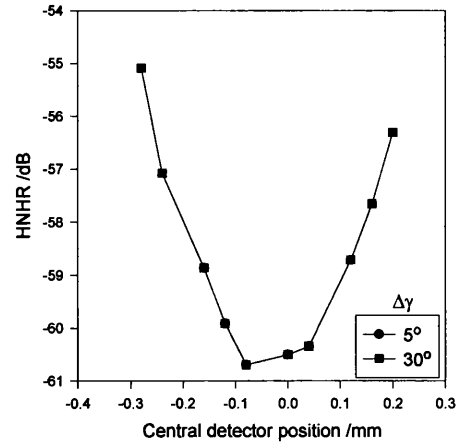
b) Beam incident at 10°

c) Beam incident at 20°
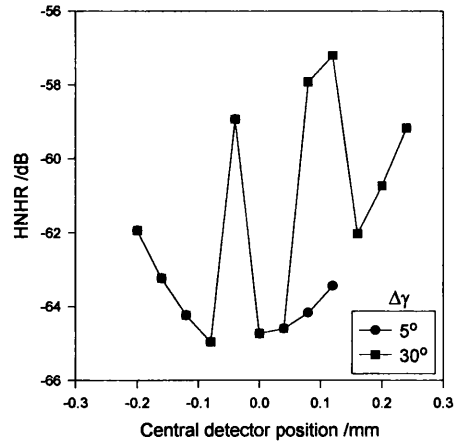

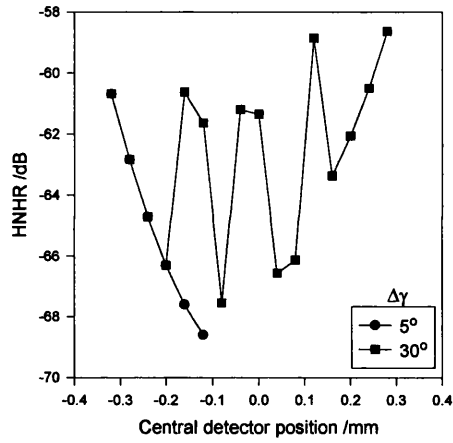d) Beam incident at 30°

e) Beam incident at 40°

119
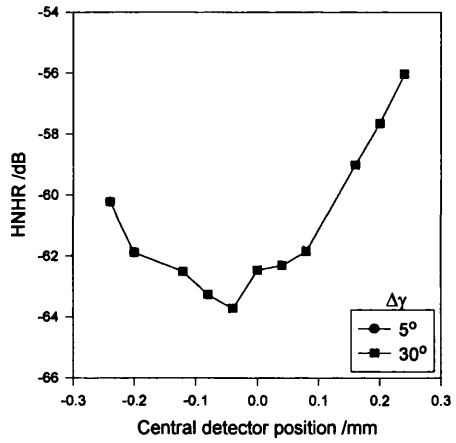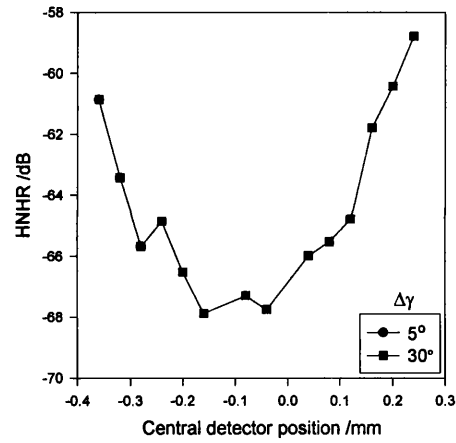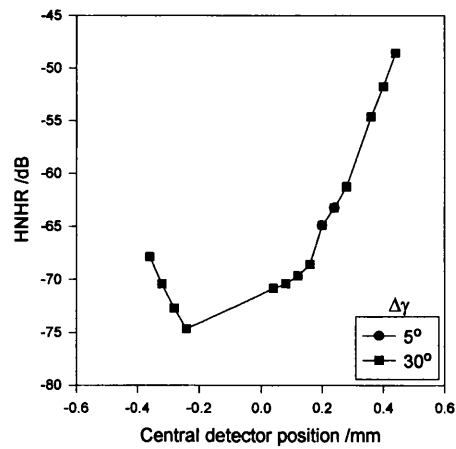
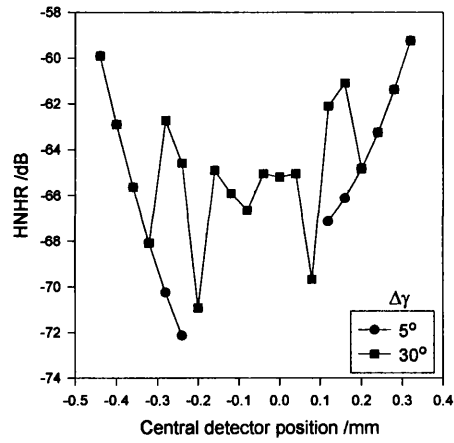**Figure 6.5: HNHR for various incident beam (θ) and detector (γ) angles; detector diameter = 0.05 mm**
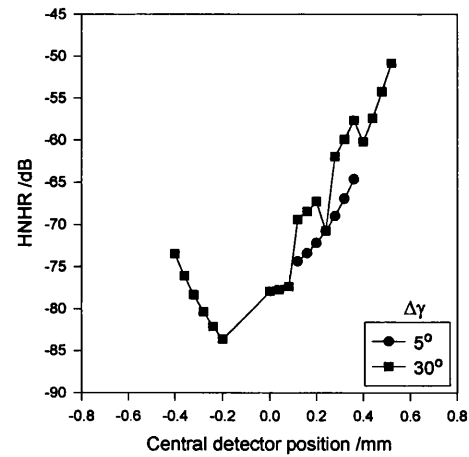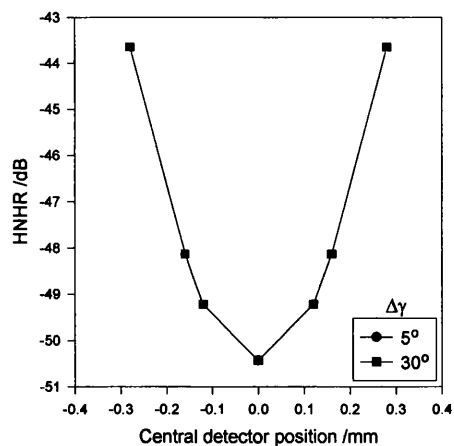
a) Beam incident at 0°

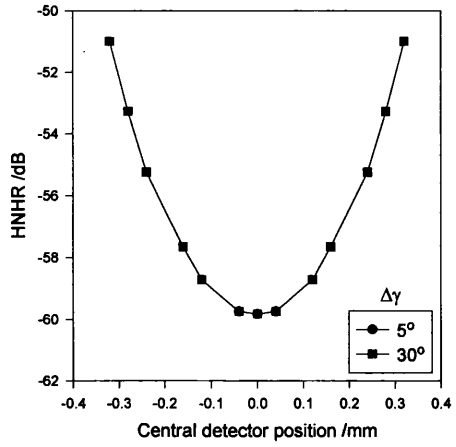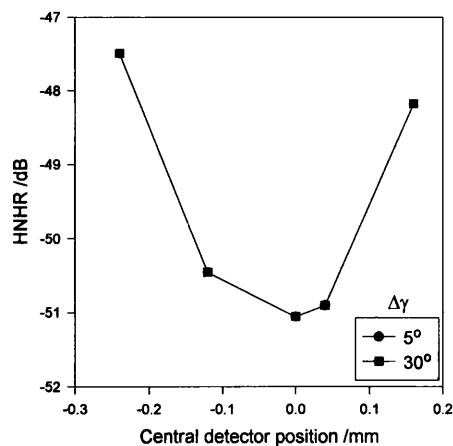b) Beam incident at 10°
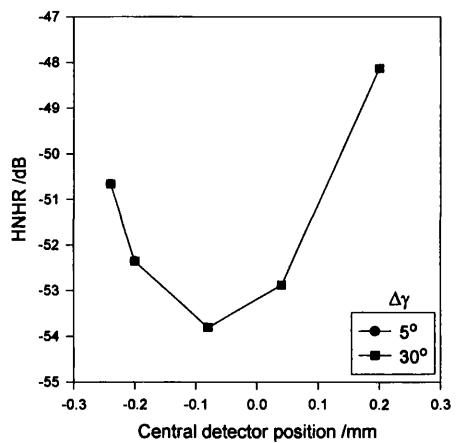
c) Beam incident at 20°
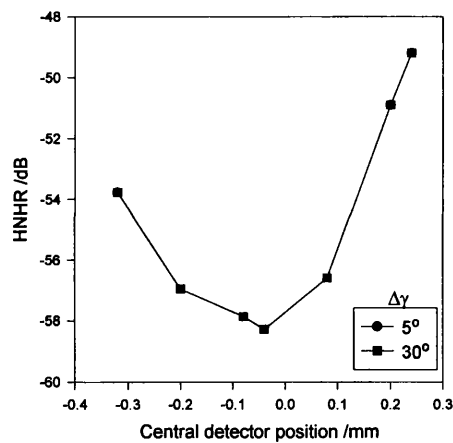
d) Beam incident at 30°
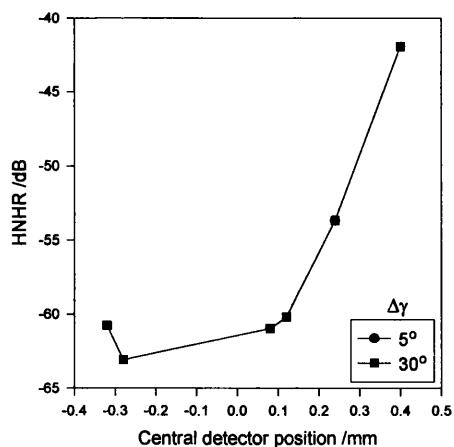
e) Beam incident at 40°

120

Figure 6.6: Comparison of HNHR for core model with 0.6 mm Gaussian beam and point beam illumination for various incident beam and detector angles (θ = γ); detector diameter = 0.1 mm, Δγ = 15°

a) θ = γ = 0°
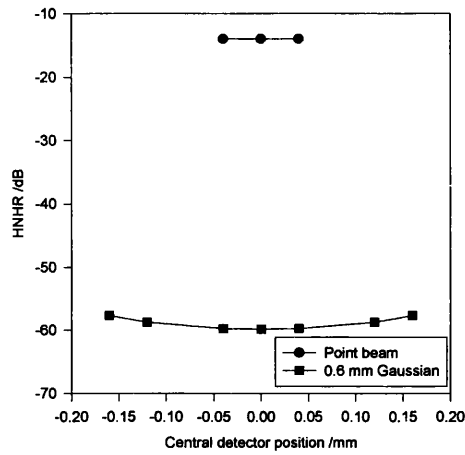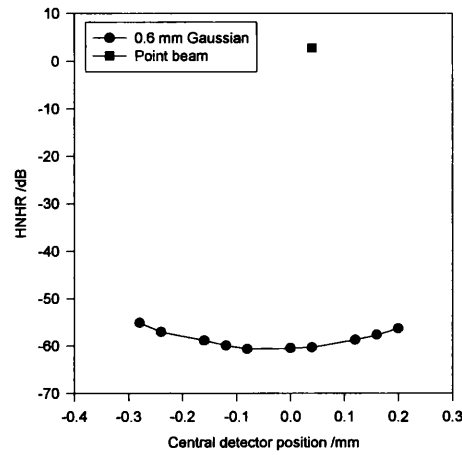
b) θ = γ = 10°

Figure 6.7: Effect of changing the refractive index of the uppermost layer from 1.56 to 1.727 for various incident beam and detector angles (θ = γ); detector diameter = 0.1 mm, Δγ = 15°

a) θ = γ = 0°

b) θ = γ = 40°

121
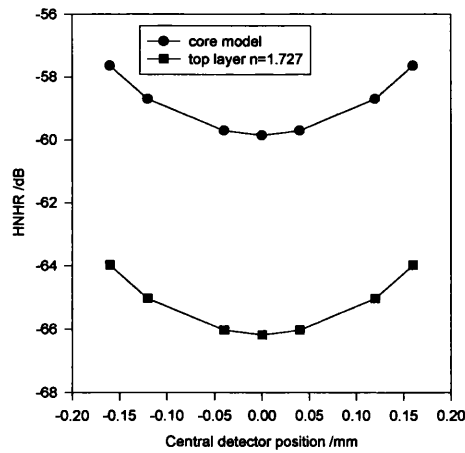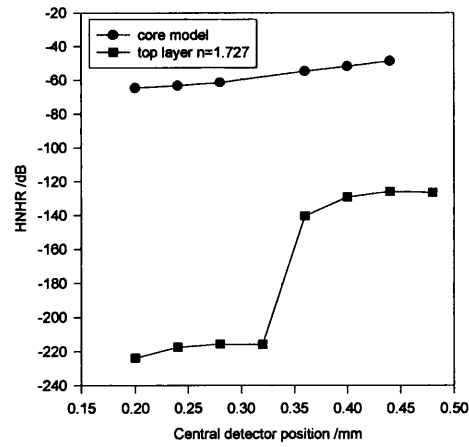
6.3 Discussion of Monte Carlo generated results

Figure 6.2 shows the HNHR profile for a 0.6 mm diameter detector area scanned across the surface of the core model. In this case the incident beam delivery system and detector were degenerate, i.e. $\theta = \gamma$.

As the detector area was scanned across the surface at normal incidence (for $\theta = \gamma = 0°$), it began to encompass heterodyne signal that had sampled the cylinder surface. As the edge of the detector area encompassed this heterodyne signal, i.e. when the central detector position (*cdp*) of the detector area was at about -0.35 mm for the 5° acceptance area of Figure 6.2 a), a measurable HNHR arose. Beyond this point, when *cdp* < -0.35 mm, no heterodyne signal, and therefore no HNHR, was measurable although there was a detectable non-heterodyne component.

As the detector area moved further across the sample surface, from *cdp* = -0.35 mm towards *cdp* = 0.0 mm (where the detector area was coincident with the centre of the centre of the incident beam), the heterodyne component of HNHR increased along with the non-heterodyne signal component. In this case, the contribution to the HNHR by the non-heterodyne component increased more rapidly than the contribution to HNHR by the heterodyne signal reaching the detector. Consequently, the HNHR dropped as the detector area approached the point where *cdp* = 0.0 mm. This profile was reversed as *cdp* moved from 0.0 mm to about 0.3 mm, and produced the parabolic shape seen in Figure 6.2 a) for $\Delta\gamma = 5°$.

The shape seen in Figure 6.2 a) for $\Delta\gamma = 30°$ can be understood from the curve for which $\Delta\gamma = 5°$. The curve is composed of an average parabolic profile with superimposed spiky structure. The spikes were caused by quantisation of the coherent analytical beam, i.e. the component beams of which fanned out angularly from the point at which they sampled the cylinder surface. As the value of $\Delta\gamma$ increased, more of these coherent beams were recorded at the detector and this explains the shape of the profile observed. Here the average parabolic profile is shallower than that of the case for which $\Delta\gamma = 5°$. The shallower averaged profile was believed to be due to the non-heterodyne signal component of HNHR being distributed over a wider angular range than the heterodyne signal component,

following randomisation of the angular distribution for the emergent non-heterodyne light as a result of multiple scattering. This gave rise to more non-heterodyne signal being recorded at the detector as $\Delta\gamma$ was increased from $5°$ to $30°$.

The curves in Figures 6.2 a) to e) show the effect of increasing the incident beam angle θ from $0°$ to $40°$. In all cases, the curves with the highest value of $\Delta\gamma$ produced a higher mean value of HNHR. A parabolic tendency similar to that seen and previously described for Figure 6.2 a) is also seen in the curves of Figures 6.2 b) to e), however the mean value of the curves skewed increasingly as the detector angle γ increased to $40°$.

The curves in Figures 6.2 c) and d) show a relatively small positive difference in mean HNHR between scan extremities, when *cdp* was varied between an extreme negative and extreme positive position. The data in Figure 6.2 b), shows a slight negative difference. This seems to imply that little increase in the observed HNHR will be seen (or even a small decrease), when a large area detector is scanned across the sample shown in Figure 6.1 and illuminated using a relatively large diameter incident beam.

Only when $\theta = \gamma = 40°$, as shown in Figure 6.2 e), did the heterodyne component of HNHR dominate significantly the non-heterodyne component of HNHR. In this case a pronounced skew was observed in which the mean value of HNHR seen at *cdp* ~ -0.7 mm was some 25 to 30 dB lower than that observed at *cdp* ~ 0.7 mm, the absolute mean value varying from around -80 dB to about -55 dB. This compares to a mean value seen in Figure 6.2 a) varying from about -58 dB to about -59 dB.

Thus the results in Figures 6.2 indicate that overall mean measured HNHR can be enhanced slightly by decoupling the incident and detector arms by an increasing angular amount (-58 dB at *cdp* = 0.45 mm with $\Delta\gamma = 30°$ for $\theta = \gamma = 0°$, to -55 dB at *cdp* = 0.7 mm with $\Delta\gamma = 30°$ for $\theta = \gamma = 40°$). However, the difference (contrast) in mean HNHR seen between the extremities of the scan as *cdp* moves from negative to positive is only enhanced significantly for relatively large angular separations of the incident and detector arms (25 to 30 dB for $\theta = \gamma = 40°$).

Figures 6.3 to 6.5 show the effect of reducing the size of the detector area from a diameter of 0.6 mm to 0.05 mm. These figures all show broadly similar characteristics to the curve in Figure 6.2: i.e. a parabolic profile for a degenerate normally incident input beam/detector profile ($\theta = \gamma = 0°$) with only a marked skew in the profile as the incident and detection angles were separated and increased towards $\theta = \gamma = 40°$. The spiky structure, however, tended to reduce as fewer of the coherent beams reached the detector area: this was particularly marked for detector diameters of 0.1 and 0.05 mm.

The mean value of HNHR for a working angle of $\theta = \gamma = 40°$ remained at a similar level for detector diameters of 0.6, 0.2 and 0.1 mm (HNHR at maximum negative value position of the central detector position $\approx$ -70 dB rising to $\sim$ -50 dB at the maximum positive value of the central detector position). However, for a detector area of 0.05 mm, the mean value of HNHR increased by some 10 dB between the two extremities of the scan in comparison to the other detector diameters. This phenomenon was also observed for the other incident angles, and appears to indicate that use of an increasingly small detector angle will increase the measured HNHR. This is to be expected when one considers that a reduced detector area is a closer approximation to a confocal system.

Figure 6.6 shows the effect of changing the input beam from a collimated Gaussian beam to an infinitely narrow point beam. As for the Gaussian beam, a HNHR improvement was seen when the point input beam/detector system was decoupled: in this case the difference between a degenerate input/detection system and one having $10°$ of tilt was 16.6 dB. There was also seen to be a marked improvement in HNHR, for both Figures 6.6 a) and b), when using a point input beam as opposed to a collimated Gaussian input beam: in this case the improvement was some 55 to 60 dB.

Figure 6.7 shows how the HNHR was affected by changing the refractive index of layer 1 of the model from 1.56 to 1.727. For a degenerate input/detection system ($\theta = \gamma = 0°$), a systematic reduction of approximately 6 dB was observed. For a decoupled detection/delivery system at $\theta = \gamma = 40°$, the measured HNHR for the

124

model having a high refractive index layer 1 dropped to below the limits that would be physically measurable (~ -140 dB).

6.3.1 Error sources

The background Monte Carlo simulated data is smooth as witnessed by the smooth parabolic envelope. The error due to the statistics of the Monte Carlo data was deemed small (< 1dB of noise is seen in Figures 6.2 to 6.7 which is attributable to the Monte Carlo data). Furthermore, a comparison of the Monte Carlo data to the analytical model of Figure 4.10 shows a good fit over the radial range of the scans we performed here (-4.0 to 4.0 mm). The main source of error was thus thought to be due to quantisation of the coherent input beam. Estimates of this error source were put at ~5 to 6 dB based on the variance ("spikiness") in HNHR seen in Figures 6.2 and 6.7.

6.4 Conclusions

The benefit of using a confocal illumination and detection system is confirmed by the results which show an improved mean HNHR when using a narrow illumination input beam (+60 dB) and a reduced detector surface area (+10 dB for a 0.05 mm detector diameter), when compared to a collimated system using a 0.6 mm Gaussian beam illumination with a 0.6 mm diameter detector.

In answering the question posed in section 1.4: separating the degenerate input and detection beam orientation does not appear to improve the HNHR *per se*. It does, however, seem to improve the differential HNHR (by up to some 25 to 30 dB for certain of the cases studied) measured between the extremities of a radial scan when imaging a relatively large object embedded in a composite turbid media. However, this HNHR differentiation disappears when the stratum corneum is allowed to remain as the uppermost layer, as it prevents most of the coherent signal emerging from the sample by virtue of total internal reflection.

Therefore, if such HNHR differentiation is to be of practical value, for example to improve the contrast in images obtained using a degenerate low-coherence interferometer, either the stratum corneum needs to be removed from the sample or

the detector and light delivery systems need to be more closely index matched to the sample in question. It is known that the stratum corneum can be "clarified" by use of hydrating solutions and creams (in the main containing water and propylene glycol). These reduce the refractive index of the stratum corneum and its scattering coefficient. The external surface reflection could be further reduced by having a contact glass or plastic sheet against the skin, which could be used to couple the optical system to the skin.

Chapter References

[1] M. Firbank, M. Hiraoka and D. T. Delpy, "Development of a stable and reproducible tissue equivalent phantom for use in infrared spectroscopy and imaging," *SPIE proceedings,* Vol. 1888, pp. 264-270, 1991

[2] A. Yariv, *Optical Electronics*, (Saunders College Publishing, Philadelphia, 1991)

[3] W. F. Cheong, S. A. Prahl and A. J. Welch, "A review of the optical properties of biological tissues," *IEEE J. Quan. Electronics,* Vol. 26, No. 12, pp. 2166-2185, 1990

[4] L. Reynolds, C. Johnson and A. Ishimaru, "Diffuse reflectance from a finite blood medium: applications to the modelling of fiber optic catheters," *Appl. Opt.,* Vol. 15, No. 9, pp. 2059-2067, 1976

[5] G. D. Pederson, N. J. McCormick and L. O. Reynolds, "Transport calculations for light scattering in blood," *Biophys. J.,* Vol. 16, pp. 199-207, 1987

[6] J. M. Steinke and A. P. Shepherd, "Comparison of Mie theory and the light scattering of red blood cells," *Appl. Opt.,* Vol. 27, No. 19, pp. 4027-4033, 1988

Experimental details

This chapter describes an experimental low-coherence interferometer built by the author. It was used to perform unfocussed degenerate light delivery/collection scans in samples made from phantom materials. The component parts of the interferometer are described in detail in sections 7.1 to 7.3 below. Following discussion of the experimental system, some general comments are made on the experimental design in section 7.4, including a brief mention of some of the practical problems encountered whilst setting-up and performing the experiments. Details of the construction of the tissue equivalent phantoms used as samples is then given in section 7.5. Some of the results obtained using the experimental system are presented in section 7.6 and then discussed in section 7.7. In section 7.8 we draw our conclusions and finally, in section 7.9, describe a partially completed decoupled light delivery/collection experimental system shown schematically in Figure 7.20.

In order to measure localised reflections arising from within a turbid media we constructed the low-coherence interferometer shown below in Figure 7.1 as a precursor to building the proposed system shown in Figure 7.20. The system of Figure 7.20 was to have been constructed to test experimentally the hypothesis discussed in section 1.4.

As indicated above, the description of this system is broken down into various sections below. The first discusses the Michelson interferometer, the second the modulation and detection scheme, and the third the data acquisition and reference arm scanning: in sections 7.1 to 7.3, respectively. This breakdown is for convenience only as there is necessarily some synergetic overlap between the contents of the categories. The optical system (section 7.1) provided the means by which a heterodyne signal, created by a moving fringe pattern, could be generated at the detector system. The modulation scheme provided a means of which the relatively small heterodyne signal produced at the detector could be detected in spite of a large non-heterodyne signal background. The data acquisition and scanning system provided a way of producing automated pathlength resolved heterodyne signal vs. optical depth scans and a means for performing data acquisition under the control of a personal computer.

Figure 7.1: Experimental low-coherence fibre-optic Michelson · interferometer system
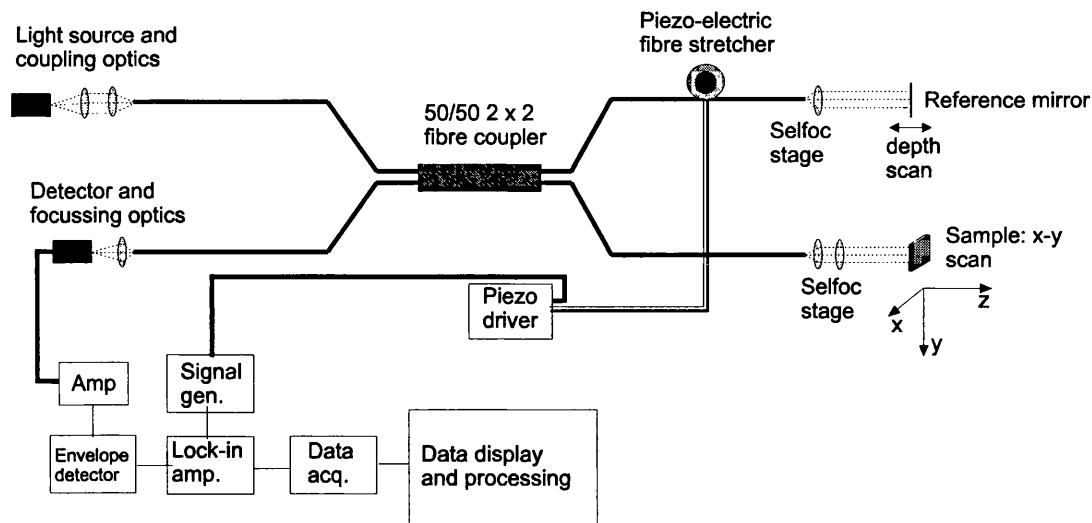
7.1 Optical system

All of the optical components used in the experiment were placed on an air-cushioned optical table. The selfoc stages, the reference mirror and the sample were all rail-mounted on Melles-Griot optical rails using custom-made mounts and 12 mm mounting posts. In addition the reference mirror and the sample selfoc stage were mounted using tilt-adjustable retainers.

7.1.1 Interferometer set-up

One original aim of the project was to develop a system that was, preferably, portable so that it could be used at the bedside. For this reason a fibre-optic based system was employed, since once deployed it would be compact and rugged.

Once we had decided to use a fibre-optic based device, the choice to use the Michelson configuration was made: a fibre-based Michelson interferometer being relatively simple to build and requiring few optical components.

At our disposal was a 50/50 coupler consisting of a 2x2 fused fibre coupler, with 5 m of fibre in each of the four fibre arms, set to split 50% of light incident at a wavelength of 820 nm in one fibre arm into each of the two opposite arms. This arrangement produced an immediate 3 dB loss from any signal beam propagating

128

towards the detector (this is also the case for an equivalent free-space component version). Our coupler was a PS788 device supplied by Point Source Ltd. made using Corning Flexcor 780 fibre. The fibre had a core diameter of 5 μm and an outside cladding diameter of 125 μm surrounded by a jacket that gave an overall outer diameter for the fibre of approximately 500 μm. Polarisation effects were not taken into account in this interferometer[*].

Two of the fibre ends were terminated into FC connectors and the other two into selfoc lenses as illustrated in Figure 7.1. The power emitted from each of the selfoc collimator terminated fibre arms was 2.0 mW, and the beams were collimated to 0.6 mm in diameter (1/e width). Use of selfoc collimators gave a certain degree of flexibility which would have been lost had we used a fixed focused end termination because as the beam was collimated it was thought that it would be relatively easy to add different optical stages to the fibre end at a later date. However, this also contributed to the problems discussed below.

The coupler arrangement was not ideal as both FC connectors and selfoc lenses gave rise to unwanted reflections at their various interfaces and they reduced the signal passing though them by a nominal 3 dB on each pass. This situation could have been improved by angle polishing the fibre ends and using external anti-reflection coated high quality optical components.

Furthermore, a 50/50 split ratio is not ideal when the sample in one arm of the interferometer does not produce a reflected coherent signal (heterodyne signal) that is of an intensity substantially equal to that reflected coherent signal in the other arm. As the relative coherent intensities in each of the arms becomes more disparate, the fringe visibility at the detector reduces. Compensation for this effect can be made if the reflectance of the sample is known and remains constant, by increasing the power incident upon the sample to a level which matches the signal of the light that travels in the reference arm. In tissue the range of reflectance may vary from 2.8% at the surface of the tissue to zero for coherent volumes deep inside the sample, so

---

[*] This was believed to be one of the biggest sources of problems encountered - see section 7.4

theoretically the relative power in one arm can be increased *ad infinitum*, however practical limits for *in-vitro* samples, and additionally health and safety regulated limits for *in-vivo* samples, also apply to the maximum useable power of the incident beam as defined by laser safety standard IEC 825[1]. That said, in the case of a tissue sample it is favourable, where possible, to have at least an 80/20 split in favour of the sample arm, and as high an optical power as practical incident upon the sample.

7.1.2 The light source

The low-coherence interferometer needed to contain a light source that possessed a short coherence length as this is one parameter that defines the maximum resolution of the overall system. In order to see interference fringes and produce a heterodyne signal, light returning to the detector via the sample and reference arms had to be matched to within an optical pathlength difference of $\pm l_c/2$, where l_c was the source's equivalent optical coherence length[*]. If this condition was not met, then the light returning along the sample and reference arms gave rise to an incoherent summation upon recombination at the detector that produced no interference fringes and thereby contributed to the non-heterodyne signal. A super-luminescent diode (SLD) was chosen as these are high power broadband sources that can be efficiently coupled to fibre-optic waveguides.

The SLD, essentially an anti-reflection coated semiconductor laser diode chip, was an SLD361 device supplied by Superlum of Moscow. It was a high powered device providing peak emission at 817.6 nm when drawing an operating current of 140 mA. The source coherence length in air was estimated at 32.4 ± 0.2 μm from a spectral measurement of the source's characteristics provided by the manufacturer.

The source assembly, built by the author, consisted of an SLD emitter thermally coupled to a thermoelectric cooling device that operated on the Peltier principal, typically drawing 100 mA DC at 3.5 volts. This device was further mounted upon a

---

[*] This general statement assumes that light arriving at the detector is either fully coherent or fully incoherent with the light in the reference beam. In practice, some light incident at the detector will be partially coherent - see section 5.3.4.1 for details of how this condition may be simulated.

large heatsink along with a Hytek Microsystems HY5600 thermoelectric cooling driver, and the whole system was supported by a screened dicast metal box that housed the drive electronics for the SLD itself. Current was fed into the box by a 15 way D-type connector from a laser diode power supply, an ILX Lightwave 3207B.

The use of a specially designed current controlled device to deliver the drive current was desirable as it provided a so-called soft start-up for the SLD, whereby the drive current ramped up slowly over approximately one second so as to prevent damage to the SLD. It also provided isolation for the SLD from mains spikes and other potentially damaging current and voltage surges as well as a controlled ramp down of the current when the SLD drive was switched off. A maximum current limit could also be set using the ILX 3207B, and it was set to 141 mA to prevent accidental oversetting of the current control setting or thermal runaway from damaging the device.

As a way of controlling the operation of the SLD during long overnight experiments, a computer controlled interlock system enabled and disabled the SLD by sending a TTL signal to a driver which shorted out the interlock on the ILX 3207B current source using a miniature non-latching relay.

The optical output of the SLD was coupled to one end of a single mode Corning Flexcor 780 fibre, with a core diameter of 5 μm and an outside cladding diameter of 125 μm. The other end of this fibre was terminated into an FC connector enabling it to be connected to one of the FC connectors of the 2x2 fused fibre coupler.

7.2 Modulation and detection

Where a turbid medium such as a tissue equivalent phantom material was used as the sample placed in the sample arm, the relative intensity of the reflected heterodyne producing signal (falling within the $\pm l_c/2$ optical path length matching range) compared to the non-heterodyne component due to the incoherent summation of all other light reaching the detector was generally very small. The precise value of this difference depended upon the optical properties of the sample and at what point the matching distance was set relative to any reflection producing components of the sample. By adjusting the optical path difference between the two arms we obtained a

131

fringe pattern at the detector, generally sitting upon a large DC signal, whose magnitude gave a measure of the reflectance of the sample at a depth corresponding to the optical path difference in the two arms $\pm l_c/2$.

In order to recover this small signal, which at the shot noise limit of detection could be as much as -140 dB lower than the background DC, coherent detection techniques using lock-in amplification were needed (see section 7.2.2 below). Due to the nature of coherent detection, the detection system was highly directionally sensitive. Although this allowed the detection system to further discriminate against multiply scattered light that was not incident upon the detector in precisely the direction of the reference beam, it did make stable repeatable alignment of the system extremely difficult.

7.2.1 Modulation scheme

To produce a time varying fringe pattern for the coherent detection to lock onto, modulation of the light signal in at least one of the arms of the interferometer was necessary. Several techniques are available, including Doppler, phase and pathlength modulation. We discounted Doppler modulation as we had encountered alignment problems in our system, and phase modulation due to the expense of electro-optic modulators and their inability to modulate over a range large enough to correspond to the number of fringes appearing in a typical coherence envelope (of the order of 30 fringes or so). Furthermore, we wished to avoid use of systems in which moving mirrors were employed to the greatest degree possible in order to facilitate the development of a bedside system. We therefore chose to use pathlength modulation within the fibre itself in an attempt to reduce alignment problems and further permit a relatively compact and rugged system to be built.

The modulator consisted of a piezo-electric cylinder (supplied by Roditi International Inc. and made from VP-A40 material) onto which a number of turns (10 in this case) were bonded with a strong, non-filled epoxy resin (FC/PC bonding epoxy supplied by Fibre Optics Centre Ltd.). Jacketed fibre was wound under tension by placing a small weight onto the fibre end and dangling it over a table edge, whilst clamping the cylinder to the table. Each turn was spot-fixed with superglue until set, and then

another turn added until all turns were done. Then the whole spiral of turns, held flush under tension against the cylinder, were permanently fixed using the non-filled epoxy resin. This ensured maximum transfer of radial cylinder stretch into fibre stretch. The cylinder was then driven with a Physik Instrumente PI263 high voltage amplifier which amplified a triangular drive waveform from a few volts up to around 40 V. The HT amplifier was driven with a signal derived from a Farnell SG3 signal generator.

The dimensions of the piezo-electric cylinder were selected to ensure that the radius of curvature of the fibre when bonded to the cylinder was greater than that which would induce substantial bending losses in the fibre. The piezo-electric cylinder chosen had dimensions of 50 mm outside diameter, 50 mm length with a wall thickness of 2.5 mm. The inner and outer walls were completely covered by thin metallic silver electrodes to which the connecting leads were soldered. The number of turns was calculated from the known properties of the piezo-electric cylinder to give a radial stretch of the order of 100 μm.

The optical pathlength modulation amount M, over which the piezo-electric cylinder stretched the fibre, was found by counting the number of fringes N_f that appeared during one period of a modulating signal provided by the signal generator using the formula $M = (N_f . \lambda)/2$, assuming a constant refractive index during stretching of the fibre. The value of optical pathlength modulation calculated according to this equation for our system was variable from $M = 22.0 \pm 1.0$ μm at a drive frequency of 8 Hz to $M = 12.0 \pm 2.0$ μm at a drive frequency of around 30 Hz, this latter frequency being that used during the performance of the majority of the experiments. The modulation fringe pattern was asymmetrical with the contraction of the piezo-electric cylinder being more rapid than its expansion. This hysteresis may have been due to pressure exerted by the jacket on the fibre, or was perhaps due to non-uniform attachment of the fibre cladding to the cylinder as a result of patchy application of epoxy resin.
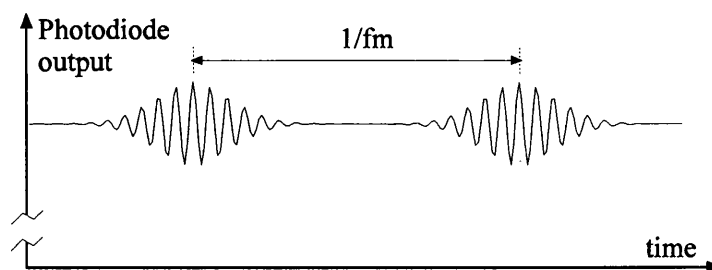
7.2.2 Detector system

The ability of the experiment to recover the small coherent fringe pattern from a large incoherent DC signal governed how small a reflectance could be measured by the system. The recovery of this AC signal is the subject of the following few paragraphs in which the operating principles of the experimental detection system are explained.

The fibre modulator (PZT cylinder) stretched the fibre over at least part of one complete coherence length at a frequency f_m. The coherent signal due to a reflection from within the sample was then seen as a set of fringes within an envelope defined by the coherence envelope of the source repeating periodically at the driving frequency f_m: Figure 7.2 illustrates this below.

To recover the envelope of the fringes, whose magnitude was proportional to the sample reflectivity, a system based on lock-in detection was used. First the envelope was recovered using an envelope detector (see section 7.2.3). This removed the DC signal component and helped to filter out any low frequency amplitude modulated light signals, such as those due to fluorescent lighting or, more problematically, those due to bending losses in the fibre caused by the PZT cylinder occurring at f_m. Once the envelope was recovered, lock-in detection was used to measure the RMS amplitude value at the reference frequency f_m, derived from the signal generator.

Figure 7.2: Schematic of photodiode output

One important consideration of the detector system was to ensure that the output of the photodiode was linear over the range of intensities applied to it. Thus it was important that the detector was not allowed to saturate, even with the relatively large input that came from the incoherent light falling onto the detector. This was because the small AC signal, which contained the information about the sample under test, sat

upon a large DC contribution due to the reference beam. This required a detector and amplifier with large dynamic range, good linearity and low noise.

The detector chosen was an FC coupled Honeywell HFD3002 silicon PIN photodiode whose output was fed into a transimpedance amplifier of variable gain and bandwidth.

A Theoptics TA20 transimpedance amplifier served as the transimpedance amplifier and was operated with a 5 kHz bandwidth low-pass filter with 12 dB/octave roll-off and a switchable gain (minimum sensitivity was ~1 V/nA). The minimum length of coax cable possible was used to feed the output signal from the transimpedance amplifier to the envelope detector: as a general matter of good practice, cable lengths were kept to a minimum in order to reduce noise pickup.

7.2.3 The envelope detector

Problems were encountered with a residual amplitude modulation of the light passing along the reference arm. It is believed that this was caused by birefringent coupling losses in the fibre induced as the piezo-electric cylinder stretched and contracted. These losses altered the coupling between core and cladding and lead to an AC signal at the photo-detector that was independent of the position of the reference mirror. This signal thus fed through the envelope detector into the lock-in amplifier where it gave rise to a DC at the output of the lock-in amplifier. Thus the following design was used to attenuate this signal whilst simultaneously allowing the fringes, at a higher frequency, to pass.

Figure 7.3 shows a schematic diagram of the envelope detector. Figures 7.4 and 7.5 show components of the envelope detector in more detail, and include component values or part numbers as appropriate.

Figure 7.3: Schematic of the envelope detector
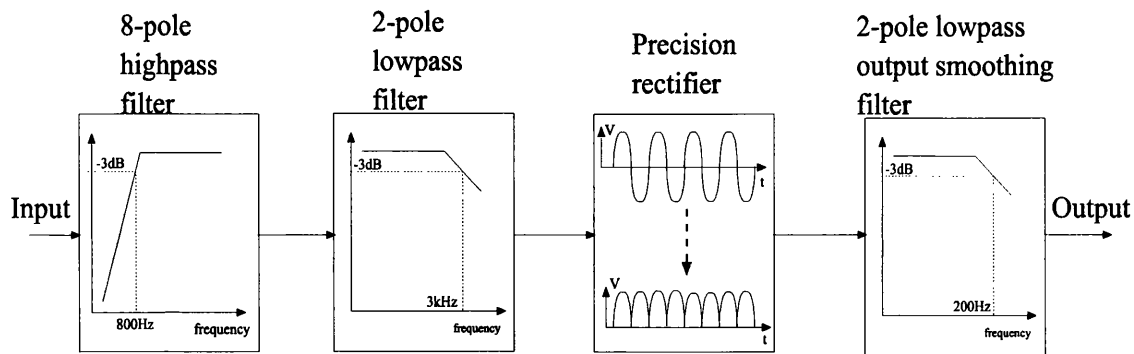
The envelope detector consisted of an 8-pole high pass filter input stage, constructed with precision OP27 instrumentation amplifiers cascaded in a Butterworth configuration.[2] This stage had a 3 dB point set at around 800 Hz so as to attenuate any stray residual 30 Hz modulation frequency (measured to be ~5 mV) at the input by ~70-80 dB down to the level of the intrinsic system noise (some 0.5 μV). The fringe frequency for our particular system was measured to be 1.1 kHz when the modulating cylinder was driven at 30 Hz, and so a low pass filter followed the first stage to roll off the frequency response above 5 kHz. Figure 7.4 below shows the circuit diagram for this part of the system.

The 8-pole filter circuit was followed by a 2-pole low-pass filter with a 3 dB cut-off point set at 5 kHz. This filter was chosen to bandwidth limit the envelope detector to approximately the same bandwidth as the transimpedance amplifier, thereby filtering out high frequency noise.

The rectifier part of the circuit, Figure 7.5, used small signal diodes in the feedback loop of a unity gain operational amplifier circuit. OP27s were chosen as the amplifiers for their low noise, low offset characteristics which gave superior performance when rectifying small signals close to zero volts. The rectified amplified fringes were smoothed, by a final stage, to recover the original envelope by use of a 2-pole 200 Hz low-pass filter circuit.

Figure 7.4: 8-pole Butterworth filter circuit
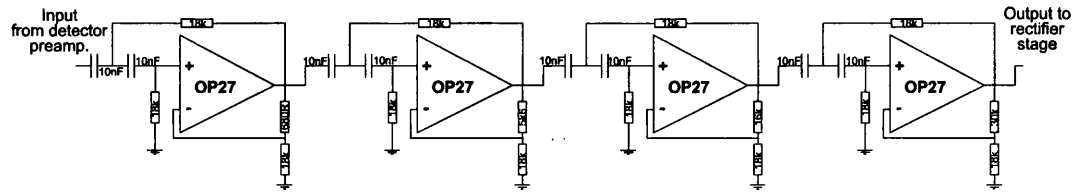
Figure 7.5: Rectifying and smoothing circuit
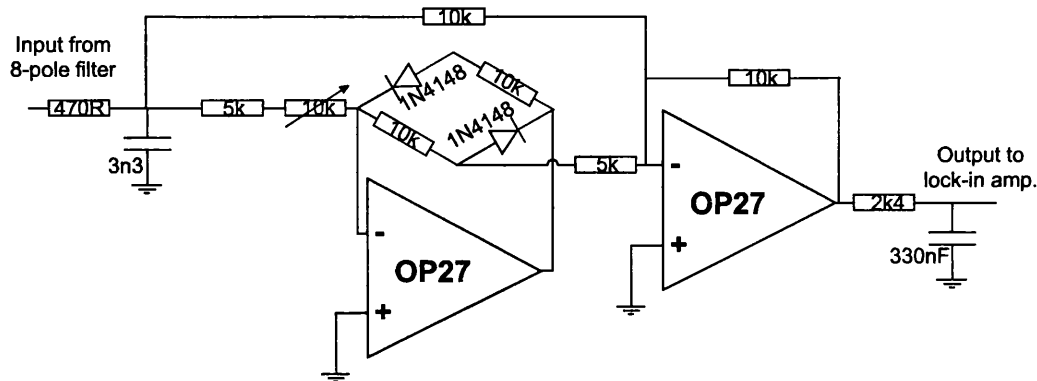
7.2.4 Lock-in amplifier

The lock-in amplifier used was a Stanford Research Systems SR830 DSP model with a maximum dynamic reserve of 100 dB and a minimum sensitivity of 2 nV. The lock-in amplifier was programmed remotely from a 486-PC computer via a GPIB interface, and it sent acquired data back across the same interface to the PC for storage.

7.3 Data acquisition and reference arm scanning

By scanning the reference arm mirror and measuring the magnitude of the fringe pattern produced, we were able to derive a signal that gave us a value of sample reflectance as a function of optical pathlength. The optical pathlength was easily converted to an equivalent depth in the sample as we knew, or could measure, the refractive index of the sample. This, therefore, allowed us to form a reflectivity profile of the sample as a function of depth in that sample.

137

7.3.1 Depth and lateral scanning

The depth scan, the z-direction illustrated in Figure 7.1, was achieved by moving a tilt-adjustable surface aluminiumised mirror mounted upon an Ealing DPS (digital positioning system) controlled translation stage. The mirror had a surface reflectance of approximately 80% for light at a wavelength of 820 nm. The stage was controlled from a PC via a GPIB interface and could be stepped over a distance of 50 mm with a resolution down to 1 μm (manufacturer's data).

Transverse scanning, in the x-y plane, was achieved by mounting the sample in a cylindrical holder upon two further DPS stages and using the PC to control the motion. Thus the computer was able to control the so called "voxel" position in three dimensions from which the coherent signal was sampled, and by stepping the stages in turn an image could be built up from these pixelated samples.

The stages had to be able to track accurately as they moved in a direction perpendicular to their direction of motion. The reference arm had to scan over distances of approximately 6 mm to achieve a tissue equivalent depth of 2 mm when the sample was held beneath a 2 mm thick glass flat. An order of magnitude calculation for the tilt tolerance for the reference mirror gave a value of approximately a tenth of a degree for a 3 dB coupling loss in the reference signal arm. This condition could be satisfied by the Ealing DPS controlled stages which tracked with a transverse accuracy of ±1 μm (manufacturer's data).

The lateral (depth or z-direction) resolution of the system was equal to l_c (~32.4 μm in air), whereas the transverse resolution (x or y-directions) could, theoretically, be narrowed using a lens focusing system to a diffraction limited spot (of the order of 5 μm in diameter).

7.3.2 Acquisition of data

Automated data acquisition and the scanning of the reference arm were achieved using an IBM compatible 486-based PC via a GPIB interface. The control software was written in the C programming language by the author so as to run under National

Instruments LabWindows version 2.2.1. The listing for this control software is given in Appendix A.

The data acquisition software averaged 10 data points, acquired by the PC from the lock-in amplifier, per stepped position of the reference mirror and stored this average value in tabular form along with a value indicating the relative position of the mirror with respect to the point at which the scan was begun.

7.4 General comments on the experimental design

Leads connecting the photodiode to the envelope detector and the envelope detector to the lock-in needed to be screened as well as possible. The output from the envelope detector was a screened coaxial cable whose connections provided an input to the single channel input of the lock-in amplifier. These were the noise critical points in the system. Careful arrangement of the equipment was needed to position sensitive instruments as far away as possible from the noisier items. The stepper motor stages and their controller were particularly noisy.

Problems encountered included loss of heterodyne signal due to alignment and tracking of the stepper stages, and temporal drift due to temperature and vibration: in fact, the output of the lock-in amplifier was observed to drift over time even when the optical pathlength in the reference arm of the interferometer was set to produce a heterodyne signal peak corresponding to a glass/air interface in the sample arm and the stepper stage left in a fixed position. This was believed to be predominantly due to atmospheric (temperature variations and air currents) and general environmental vibration due the siting of the equipment in a laboratory on the first floor of the building.

These problems did not prevent certain measurements across reflectance peaks obtaining a dynamic range of up to around 112 dB, see section 7.6 below for examples, but they did make it difficult to consistently perform high dynamic range contrast scans.

7.5 Tissue equivalent phantoms

This section discusses the need for and the design of the phantom materials used in various combinations as samples in the experimental system.

7.5.1 The need for phantoms

There were several reasons why it was advantageous to use tissue equivalent phantoms rather than either *in vivo* or *in vitro* tissue as samples in the low-coherence interferometer system. Two such reasons related to the issues of the repeatability and the stability of the measurements made. Since samples made from phantom materials were not subject to biological variations, such as cell wall degradation and physical decay, they were physically robust and remained optically stable over long time periods. Phantom materials could also made with known homogeneous optical properties.

Another reason for using phantoms was the ease with which they could be manipulated. Using phantom materials to provide test samples allowed us to progressively build up the complexity of the phantom to approach that of the real sample of interest, such as by adding successive layers and simulated blood vessels to approximate a skin sample. The physical properties of phantom materials also permitted machining or casting of individual components of samples into practically any shape that was desired. Different phantoms could then be mixed and matched to give embedded structure and a reconfigurable sample geometry. This "mixing and matching" also allowed us to choose the refractive indices and chose to match or mismatch boundaries.

The availability of biological samples was another reason for preferring phantom materials over excised biological samples, as not all laboratories would have had access to or storage facilities for the latter.

7.5.2 Materials available

Many different approaches and materials have been tried in the quest to find materials that closely simulate the optical properties of tissue. Broadly speaking, until

the development of solid phantoms in the early 1990's the range of materials available to simulate the optical properties of tissue fell into three basic categories.

The first approach simply replaced one type of biological tissue with another, more readily available type. This overcame the problem of dealing with availability of phantom material but did not deal with the problems of biological variation and repeatability. One such example that has been commonly used was chicken breast meat[3].

Other materials that have been used as phantom materials include liquid phantoms, especially emulsions containing naturally occurring lipids[4]. These lipids give rise to the scattering properties of radiation passing through them. These materials suffer from problems of longer term stability and also contain non-uniform distributions of scattering particle sizes. It is also impossible to guarantee that a different batch of the same material used one day will have exactly the same properties as another batch on another day. The most popular of these materials is Intralipid where the batch to batch variation in μ_s' is of the order of 5-10%[4].

A further liquid phantom has been used in an attempt to overcome problem of non-uniform particle size by introducing uniform sized particles into a liquid form. In this case the effect of the particles on the propagation of light could be calculated using Mie theory to produce known effects on the optical beam. This works well if the particles are held in a well mixed solution and are not allowed to settle from that solution, but liquid phantoms are not easy to handle or reconfigure into different arrangements. A classic example of this type of phantom material is a suspension of polystyrene spheres in water[5].

It is clear that none of the preceding three categories of phantom are ideal for making repeatable measurements, and it was with these thoughts in mind that the solid phantom material described in the next paragraph was developed by Mike Firbank[6] at UCL.

## 7.5.3 Design and construction of a solid phantom

Our solid phantoms were made from a base of epoxy resin (Ciba-Geigy MY750 araldite mixed with HY905 hardener and DY073 accelerator), and consequently were easy to process into thin layers, as they could be easily machined or cast. We added scattering centres (1.0 µm diameter silica spheres supplied by Duke Scientific) and near infra-red absorbing dyes into the resin matrix in proportions calculated to give values for μ_a, μ_s and g that were matched to the equivalents for the tissue the phantom was designed to simulate. The particles added to give rise to scattering were chosen according to their refractive index and size based on calculations made using Mie theory.

The Mie data was calculated using the computer program taken from Bohren and Huffman[5], and converted to the C language by Dr. Jeremy Hebden at UCL. It assumed that the scattering particles embedded in the matrix were illuminated by a plane wavefront and were sufficiently separated so that interference effects between them were negligible compared to self-interference effects due to interaction of the plane wavefront with the individual particles.

Unfortunately, using this method, it was not always possible to exactly match an arbitrary set of desired optical parameters to the materials available to build the phantoms. In particular we were limited by the suitable range of available epoxy resins and the consequent range of refractive indices this constrained us to. We were also limited by the type of scattering particle available and the restraints that also placed on particle size and refractive index. In particular, this often meant that materials had to be used where the refractive index difference was of the opposite sign to that generally occurring in tissue: i.e. the resin refractive index was greater than that of the scattering particles' refractive index. This does not effect the values of g, μ_a, and μ_s, but does have an affect on the backscattering cross-section (see Figure 7.6 below). Although this did not matter much for experiments done in transmission, or those concerned chiefly with diffuse light, it was of relevance to our experiments in which we were concerned with measuring the backscattered coherent reflectance. Interestingly, this is an effect that, as far as I am aware, has not been addressed in the literature regarding tissue phantoms.

142

Certain components of skin were difficult to simulate using our phantom material, in particular stratum corneum. Simulating tissue of very high μ_s values was known to be difficult, if one wished to retain a high value for the g-factor. This is because the particles used to produce the scattering in the phantoms for high g-factor were silica microspheres. At the high concentrations needed to produce large scattering coefficients, the spheres tended to clump together. This had the aggregate effect of changing the many small scatterers into a lesser number of larger ones, and thereby reducing the scattering coefficient (as well as altering g). In essence the relationship between the concentration of particles and the scattering coefficient became non-linear and the scattering coefficient effectively saturated. It was found experimentally that the linear relationship held up to concentrations of somewhere between 6-10% depending on the size and chemical properties of the scattering centres involved.[6]

Figure 7.6: The effect of inverting the refractive indices upon the backscattered intensity for 0.5 μm diameter spheres at 850 nm
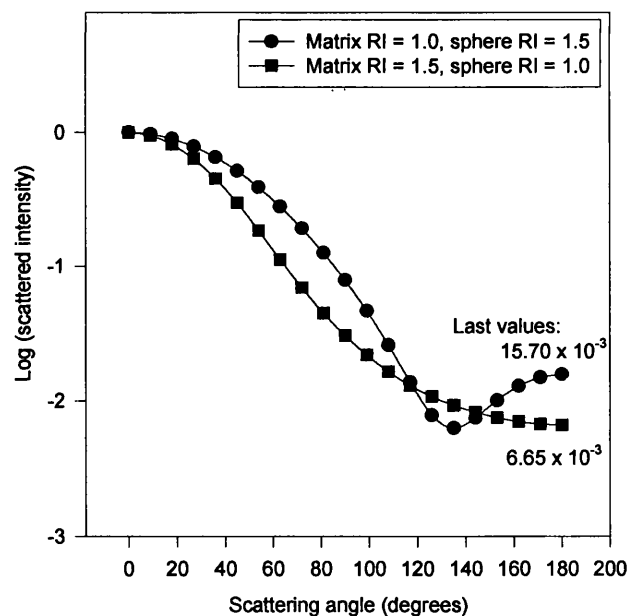
After considerable experimentation, the tissue equivalent phantoms used in these studies were made from epoxy resin of refractive index 1.56 (Ciba-Geigy MY750 araldite mixed with HY905 hardener and DY073 accelerator), into which were

embedded 1.0 μm diameter silica spheres (supplied by Duke Scientific), of refractive index 1.51 at 820 nm, in varying concentrations depending on the scattering coefficient required. Several different materials were made, all with an absorption coefficient of 0.04 mm^{-1}, but with values of reduced scattering coefficient, μ_s', varying from 0.5-2.0 mm^{-1}. The dye added to the mixture was Project 900NP dye whose absorption spectrum is shown below in Figure 7.7.

These samples were processed into disks of 2 cm diameter and a graded range of thicknesses. Thicknesses were 0.1, 0.2, 0.5, 1.0 mm, and the disks were used in a screw threaded retaining device to produce an easy to reconfigure phantom with variable numbers of layers, thickness and optical properties, clamped rigidly between two 2.56 cm diameter optical glass windows. The windows gave physical support to the plastic phantoms and also protected the plastic surface from environmental damage. Index matching between the resin layers was possible using the chemical Ethyl Cinnamate, which has a refractive index of 1.56 at 820 nm, and so closely matched that of the epoxy resin; the concentration of spheres was low enough that the perturbation in average refractive index due to the spheres was negligible. The rigidly clamped samples were placed in the sample beam of the interferometer shown in Figure 7.1.

7.5.3.1 Addition of blood vessels to the phantom

In order to incorporate a model blood vessel into the phantom, we added cylinders of various sizes filled with a blood phantom equivalent material (see section 7.5.4) into some disks of the phantom material made according to the process above. Two methods were adopted in order to add channels to the tissue phantom material. The first was to machine or engrave grooves into the surface of flat polished disks, and then to fill the grooves with the blood phantom before finally polishing the disks down again to remove any spillage lying on the surface. The second method involved embedding a wire that was held straight under tension into a setting sample of the tissue phantom. This block was then polished down and the wire pulled out, leaving a channel in the material. This channel was then filled with the blood equivalent phantom material and both ends were sealed with a quick setting epoxy resin. By

using the first and second methods, filled grooves varying in diameter from approximately 50 μm to 200 μm were readily producable.

Figure 7.7: Absorption spectrum of Project 900NP NIR dye
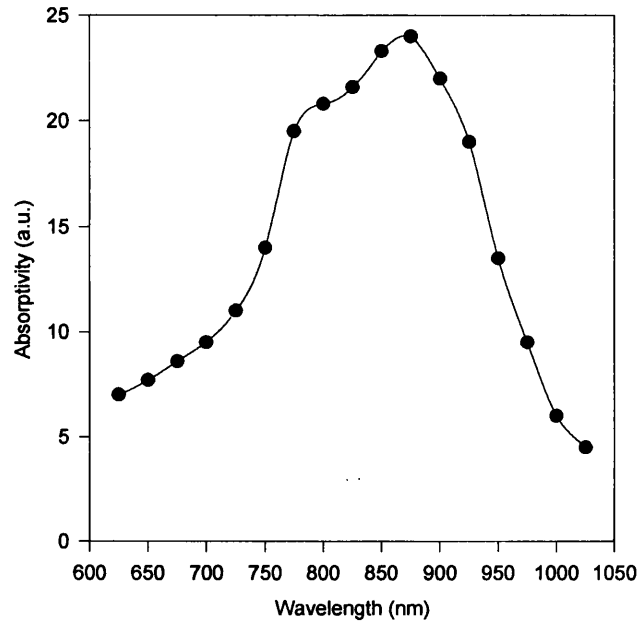
The layer containing the phantom blood vessel was then added into the stacked sampled. In this way a three layered model that included a blood vessel could be constructed. This was the model that our Monte Carlo technique simulated and would have allowed us to compare experimental and theoretical results. It was also a rudimentary approximation to the physical structure of skin.

7.5.4 Blood phantom material

Figure 7.8 below shows the physical dimensions of a red blood cell drawn using a side elevation with a plan view of the cell beneath it. The equatorial radius r = 4.25 μm, the greatest half thickness b = 1.2 μm and the least half thickness a = 0.5 μm.[7] The red cell thus has a volume of 4.3 x 10^{-17} m^3, and this is equivalent to a sphere of diameter 4.4 μm. The refractive index of the cell is 1.40 at 805 nm, and the plasma

145

has a refractive index close to that of water in the near infra-red, being 1.35 at 805 nm[8].

Figure 7.8: The red blood cell
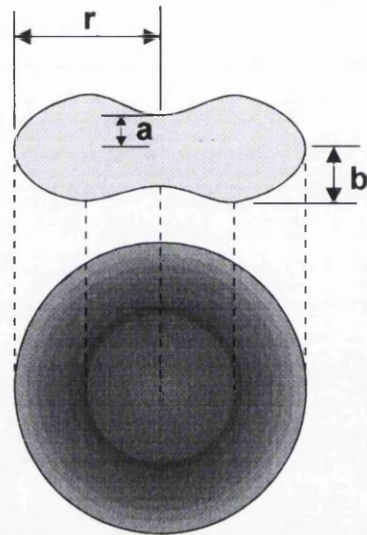
A Mie theory analysis of the above particles revealed that for a 3.5% concentration (by volume) of particles in an embedding plasma matrix, the g-factor was 0.991 and the scattering coefficient $\mu_s = 14.9$ mm^{-1}. This corresponded closely to measured data in the literature taken from whole blood samples[8]. If we used silica particles of diameter 5 μm, with refractive index 1.56, in a resin of refractive index 1.51 at 820 nm, we could recreate the values for the parameters calculated above to within 7% for backscattered light by taking a particle concentration of 3.3%. These values were chosen because of the availability of suitable commercially available particles and resin to make the phantom. The resin used was Ciba-Geigy MY750 araldite mixed with HY905 hardener, and the particles were 5.1 ± 0.5 μm calibrated borosilicate glass spheres supplied by Duke Scientific Corporation.

Figure 7.9: Graph showing a comparison of the angular intensity distributions between the Mie plot for a volume equivalent red blood cell and that for the phantom used to simulate it

Angle of deviation from incident beam direction (degrees)
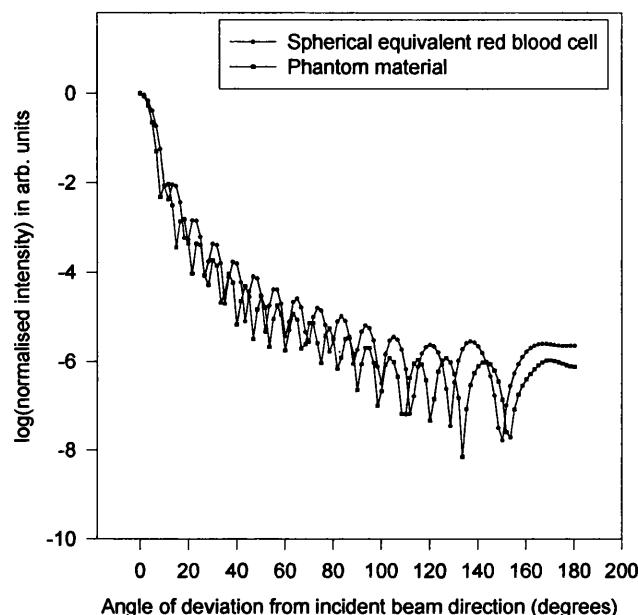
A comparison of the calculated angular intensity distribution for both a 4.4 μm sphere and the phantom scattering particles, using the 5 μm spheres, is shown above in Figure 7.9. The data was calculated using Mie theory. Whilst the angular oscillations do not match exactly the average does correspond closely between the two sets of data.

The work of Steinke[8] et al., compared measured light scattering data taken from blood samples of different animal species using a He-Ne laser. They suggested that equivalent volume Mie simulations give a good fit to the backscattering cross-section measured experimentally from human blood, but cautioned about the use of Mie theory to predict g-values as it tends to produce an overestimation of g. This is stated as being due to the deviation of the red blood cell from a spherical shape. The slight overestimation could be problematic in the case for high g-values where one is concerned with the value of μ_s' ($= \mu_s(1\text{-}g)$) as it can leads to an overestimation by up to a factor of 4-5 times; however where one is not concerned with μ_s', as was the case

for a coherent backscattering system, then the slight variation in g could be disregarded.

Figure 7.10: Effect of adding NIR 900NP dye to the blood phantom base epoxy resin
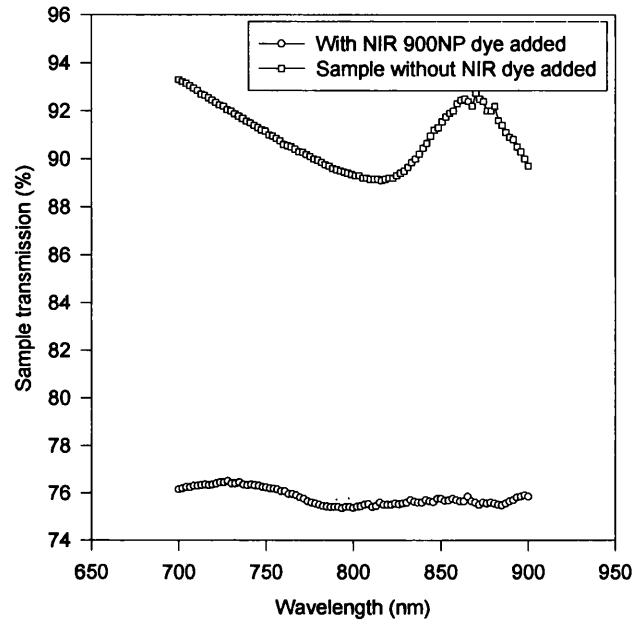
Blood was modelled as a scattering media with a relatively high absorption coefficient: that is a high absorption coefficient compared to that of the tissue that surrounded the blood vessel (μ_a = 0.6 mm^{-1} in blood as opposed to μ_a = 0.04 mm^{-1} in the surrounding tissue).

Figure 7.10 shows transmission spectra for the epoxy resin used to make the blood phantom before and after the addition of the near infra-red dye. A 3 mm thick disk of each of the two materials was manufactured and polished. The absorption spectra were then taken using a Varian 2300 spectrophotometer. The results showed that the dye was not chemically bleached by any of the components of the epoxy resin mixture and could thus be used in the production of the blood phantom. It had been found previously at UCL that certain dyes were susceptible to bleaching by chemical reaction with the epoxy resin hardener and so it was considered necessary to test any new mixtures for this possibility.

From the results of Figure 7.10 it was observed that 0.2 mg of dye, in a final quantity of 10 g of resin, changed the absorption coefficients for the two disks from 0.014 mm^{-1} to 0.031 mm^{-1}. Therefore in order to give an absorption coefficient similar to that of blood (0.6 mm^{-1}) we needed to add 6.9 mg of dye to a 10 g batch of the epoxy resin.

7.6 Experimental results

In this section we present some of the more interesting results generated by the scanning interferometer system shown in Figure 7.1, and described in detail in the preceding sections of this chapter. Selection of the data for this thesis is made in chronological order and therefore shows the effect of modifications made to the system between scans. What these modifications were and how they affected the measurements are described below in section 7.7.

The data plots show (in Figures 7.11 to 7.17 below) the heterodyne to non-heterodyne signal ratio HNHR (ordinate) as a function of optical pathlength set by the position of the depth-scan stage (abscissa). The data plots are normalised so that the value 0 dB represents the maximum measured HNHR for each figure. This maximum was usually created by the reflection from a glass/air interface of an optical glass flat which covered the samples and held them together in the retaining mount.

The data plots shown in Figures 7.11 to 7.17 below are discussed in more detail in section 7.7, whilst the rest of this section is devoted to describing the experimental conditions associated with each of the plots.

Figure 7.11 shows a scan performed using a collimated incident beam incident at normal angle and a degenerate delivery/collection geometry. The sample consisted of an optical glass flat, which was 2.0 mm thick, with a hand-polished thin flat layer of phantom material held beneath it. The phantom material layer had been designed with $\mu_s' = 1.0$ mm^{-1}, $\mu_a = 0.04$ mm^{-1} and $g = 0.9$.

Figure 7.12 shows another scan performed using a collimated incident beam incident at normal angle and the degenerate delivery/collection geometry. The sample in this

case was a non-index matched phantom sample held in position beneath a 2 mm thick optical flat. The phantom sample was the blood vessel sample having a 1 mm diameter cylinder of blood phantom material (μ_s = 14.9 mm^{-1}, μ_a = 0.6 mm^{-1} and g = 0.991) embedded close to the surface of a 5 mm thick disk of tissue phantom material (μ_s' = 1.0 mm^{-1}, μ_a = 0.04 mm^{-1} and g = 0.9). The surface of the phantom blood vessel was thus close to the glass/phantom boundary.

Figure 7.13 shows a scan using the same arrangement as for Figure 7.12 with the exception that the phantom sample was index matched to the glass disk above it by a thin layer of ethyl cinnamate.

Figure 7.14 depicts the results of a scan performed using a collimated incident beam incident at normal angle with a degenerate delivery/collection geometry. The sample was a disk of phantom material sandwiched between an upper optical glass flat retainer and a lower gold mirror. The sample was index matched on both sides using ethyl cinnamate. The disk had a mean thickness measured to be 0.12 mm and had the following optical properties: μ_s' = 1.5 mm^{-1}, μ_a = 0.04 mm^{-1} and g = 0.9. The data acquisition system performed averaging of 5 samples per one position of the stage.

Figure 7.15 shows the results of a scan performed using a focused sample beam, focal length f = 200 mm, incident at normal angle with a degenerate delivery/collection geometry. The sample was index matched to a 2 mm optical flat retainer using ethyl cinnamate. The phantom was formed using a thin top layer (d = 70 μm, μ_s' = 2.0 mm^{-1}, μ_a = 0.04 mm^{-1} and g = 0.9) above the blood vessel bearing phantom (described above).

Figure 7.16 illustrates data from a scan performed using the same light delivery/collection system as for the scan of Figure 7.15. The sample in this case was a 0.22 mm thickness tissue phantom disk (μ_s' = 2.0 mm^{-1}, μ_a = 0.04 mm^{-1} and g = 0.9) sandwiched between a 2 mm optical glass flat and a gold mirror, and index matched to each using ethyl cinnamate.

Figure 7.17 shows a scan using the same optical arrangement as the scans of Figures 7.15 and 7.16. The sample in this case was a stack of glass cover slips of measured

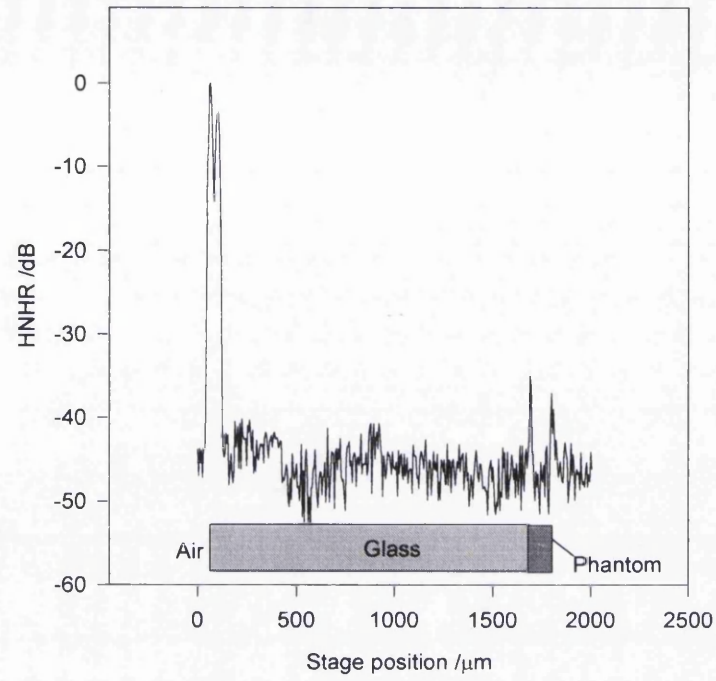mean thickness 0.165 mm. An average of 10 samples per stage position was used to derive the data for this scan.
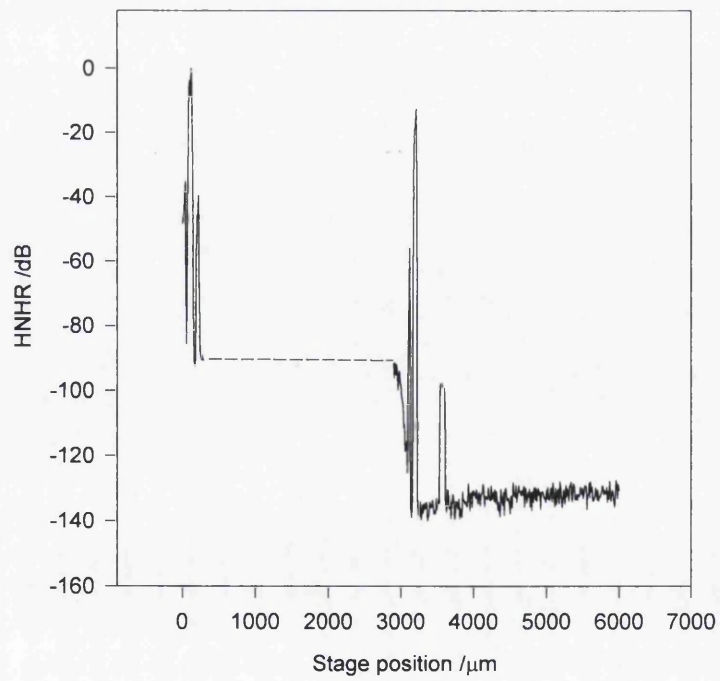
Figure 7.11

Figure 7.12
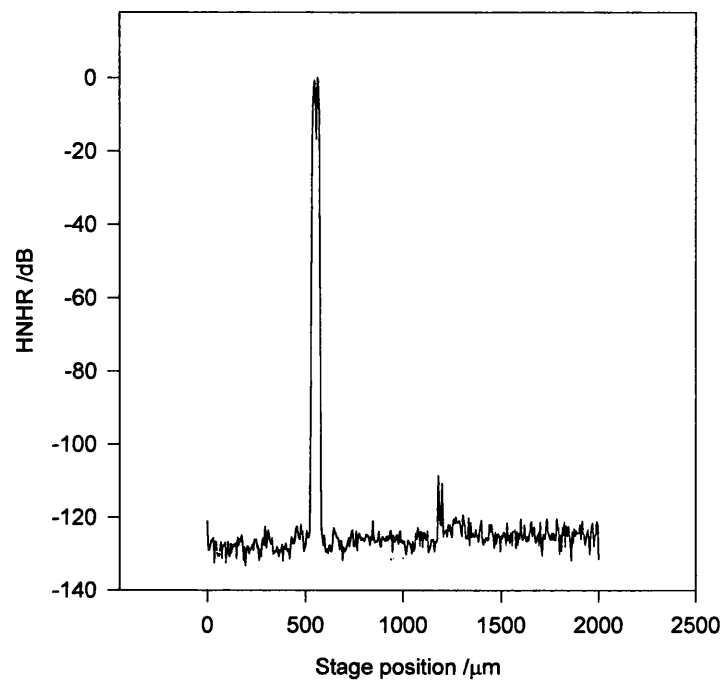
Figure 7.13
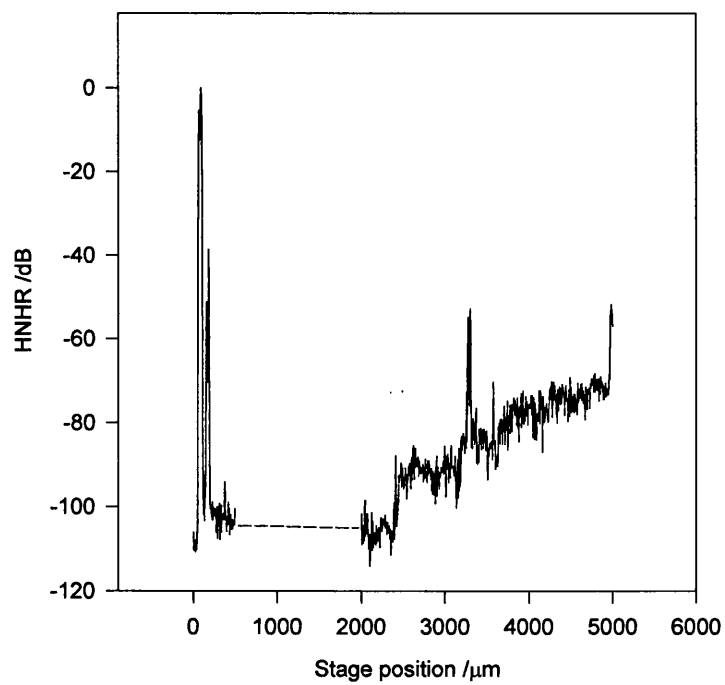
Figure 7.14
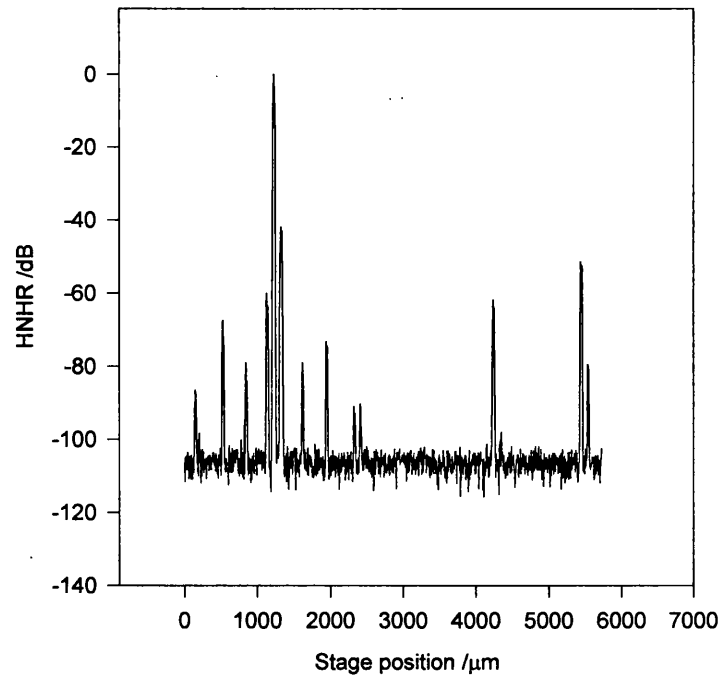
Figure 7.15
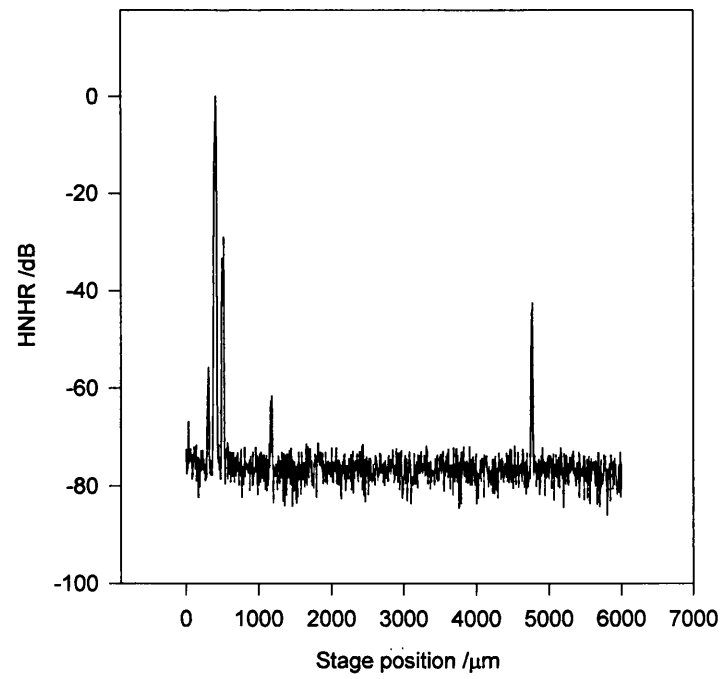
Figure 7.16
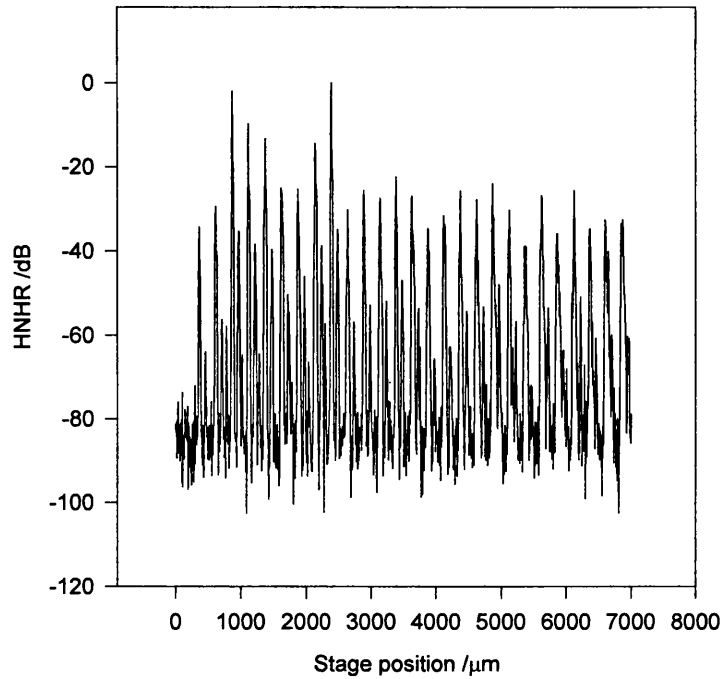
Figure 7.17

7.7 Discussion of experimental results

In this section we discuss the results produced by the low-coherence interferometer. Section 7.7.1 describes how the system was used to characterise some of the optical properties of the phantom materials we constructed. Section 7.7.2 discusses the dynamic range of the system, and section 7.7.3 relates to the triple peak observed in many of the results when the interferometer system performed a scan across a refractive index boundary. Section 7.7.4 illustrates results from a Monte Carlo simulation of the sample whose scan is shown in Figure 7.11.

7.7.1 Use of a low-coherence interferometric system to characterise phantom materials

As part of an experimental study performed using the fibre-optic low-coherence interferometer, some measurements were made to characterise the tissue equivalent phantom material. For these experiments, a degenerate 0.6 mm diameter collimated light delivery and collection system were used at normal incidence to the sample, and

depth (i.e. parallel to the z-axis) scans were performed to obtain the data sets by stepping at 5 µm intervals.

7.7.1.1 Measuring refractive index

The thin phantom material layer used as the sample of the scan of Figure 7.11 was measured at various points on its surface using callipers, and the results of this measurement averaged to give a value for the physical thickness of 70 ± 3 µm. The sample was then clamped between glass plates and placed into the scanning low-coherence interferometer where a z-depth scan was performed. Figure 7.11 above shows the result of this scan.

From the measured data, the optical path length for light at ~820 nm travelling in the phantom sample was determined to be 110 ± 5 µm. This gave a calculated value for the refractive index of the phantom of 1.57 ± 0.14. This technique was fairly crude, but gave a result comparable to the value range of refractive indices measured by Firbank et al[4] for similar phantom materials.

7.7.1.2 Measuring μ_t

In order to measure μ_t, varying thicknesses of phantom material (designed to have $\mu_s' = 2.0$ mm^{-1}, $\mu_a = 0.04$ mm^{-1} and $g = 0.9$) were held under an optical glass flat backed by a gold mirror. They were index matched on both faces using ethyl cinnamate, and then placed into the sample arm holder of the low-coherence interferometer. The peak heterodyne signal strength measured at an optical pathlength corresponding to the position of the mirror surface, found by performing a z-direction depth scan for each different thickness of phantom material, were then plotted as a function of phantom thickness. In this way, the attenuation plot of Figure 7.18 below was obtained (shown with a linear fit to the data plus 95% confidence limits).

Figure 7.18: Measuring phantom attenuation as a function of sample thickness
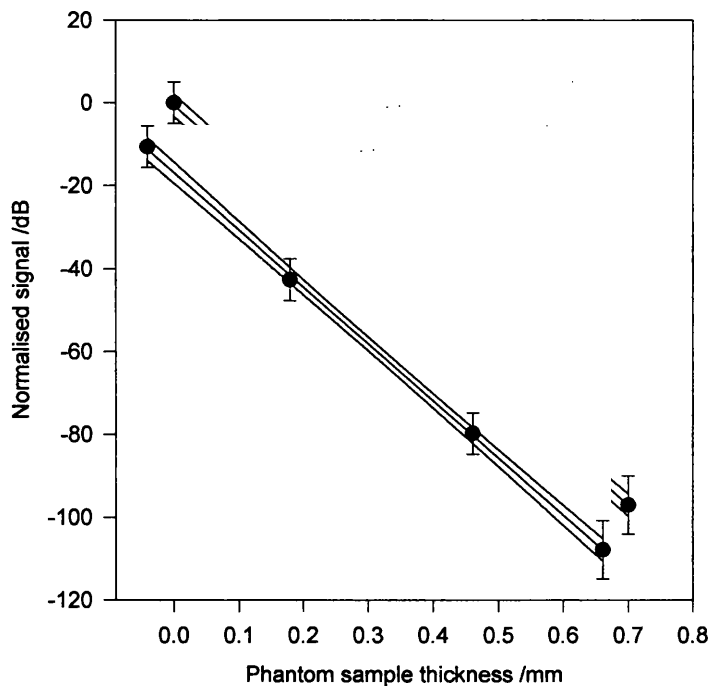
From the above plot we calculated a value for μ_t of 17.6 ± 0.3 mm^{-1} for our phantom material using the 95% confidence limits to calculate the error estimation. This value was some 12-13% below the design value for the phantom (μ_t was designed to be 20.04 mm^{-1}), a factor thought to be due at least in part to the clumping effect of the scattering particles. This phenomenon is known and has been described by Firbank *et al*[4]. It was also the case that the presence of any non-heterodyne signal would lead to a reduced value for μ_t, and this could be another factor that contributed to the lower than expected measured value.

7.7.2 General discussion of experimental results

Figure 7.11 clearly shows a surface reflectance peak from a glass/air interface at about 50 μm and two reflectance peaks at ~1650 μm and 1800 μm respectively. These latter two peaks were believed to be due to the refractive index mismatch between the glass and the phantom and the phantom and air, neither of which was index matched. The glass/phantom interface has a peak of -35 dB and the

phantom/air reflection a peak of -38 dB. This difference is believed to be due to scattering in the phantom which attenuates the phantom/air reflection.

For Figure 7.11 it should be noted that the system was sub-optimal as the modulation scheme and envelope detector previously described in this chapter had not been built at the time the results were taken. This lead to the poor dynamic range seen: i.e. some 50 dB between the reflection peak from a glass/air interface and the noise floor.

Figure 7.19: Monte Carlo simulated results of the sample used in Figure 7.11
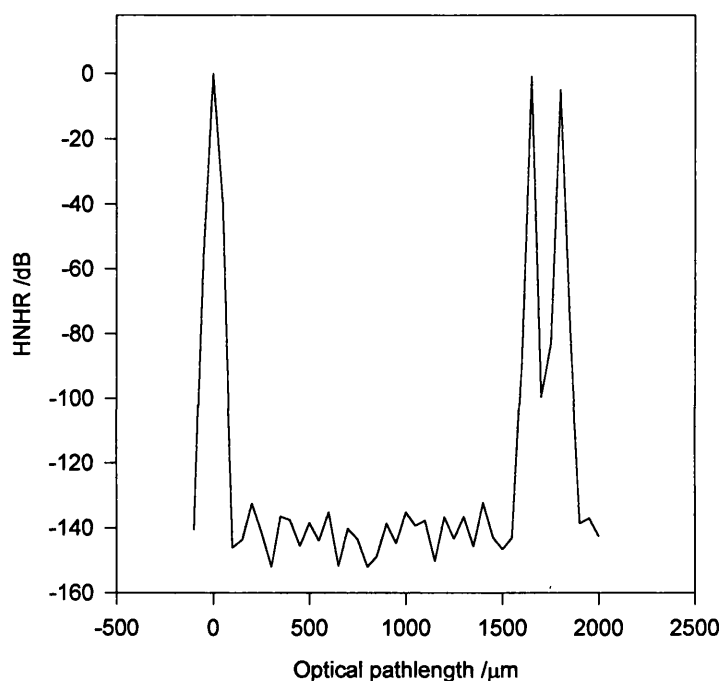
In order to validate the results from the experimental system, the Monte Carlo simulation described in Chapter 4 was set-up to perform a numerical simulation of the sample and experimental set-up used to generate the data of Figure 7.11. The results of this numerical simulation are shown above in Figure 7.19.

Figure 7.19 shows peaks at positions corresponding to the peaks found in Figure 7.11. However, the peaks at 1650 and 1800 μm in the Monte Carlo derived data are some 34 dB greater in intensity than those actually measured at corresponding positions in Figure 7.11. This disparity is believed to be due to misalignment of the

experimental system, which although optimised manually to give a maximum peak for the initial glass/air interface at 0 μm, is thought to have drifted from optimal alignment as the reference arm was scanned across the two rightmost peaks. This further confirmed our belief that alignment was a major problem in our experimental system.

Finally in regard to Figure 7.19, it is noted that the difference in intensity between the peaks at 1650 and 1800 μm was the same for both the measured and simulated results. In both cases, the peak at 1800 μm is some 4 dB below that at 1650 μm.

Figure 7.12 shows a scan for a glass flat covered blood vessel bearing phantom. The exact sample is described in section 7.6 above. It is notable that the dynamic range seen for this scan approached the theoretical shot noise limit. This scan was produced following introduction of the modulation scheme and envelope detector as described in section 7.2. In this scan three peaks are seen. The two strong leftmost peaks correspond to reflections from the surface of the 2 mm thick optical flat. They are separated by ~3000 μm, which corresponds to the optical thickness of the glass flat.

The two peaks are separated by a broken line, and in all the figures any broken line represents a stage step. In this case the stage step was 2500 μm. The size of the stage step could be programmed into the data acquisition code (see Appendix A), and caused the stage mounted mirror in the reference arm to be moved by a fixed amount during a stepped scan in order to speed up the data acquisition. This avoided the need to sample every 5 or 10 μm for regions of no interest to us, such as from within the optical glass flat.

For Figure 7.12 the HNHR measured in the glass flat was some -90 dB. It therefore appeared that a fortunate realignment of the reference arm had occurred following the stage step, which resulted in a ~135 dB dynamic range. This scan had the highest dynamic range of any scan we ever performed, and although a dynamic range of 80 to 110 dB was fairly easy to obtain, system performance in the 110 to 140 dB range appeared to happen by chance and only rarely. We believe that the reasons for this were due to the problems of aligning the reference beam mirror and keeping it

aligned during z-direction scanning: the effects of any misalignment being compounded by use of coherent detection techniques.

The third peak seen in Figure 7.12 arises from the interface between the phantom blood vessel and the surrounding phantom material. The peak is some 40 dB above the noise floor and some 100 dB lower than that produced at the glass/air interface. The peak corresponds to a reflectance of around 0.012% at a depth some 300 μm below the phantom surface.

Figure 7.13 shows a repeat of part of the scan performed in Figure 7.12, except that the phantom sample was index matched to the optical glass flat using ethyl cinnamate. The second peak at about 1150 μm apparently corresponds to the third peak in Figure 7.12, however, the index matching has reduced the magnitude of this peak by some 20 dB.

Figure 7.14 shows a scan performed for a phantom disk sandwiched between an optical glass flat and a gold mirror. The first peak corresponds to the glass/air interface at the surface. The peak at around 3200 μm corresponds to the gold mirror beneath the phantom. The noise floor is seen to rise in an approximately linear fashion from ~2300 μm to the end of the scan, where we see what is believed to be a stray peak caused by an internal reflection, possibly from one of the FC connectors. The noise floor rises at ~10 dB/mm. The reason for the rise from 2300 μm is not fully understood. It could be a noise artefact due to misalignment, but is not thought to be due to the phantom sample as the slope is not sufficiently steep: for the phantom $\mu_s = 15$ mm^{-1}.

The introduction of a $f = 200$ mm microscope objective lens and a multiple layer skin approximating sample into the interferometer is shown in Figure 7.15. Multiple peaks can be seen, and the results of this scan were inconclusive. The largest peak certainly corresponded to the glass/air interface at the upper face of the optical flat, and the peak seen at 4200 μm corresponded to the other face of the optical flat, but all other peaks were of indeterminate origin.

In order to take a step back from the confusing data of Figure 7.15, the skin approximating sample was replaced with a simple phantom slab having

$\mu_s' = 2.0$ mm^{-1} with a measured thickness of 0.22 mm. The upper surface of this slab was index matched to the glass flat, in contrast to the sample of Figure 7.15.

We observed that the three peaks in this scan appeared to correspond to those seen in the previous scan at 1100, 1950 and 5500 μm respectively, although the dynamic range had dropped to 80 dB and so the peaks corresponding to those in the previous scan at 1600 and 2300 μm could have been present but not measurable. Our conclusions were that the peaks at least 1100 and 4900 μm in Figure 7.16 were not due to the sample, but were probably introduced by the lens system itself.

Figure 7.17 shows a scan through a stack of glass cover slips. Regular peaks are observed every 250 μm. This spacing corresponds to a thickness of 0.167 mm, if the refractive index is taken as 1.5, and this is in close agreement with the measured thickness for the cover slips of 0.165 mm.

7.8 Conclusions

We have already mentioned above that the dynamic range seen in the experiments was variable and that the system was very sensitive to alignment. This was not helped by the relatively low-frequency modulation scheme employed, which allowed 1/f noise to add to variations caused by misalignment. The piezo-electric cylinder had to stretch over a relatively long optical path to give a good modulation depth in the fringe envelope, and its physical characteristics meant that this could only be achieved at a low modulation frequency of typically around 30 Hz. Ideally, an alternative modulation scheme should have been used having a high frequency (~kHz or above) modulation with an optical path length modulation of the order of, or greater than, the coherence length of the optical source. One such contender is Doppler modulation, which we crudely tried without success during several attempts to ramp the reference arm depth scanning stage at constant linear velocity.

Piezo-electric cylinder modulation was unsatisfactory for another reason. Driving the cylinder caused stress-induced birefringence in the wound and bonded fibre which could cause light travelling in the fibre to couple from one polarisation state to another. Since we took no account of polarisation state this effect produced an amplitude modulated signal at the detector which, although filtered by the envelope

detector to a large degree, still contributed a small amount to the noise measured at the detector. Furthermore, it resulted in an unpredictable variation in measured heterodyne signal at the detector, dependant upon the amplitude and frequency of the driving signal applied to the piezo-electric cylinder.

Another phenomenon sometimes seen when measuring the HNHR across a glass/air interface was a triple peak. This triple peak appeared where we would have expected only to observe a single peak. The triple peak comprised a maximum central peak occurring where the expected single peak should have been, with two lower valued peaks occurring at approximately 100 μm either side of the central peak. Such a peak may clearly be seen in Figure 7.16. Here a first peak of some -56 dB at ~250 μm is followed by a main peak of 0 dB at ~350 μm, and by a third peak of -30 dB at ~450 μm.

Several possible reasons for the peaks can be identified. Firstly that the triple peak was due to birefringence caused by the stretching of the fibre creating differing multiple optical pathlength paths for light of different polarisations. In this hypothesis the interferometer essentially becomes two interferometers having two different optical pathlengths according to the polarisation of the light. Changes in the modulation used and/or alignment variations could also cause the amplitude of the peaks to vary and in certain cases the "two interferometers" to be pathlength matched and the triple peaks to merge into a single peak. A single peak was sometimes observed, although this was the exception rather than the rule.

Another theory for the origin of the two peaks was that they were caused by internal reflections close to the optical source. A reflection may have occurred at one facet of the SLD cavity or at the fibre end abutting the SLD cavity, and there may possibly have been additional cavity modes or side lobes generated in the output of the SLD as a result. Such side lobes could also have been merged into one peak or even suppressed entirely by alignment of the reference arm or by fortuitous cylinder stretch induced polarisation effects. This effect could have been significantly reduced by using angle polished fibre ends and optical coupling fluids.

The aforementioned problems were further compounded by stray reflections that made location of reflectance peaks and their interpretation difficult. In this respect use of a glass cover for the samples, not only to hold them flat but also to provide a strong reflectance peak at a glass/air interface for surface location, was advantageous. However, even this provision did not guarantee that peaks that were observed at positions corresponding to points within the sample were not due to reflectance peaks or Fabry-Perot peaks caused by the interferometer itself.

7.9 A partially developed experimental system

In order to be able to do the experiments to analyse the effect of delineating the illuminating and collecting optics in the sample arm, and thereby allow comparison of the Monte Carlo data (in section 6.2) to experimental data, the system shown below in Figure 7.20 was proposed. Unfortunately, there was insufficient time available to complete its assembly before the end of the studentship funding period.

The operating principle of the alternative system was basically the same as that of the interferometer shown in Figure 7.1 but with a few changes to the layout. Firstly, the addition of a 2x1 coupling block was necessary to allow for separate illuminating and detection channels at the sample surface. A 2x1 coupler made from Corning Flexcor 780 with a split ratio of 50/50 was available. The two fibres emerging from the same side of the coupler were terminated into similar selfoc lenses to those used in the 2x2 coupler, and the single channel was terminated with an FC connection.

A retro-reflector was available to replace the reference mirror so that the reference beam could be split into the input channel of one of the selfoc terminated fibres of the 2x1 coupler. The retro-reflector, a borosilicate glass prism supplied by Melles-Griot, could then have been scanned to give rise to the path difference necessary to acquire fringes from different volumes within the sample.

The detector system would have remained exactly the same as before except that the photodiode would have been placed so as to measure the output of the 2x1 coupler and the now redundant arm of the 2x2 coupler was to have been coupled to a beam dump. However, it was also envisaged that the 2x1 and 2x2 couplers could be

swapped so as to remove the need for a beam dump and also allow for dual balanced detection to be used.

Figure 7.20: Low-coherence interferometer system incorporating angular decoupling of the sample delivery and collection paths
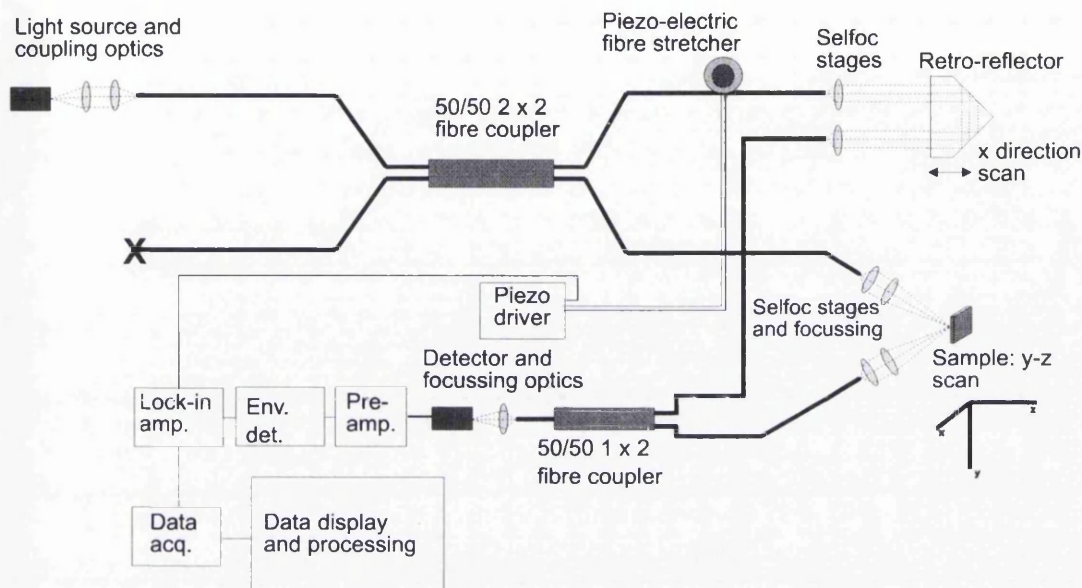
In the case of the tilt experiment, a confocal system was to have been used. The sample delivery arm was designed to focus the incident light to a small spot. This was to have the effect of both reducing the volume into which the light was delivered about the focus and increase the irradiance falling into the volume of interest. This would enhance the signal intensity coming back from the region of interest. The collecting objective lens was to have had the effect of reducing the region from which emerging light fell on the detector. The collecting objective lens was also to have another important function: specular reflection from the surface entering the collecting optics was to be rejected thereby reducing the background intensity falling on the detector and so improving the measured HNHR. It was our belief that this experimental arrangement would lead to an enhanced HNHR at the detector, and that this would be corroborated by the results of our Monte Carlo simulations which were designed to simulate such an experimental system.

Chapter References

[1] British standards BS EN 60825

[2] P. Horowitz and W. Hill, *The art of electronics*, Cambridge University Press, 1980

[3] B. B. Das, K. M. Yoo and R. R. Alfano, "Ultrafast time-gated imaging in thick tissues: a step toward optical mammography," *Opt. Lett.,* Vol. 18, No. 13, pp. 1092-1094, 1993

[4] S. T. Flock, S. L. Jacques, B. C. Wilson, W. M. Star and M. J. C. van Gemert, "Optical properties of intralipid: a phantom medium for light propagation studies," *Lasers. Surg. Med.,* Vol. 12, pp. 510-519, 1992

[5] C. F. Bohren and D. R. Huffman, *Absorption and scattering of light by small particles,* (Wiley-Interscience, New York, 1983)

[6] M. Firbank et al., "Development of a stable and reproducible tissue equivalent phantom for use in infrared spectroscopy and imaging," *SPIE proceedings,* Vol. 1888, pp. 264-270, 1991

[7] R. S. Chadwick and I.-D. Chang, "A laser study of the motion of particles suspended in a slow viscous shear flow," *J. Colloid and Interface Science,* Vol. 42, No. 3, pp. 516-534, 1973

[8] J. M. Steinke and A. P. Shepherd, "Comparison of Mie theory and the light scattering of red blood cells," *Appl. Opt.,* Vol. 27, No. 19, pp. 4027-4033, 1988

Thesis summary

We began in Chapter 1 with a summary of the techniques used for optical imaging and modelling in tissue. In Chapter 2 we then outlined the basic terminology and concepts used in the field of tissue optics so as to provide a basis for understanding the chapters that follow on. We then discussed, in Chapter 3, the physical and optical properties of skin, and included a table incorporating published optical parameters for components of human skin.

In Chapter 4 we discussed the coding and design details of the Monte Carlo simulation used to simulate photons transported through a skin-approximating model incorporating an embedded blood vessel. Then in Chapter 5 we described the design of a further computer program that was developed to analyse the data generated by the Monte Carlo simulation of Chapter 4. The analysis program was flexible enough to be able account for any partially coherent signal emerging from the model used in the simulation of Chapter 4, although we never operated it in this mode.

The results of the Monte Carlo analysis were presented in Chapter 6. The conclusions of our Monte Carlo analysis, based upon these results, highlighted the benefits of using index-matched samples and confocal detection. They also showed that although decoupling the light delivery and collection systems in an imaging low-coherence interferometer does not improve HNHR (heterodyne to non-heterodyne signal ratio) *per se*, it could improve the contrast seen in a scanned image of a relatively large simulated blood vessel embedded in a layered skin-approximating phantom by up to some 30 dB.

In Chapter 7, we presented details of an experimental low-coherence interferometer built by the author and some experimental results produced by this interferometer, including several having a dynamic range (~130 dB) approaching the shot noise limit for detection (~140 dB). We outlined problems of stability and reproducibility of the experimental results, and suggested possible improvements to the interferometer system with a further view to eliminating the triple peak that was often observed in the data scans. Some of the improvements recommended included angle polishing of

166

fibre ends, index matching of components and samples, and use of a higher frequency modulation scheme.

The production of layered skin tissue approximating phantoms incorporating a stable blood simulating material was also discussed in Chapter 7, and the results of using the interferometer to characterise some of the phantom materials were presented. These results gave a value for μ_t that was some 12-13% below the design value, and possible reasons why, such as clumping of scattering centres and the presence of measured non-heterodyne signal, were mentioned.

The closing part of Chapter 7 presented and discussed a partially-completed experimental interferometer having decoupled light delivery/collection optics. Construction of this system had been commenced with a view to producing further experimental work to verify directly the results produced by the Monte Carlo simulations whose results were presented in Chapter 6. The final part of Chapter 7 provides suggestions and tips, based on the author's experience, for how the partially-completed interferometer could be put into effect in order to perform any future experiments designed to verify the results of the Monte Carlo simulations.

APPENDIX A: AUTOMATED DATA ACQUISITION PROGRAM CODE

FOR LabWindows™ (Version 2.2.1)

```
/* Data acquisition program for the Ealing DPS and SR830 system
   Copyright (c) Grant Bedford May 1996 */

/* Function prototypes */
int initialise_dps( void );
void initialise_lia( void );
int initialise_trans_amp( void );
int user_info( void );
void zero_stage( void );
void move_transverse_stage( void );
void wait_for_stop( double );
/* set_transimp_amp( ); */
double set_lockin( void );
long read_data( void );
void validate_and_save( long );
void printOutBinaryResults( void );
void printOutIEEEResults( void );
void printOutLIAResults( void );
void initGpib( char *devName );
void txLia( char *str );
void txDps( char *str );
void setupLia( void );
double get_time_const( void );
void move_stage( void );
void set_rate( void );
void write_header( int );
double get_gain( void );
void set_time_const( void );
void jumpStage( void );

/* Globals */
long max_pos, step, samples_per_point, pos, count;
long transverse_pos, transverse_step, max_transverse;
long jumpPosition, sizeOfJump;
int dps_string_size, lia_string_size, trans_amp_string_size;
int dps_string_zero_size, dps_string_transverse_size;
char dps_string[51], lia_string[51], trans_amp_string[51];
char dps_string_zero[51], dps_string_transverse[51];
char dps_string_transverse_zero[51];
char jumpString[51];
int dps_string_transverse_zero_size;
int jumpStringSize, errorFound;
int lia, dps, trans_amp; /* SR830 handle */
```

```
int rxBuf[660*2]; /* FAST mode data buffer */
double rBuf[660]; /* half buffer for R data only */
float rfBuf[1000]; /* Floating point data buffer */
double frequency, sampling_frequency;
int filehandle;
int firstPass;

void main( void )
{
int direction;
double lia_time_const;
long bytes_read;
count = 1;
firstPass = 0;
errorFound = 1;

AO_VWrite (1, 0, 4.95);
AO_Update (1);

/* Initialise GPIB instruments */
dps = initialise_dps();
initialise_lia();
trans_amp = initialise_trans_amp();

/* Get user defined info. and initialise DPS */
direction = user_info();
write_header( direction );

/* Now set the lock-in parameters, gain etc. */
lia_time_const = 0.1; /*hands value of lock-in TC to wait function*/

/* Start the nested loop controlling the 2 stages */
for( transverse_pos = 0; transverse_pos <= max_transverse; transverse_pos +=
transverse_step )
  {
  FmtOut("\nTransverse position = %d[b4]\n",transverse_pos);
  if( transverse_pos != 0 ){
    /* Move transverse stage to its next (if any) position */
    move_transverse_stage();
    }

  for( pos = 0; pos <= max_pos; pos += step )
    {
    /* For future expansion: insert setting up of GPIB
     controlled transimpedence amplifier */
    /* set_transimp_amp( ); */

    /* Read a set of data and tranfer data to the PC */
    bytes_read = read_data();
```

```c
/* trap errors from lock-in and reset if error occurs */
if( iberr != 1 ){
/* FmtOut("\nReset due to iberr:%d\n",iberr); */
  iberr = 1;
  setupLia();
  txLia("REST"); /* reset data buffer */
  errorFound = 0; /* error has been found */
  }

/* Check the data and if its good enough save it to disk */
validate_and_save( bytes_read );

/* Print position of stage so we know where it has got to */
FmtOut( "%d[b4]", pos );
if( ( count % 8 ) == 0 )
  FmtOut( "\n" );
else FmtOut( "\t" );
++count;

/* if a jump is required in the motion do it here */
if( pos == jumpPosition ){
  pos += ( sizeOfJump );/* one step less as it steps next */
  jumpStage(); /* steps one less acc. for in dps string */
  }

/* move stage to the next position */
if( pos == max_pos )
  zero_stage();
else move_stage();

/*wait_for_stop( lia_time_const );*/
txLia("AGAN");/* ... remove wait_for_stop and use autogain to do
more accurate scans/otherwise used fixed gain for max speed and look
for saturations at the reflection mismatches */

/* test for key press/abort program */
if ( keyhit() )
  {
  FmtOut("\n\nProgram aborted");
  getkey();
  exit(0);
  }

  } /* End of pos loop */

} /* END of transverse stepping loop */

/*
```

```c
AO_VWrite (1, 0, 0.0);
AO_Update (1);*/

/* return stage 2 (transverse) to starting position */
ibpct( dps );
ibwrt( dps, dps_string_transverse_zero, dps_string_transverse_zero_size );

} /* END of MAIN() */


int initialise_dps( void )
{
int dps;

dps = ibfind("DPS");
if( dps < 0 )
  {
  FmtOut("\nDPS stage driver not found");
  exit( -1 );
  }
else
  {
  /* DPS found so initialise it */
  ibpct( dps );
  }
return dps;
}  /* END of initialise_dps() */


void initialise_lia( void ) /* Terminate ALL LIA commands with '\n' */
{
lia = ibfind("LIA");
if( lia < 0 )
  {
  FmtOut("\nLIA driver not found");
  exit( -1 );
  }
else
  {
  /* LIA found so initialise it */
  /* Set SR830 to output ALL data to the GPIB interface */
  txLia("OUTX1");
  setupLia();
  ibtmo(lia,13); /* Turn off timeout for lia, or set the timeout longer than
            scan (10s) The timeout measures the FULL number of bytes
            and not the time since the most recent byte is received */
  }

} /* END of initialise_lia() */
```

```
int initialise_trans_amp( void )
{
int trans_amp;
trans_amp = -1;
FmtOut("\nTransimpedence amplifier not yet installed\n");
return trans_amp;
} /* END of initialise_trans_amp() */


int user_info( void )
{
/* Get direction step size etc. of movement. Calculate
   the necessary DPS control strings from this info. */
int direction;
char choice[2],*dps1,dps2[16],*dps3;
long int_step_size, motor_units_per_step, transverseZero;

int_step_size = 1; /* Size of one FULL step in microns */
direction = 0; /* -1 = outwards, 1 = inwards */

FmtOut("\nMove z-stage inwards (i) or outwards towards stage motor end (o): ");
ScanIn("%s",&choice[0]);
if( choice[0]=='i' || choice[0]=='I' )
  direction = 1;
if( choice[0]=='o' || choice[0]=='O' )
  direction = -1;
if( direction == 0 )
  {
  FmtOut("\nYou must choose 'i' or 'o'");
  exit( -1 );
  }

FmtOut("How far to move (microns): ");
ScanIn("%d[b4]",&max_pos);

FmtOut("Step size (multiples of %d[b4] microns): ",int_step_size);
ScanIn("%d[b4]",&step);

FmtOut("Do you want to jump the stage in mid-travel (y/n): ");
ScanIn("%s",&choice[0]);
if( choice[0] == 'Y' || choice[0] == 'y' ){
  FmtOut("At what point should it jump: ");
  ScanIn("%d[b4]",&jumpPosition);
  FmtOut("How far should it jump: ");
  ScanIn("%d[b4]",&sizeOfJump);
  /* create format string for the jump itself */
  sizeOfJump -= step;
```

172

```
    sizeOfJump *= direction;
    dps1 = "*1SF,1MN,1MR";
    Fmt(dps2,"%s<%d[b4]",sizeOfJump);
    dps3 = "\r\n";
    Fmt( jumpString, "%s<%s%s%s",dps1,dps2,dps3 );
    jumpStringSize = NumFmtdBytes();
    if( sizeOfJump < 0 )
      sizeOfJump *= -1;
    }
else jumpPosition = -1;

FmtOut("Reference frequency: ");
ScanIn("%f",&frequency);

FmtOut("How many samples per point: ");
ScanIn("%d[b4]",&samples_per_point);

/* Calculate the necessary control string for the DPS */
if( step < int_step_size )
  step = int_step_size;

motor_units_per_step = step / int_step_size;
motor_units_per_step *= direction;

dps1 = "*1SF,1MN,1MR";

/* convert motor_units... to a string to add to dps1 */
Fmt(dps2,"%s<%d[b4]",motor_units_per_step);
dps3 = "\r\n";

/* concat. all three strings */
Fmt( dps_string, "%s<%s%s%s",dps1,dps2,dps3 );
dps_string_size = NumFmtdBytes();


/* Calculate the string necessary to zero the longitudinal stage */
/* Move it in opposite direction by the amount the stage travels */
motor_units_per_step = max_pos * -1 * direction;
dps1 = "*1SF,1MN,1MR";
/* convert motor_units... to a string to add to dps1 */
Fmt(dps2,"%s<%d[b4]",motor_units_per_step);
dps3 = "\r\n";
/* concat. all three strings */
Fmt( dps_string_zero, "%s<%s%s%s",dps1,dps2,dps3 );
dps_string_zero_size = NumFmtdBytes();
/* Finished string for zeroing stage */


/* Gather info for the transverse stage */
```

```
FmtOut("\nMove transverse inwards (i) or outwards towards stage motor end (o): ");
ScanIn("%s",&choice[0]);
if( choice[0]=='i' || choice[0]=='I' )
    direction = 1;
if( choice[0]=='o' || choice[0]=='O' )
    direction = -1;
FmtOut("How far to move (microns): ");
ScanIn("%d[b4]",&max_transverse);
FmtOut("Step size (multiples of %d[b4] microns): ",int_step_size);
ScanIn("%d[b4]",&transverse_step);
/* Calculate the necessary control string for the DPS */
if( transverse_step < int_step_size )
    transverse_step = int_step_size;
motor_units_per_step = transverse_step / int_step_size;
motor_units_per_step *= direction;
dps1 = "*2SF,2MN,2MR";
/* convert motor_units... to a string to add to dps1 */
Fmt(dps2,"%s<%d[b4]",motor_units_per_step);
dps3 = "\r\n";
/* concat. all three strings */
Fmt( dps_string_transverse, "%s<%s%s%s",dps1,dps2,dps3 );
dps_string_transverse_size = NumFmtdBytes();
/* End of info for transverse stage */


/* make zeroing string for transverse */
transverseZero = max_transverse * direction * -1;
dps1 = "*2SF,2MN,2MR";
/* convert motor_units... to a string to add to dps1 */
Fmt(dps2,"%s<%d[b4]",transverseZero);
dps3 = "\r\n";
/* concat. all three strings */
Fmt( dps_string_transverse_zero, "%s<%s%s%s",dps1,dps2,dps3 );
dps_string_transverse_zero_size = NumFmtdBytes();

return direction;
} /* END of user_info() */



void wait_for_stop( double lock_in_time_constant )
{
/* Need to wait for lock-in and stage to settle. Get the lock-in time
   constant via the GPIB to calculate the settle in real time */
double  time,
        stage_settling_time,
        wait_to_acquire;

stage_settling_time = 0.055; /* time in seconds to settle mechanics */

/* Wait until we start to acquire. 95% of final value in 3 TCs */
```

174

```c
wait_to_acquire = stage_settling_time;

time = Timer();
SyncWait( time, wait_to_acquire );

} /* END of wait_for_stop() */


double set_lockin( void )
{
/* The brains section. Set lock-in parameters and return the
   time constant as a double */
double time_constant;
int i, nPts;
char tstr[20];

time_constant = 0;

/* auto configure the lock-in */
txLia( "AGAN"); /* auto gain, auto reserve */
/*txLia( "ARSV" );*/ /* set auto reserve */

/* set gain to be 10mV */
/*txLia( "SENS20" );*/
/* SET lock-in to normal reserve */
/*txLia("RMOD1");*/
/* Set the lock-in time constant according to the reference frequency */
set_time_const();

/* set the sampling rate based on new frequency */
set_rate();

/* Query time constant */
time_constant = 0.1; /* set in setupLia() */

/*txLia("AOFF3");*/

return time_constant;
} /* END of set_lockin() */

double get_time_const( void )
{
/* Takes value of time constant from lock-in, converts it to a real
   value in seconds and returns the value in seconds as a double */
char get_string[20];
int return_value;
double value;

txLia( "OFLT?" ); /* query lock-in */
```

```
ibrd( lia, get_string, 20L ); /* read answer into string */
Fmt( &return_value, "%d<%s", get_string ); /* convert value to int */

/* look up the TC corresponding to the return value */
if( return_value > 19 || return_value < 0 ){
  FmtOut("\nTime constant not returned");
  exit( 1 );
  }
if( return_value == 0 )
  value = 0.00001;  /* 0 - 10 micro Seconds */
if( return_value == 1 )
  value = 0.00003;  /* 1 - 30 micro Seconds */
if( return_value == 2 )
  value = 0.0001;   /* 2 - 100 micro Seconds */
if( return_value == 3 )
  value = 0.0003;   /* 3 - 300 micro Seconds */
if( return_value == 4 )
  value = 0.001;    /* 4 - 1 mS */
if( return_value == 5 )
  value = 0.003;    /* 5 - 3 mS */
if( return_value == 6 )
  value = 0.010;    /* 6 - 10 mS */
if( return_value == 7 )
  value = 0.030;    /* 7 - 30 mS */
if( return_value == 8 )
  value = 0.100;    /* 8 - 100 mS */
if( return_value == 9 )
  value = 0.300;    /* 9 - 300 mS */
if( return_value == 10 )
  value = 1.0;      /* 10 - 1 Second */
if( return_value == 11 )
  value = 3.0;      /* 11 - 3 Seconds */
if( return_value == 12 )
  value = 10.0;     /* 12 - 10 Seconds */
if( return_value == 13 )
  value = 30.0;     /* 13 - 30 Seconds */
if( return_value == 14 )
  value = 100.0;    /* 14 - 100 Seconds */
if( return_value == 15 )
  value = 300.0;    /* 15 - 300 Seconds */
if( return_value == 16 )
  value = 1000.0;   /* 16 - 1000 Seconds */
if( return_value == 17 )
  value = 3000.0;   /* 17 - 3000 Seconds */
if( return_value == 18 )
  value = 10000.0;  /* 18 - 10,000 Seconds */
if( return_value == 19 )
  value = 30000.0;  /* 19 - 30,000 Seconds */
```

176

```
return value;
} /* END of get_time_const() */


long read_data( void )
{
/* Transfer a set of data from the lock-in to the PC */
long number_of_bytes, bytes_read;

number_of_bytes = 4 * samples_per_point;
txLia("FAST1;STRD"); /* fast data transfer */
ibrd( lia, rxBuf, number_of_bytes );
bytes_read = (int) ibcnt;
txLia("PAUS");

return number_of_bytes;
} /* END of read_data() */


void validate_and_save( long bytes_read )
{
/* Check the data falls within required std dev etc. It may be wise
   just to dump all to disk and do stats. post-mortem. Save the data
   to the HDD, checking the disk isn't full etc. */
/* data is stored in rxBuf in form (R, theta) both are 2 byte words*/
int no_of_R_vals, i;
double meanVal, stdDev, gain, mean;
double x, y, R;

no_of_R_vals = bytes_read / 4;
for( i = 0; i < no_of_R_vals; i++ )
  {
  /* calc. the R-values from the X-Y values */
  x = ( double ) rxBuf[2*i];
  y = ( double ) rxBuf[2*i+1];
  R = sqrt( x*x + y*y );
  rBuf[i] = R;
  }
StdDev( rBuf, no_of_R_vals, &meanVal, &stdDev );
gain = get_gain();
if( errorFound == 0 ){
  errorFound = 1; /* false no error condition */
  return;
  }
mean = meanVal * gain / 30000.0; /* 30000 is the FSD value */
filehandle = OpenFile( "fastdaq.dat",2,1,1 );
FmtFile( filehandle, "%s<%d[b4]\t", pos );
FmtFile( filehandle, "%s<%f\t", mean );
/*FmtFile( filehandle, "%s<%f\t", gain );*/
```

177

```
FmtFile( filehandle, "%s<%f\n", stdDev );

CloseFile( filehandle );
} /* END of validate_and_save() */


void printOutBinaryResults( void )
{
/* Calculates the first 10 values of R based upon the X and Y values
   taken in FAST mode by the SR830 */
int i;
double x,y,r;

FmtOut("\n\n");
for( i = 0; i < 10; i++ )
  {
  x = (double) (rxBuf[2*i]) / (double) 30000.0; /* 30000 is full scale */
  y = (double) (rxBuf[2*i+1]) / (double) 30000.0; /* multiply by the full scale voltage */
  r = (double) sqrt( x*x + y*y ); /* compute r from x and y */
  FmtOut("%d %f\n",i,r);
  }

} /* END of printOutBinaryResults() */


void printOutIEEEResults( void )
{
/* Prints the first 10 values of R transfered in IEEE floating point
   format by the SR830 */

int i;

FmtOut("\n\n");
for( i = 0; i < 10; i++ )
  FmtOut("%d %e\n",i,rfBuf[i]); /* easy as values are already IEEE floats */

} /* END of printOutIEEEResults() */


void printOutLIAResults( void )
{
/* Calcs. the first 10 values of R transfered in LIA format by SR830 */
int i,mant,exp;
float val;

FmtOut("\n\n");

for( i = 0; i < 10; i++ )
  {
```

```
mant = (int) rfBuf[2*i];          /* first comes mantissa (16 bit) */
exp = (int) ( rfBuf[2*i+1] ) - 124; /* then binary exponent (16 bit) offset by 124 */
val = ( float ) mant * ( float ) pow( 2.0, ( double ) exp );
FmtOut("%d %e\n",i,val);
 }

} /* END of printOutLIAResults() */


void initGpib( char *devName )
{
if(( lia == ibfind( devName )) < 0 )
  {
  FmtOut("\nCannot find SR830 \n\a");
  exit( 1 );
  }

} /* END of initGpib() */


void txLia( char *str )
{
/* append line feed and send */
int response, test, strlen;

test = 0;

strlen = StringLength( str );
ibwrt( lia, str, strlen );

while( test == 0 )
  {
  ibrsp ( lia, &response );  /* Test bit 6: if set device is */
  test = ( response && 16 ); /* requesting service */
  }

} /* END of txLia() */



void txDps( char *str )
{
/* append line feed and send */
int response, test, strlen;

test = 0;

strlen = StringLength( str );
ibwrt( dps, str, strlen );
```

179

```c
while( test == 0 )
  {
  ibrsp ( dps, &response ); /* Test bit 6: if set device is */
  test = ( response && 16 ); /* requesting service */
  }

} /* END of txDps() */




void setupLia( void )
{

txLia("*RST"); /* initialise lock-in */

txLia("SRAT10"); /* set 64 Hz sample rate */
txLia("DDEF1,1,0;DDEF2,1,0"); /* set CH1=R, CH2=theta.
                       Buffers store CH1 and CH2 */

/* Set 2x line notch filters */
txLia( "ILIN2" );
/* Set filter slope to 24dB/octave */
txLia( "OFSL3" );
/* Set synchronous filter */
txLia( "SYNC1" );
/* Set reference to be external source */
txLia("FMOD0");
/* Select falling edge TTL trigger */
txLia("RSLP2");
/* Select low noise reserve mode */
txLia("RMOD2");
/* Select a single ended input A */
txLia("ISRC0");
/* Set input shielding to GROUNDED */
txLia("IGND1");
/* drop to maximise sensitivity */
txLia( "SENS20" );/* fixed gain to avoid "autogaining" */

/* AUTOset the offset to remove residual modulation component */
/*txLia("AOFF3");*/
/* ch1 output to display */
txLia("FPOP1,0");

txLia("OFLT8"); /* set TC to be 0.1s */
/*txLia("HARM2");*/ /* use 2nd harmonic */
FmtOut("\n");
if( firstPass == 0 ){
  FmtOut("Scan is initialised; Press a key to begin scan ... ");
```

```c
  getkey();
  }
firstPass = 1;
} /* END of setupLia() */




void move_stage( void )
{
/* Steps the stage by one unit - step is a global as is dps_string and
   dps_string_size. Predefined in the initialisation function get_user() */
long  response, mask;
mask = 163840; /* Bits 15 and 17 indicate if stage has tripped right or left */

ibpct( dps );
ibwrt( dps, dps_string, dps_string_size );

/* Check to see if the DPS stage has hit the end stop
txDps( "*1TS" );
ibsrp( dps, &response );
respone &= test;
if( response != 0 )
  {
  FmtOut( "Stage has hit end of its travel range" );
  exit( 1 );
  }
*/

} /* END of move_stage() */




void set_rate( void )
{
/* sets the lock-in acquisition rate */
char data_sent[12], word1[8], word2[8];
int freq_number;
double sample_period; /* this is frequency NOT period */

sample_period = frequency / 5;
sampling_frequency = sample_period; /* NOT!!! */

if( sample_period < 0.0625 )
  freq_number = 0;
if( sample_period >= 0.0625 && sample_period < 0.125 )
  freq_number = 1;
if( sample_period >= 0.125 && sample_period < 0.250 )
  freq_number = 2;
if( sample_period >= 0.250 && sample_period < 0.500 )
```

```
      freq_number = 3;
if( sample_period >= 0.500 && sample_period < 1.00 )
      freq_number = 4;
if( sample_period >= 1.0 && sample_period < 2.0 )
      freq_number = 5;
if( sample_period >= 2.0 && sample_period < 4.0 )
      freq_number = 6;
if( sample_period >= 4.0 && sample_period < 8.0 )
      freq_number = 7;
if( sample_period >= 8.0 && sample_period < 16.0 )
      freq_number = 8;
if( sample_period >= 16.0 && sample_period < 32.0 )
      freq_number = 9;
if( sample_period >= 32.0 && sample_period < 64.0 )
      freq_number = 10;
if( sample_period >= 64.0 && sample_period < 128.0 )
      freq_number = 11;
if( sample_period >= 128.0 && sample_period < 256.0 )
      freq_number = 12;
if( sample_period >= 256.0 && sample_period < 512.0 )
      freq_number = 13;
if( sample_period >= 512.0 )
      freq_number = 14;

Fmt( word1, "%s<%s", "SRAT" ); /* make string to transmit */
Fmt( word1, "%s<%d", freq_number );
Fmt( word2, "%s<%s", ";SEND0" );
Fmt( data_sent, "%s<%s%s", word1, word2 );

/*txLia( data_sent );*/

} /* END of set_rate */


void write_header( int dir )
{

filehandle = OpenFile( "fastdaq.dat",2,1,1 );
FmtFile( filehandle, "Pos\tMean\tStd dev\t" );

if( dir == -1 )
  FmtFile( filehandle, "\tDIR = OUT\n" );
else FmtFile( filehandle, "\tDIR = IN\n" );

CloseFile( filehandle );

} /* END of write_header() */
```

```c
double get_gain( void )
{
/* returns sensitivity setting of lock-in as gain multiplier */
double gainVal;
char get_string[20];
int retVal;

txLia( "SENS?" );
ibrd( lia, get_string, 20L );
Fmt( &retVal, "%d<%s", get_string );

if( retVal == 0 )
  gainVal = 2.0;
if( retVal == 1 )
  gainVal = 5.0;
if( retVal == 2 )
  gainVal = 10.0;
if( retVal == 3 )
  gainVal = 20.0;
if( retVal == 4 )
  gainVal = 50.0;
if( retVal == 5 )
  gainVal = 100.0;
if( retVal == 6 )
  gainVal = 200.0;
if( retVal == 7 )
  gainVal = 500.0;
if( retVal == 8 )
  gainVal = 1000.0;
if( retVal == 9 )
  gainVal = 2000.0;
if( retVal == 10 )
  gainVal = 5000.0;
if( retVal == 11 )
  gainVal = 10000.0;
if( retVal == 12 )
  gainVal = 20000.0;
if( retVal == 13 )
  gainVal = 50000.0;
if( retVal == 14 )
  gainVal = 100000.0;
if( retVal == 15 )
  gainVal = 200000.0;
if( retVal == 16 )
  gainVal = 500000.0;
if( retVal == 17 )
  gainVal = 1000000.0;
if( retVal == 18 )
  gainVal = 2000000.0;
```

```c
if( retVal == 19 )
  gainVal = 5000000.0;
if( retVal == 20 )
  gainVal = 10000000.0;
if( retVal == 21 )
  gainVal = 20000000.0;
if( retVal == 22 )
  gainVal = 50000000.0;
if( retVal == 23 )
  gainVal = 100000000.0;
if( retVal == 24 )
  gainVal = 200000000.0;
if( retVal == 25 )
  gainVal = 500000000.0;
if( retVal == 26 )
  gainVal = 1000000000.0;

return gainVal;
} /* END of get_gain() */


void set_time_const( void )
{
/* sets the lock-in time constant */
char data_sent[12], word1[8], word2[8];
int tc_number;
double period;

period = 1 / frequency;

if( period < 0.00003 )
  tc_number = 0;
if( period >= 0.00003 && period < 0.0001 )
  tc_number = 1;
if( period >= 0.0001 && period < 0.0003 )
  tc_number = 2;
if( period >= 0.0003 && period < 0.001 )
  tc_number = 3;
if( period >= 0.001 && period < 0.003 )
  tc_number = 4;
if( period >= 0.003 && period < 0.01 )
  tc_number = 5;
if( period >= 0.01 && period < 0.03 )
  tc_number = 6;
if( period >= 0.03 && period < 0.1 )
  tc_number = 7;
if( period >= 0.1 && period < 0.3 )
  tc_number = 8;
if( period >= 0.3 && period < 1.0 )
```

```
  tc_number = 9;
if( period >= 1.0 && period < 3.0 )
  tc_number = 10;
if( period >= 3.0 && period < 10.0 )
  tc_number = 11;
if( period >= 10.0 && period < 30.0 )
  tc_number = 12;
if( period >= 30.0 && period < 100.0 )
  tc_number = 13;
if( period >= 100.0 && period < 300.0 )
  tc_number = 14;
if( period >= 300.0 && period < 1000.0 )
  tc_number = 15;
if( period >= 1000.0 && period < 3000.0 )
  tc_number = 16;
if( period >= 3000.0 && period < 10000.0 )
  tc_number = 17;
if( period >= 10000.0 && period < 30000.0 )
  tc_number = 18;
if( period >= 30000.0 )
  tc_number = 19;

Fmt( word1, "%s<%s", "OFLT" ); /* make string to transmit */
Fmt( word2, "%s<%d", tc_number );
Fmt( data_sent, "%s<%s%s", word1, word2 );

/*txLia( data_sent );*/
/*txLia("OFLT10"); 1s time constant */
} /* END of set_time_const() */


void zero_stage( void )
{
/* Function to move stage 1 (longitudinal Z scan) back to start position */
ibpct( dps );
ibwrt( dps, dps_string_zero, dps_string_zero_size );
}/* END of zero_stage() */


void move_transverse_stage( void )
{
/* Steps the transverse stage (2) one unit in selected direction */
/* and saves transverse position to disk */
char *send_str;

filehandle = OpenFile( "fastdaq.dat",2,1,1 );
FmtFile( filehandle, "\nTrans: " );
FmtFile( filehandle, "%s<%d[b4]\n", transverse_pos );
CloseFile( filehandle );
```

185

```
ibpct( dps );
ibwrt( dps, dps_string_transverse, dps_string_transverse_size );

}/* END of move_transverse_stage() */

void jumpStage( void )
{
/* jumps stage to new position */
/* max speed of stages = 100 mm/s */
double timeToJump, maxStageSpeed;

maxStageSpeed = 100 * 1000; /* speed in microns/sec */
timeToJump = (double) sizeOfJump / maxStageSpeed;
ibpct( dps );
ibwrt( dps, jumpString, jumpStringSize );
wait_for_stop( timeToJump );
}/* END of jumpStage () */
```